



**University of
Leicester**

**The progenitors of extended emission
gamma-ray bursts**

Benjamin Paul Gompertz

Supervisors:

Paul O'Brien

Graham Wynn

Thesis to be submitted for the degree of

Doctor of Philosophy

at the University of Leicester.

X-ray & Observational Astronomy Group

Department of Physics and Astronomy

University of Leicester

May 27, 2015

The progenitors of extended emission gamma-ray bursts

Benjamin Paul Gompertz

Abstract

Gamma-ray bursts (GRBs) are the most luminous transient events in the Universe, and as such are associated with some of the most extreme processes in nature. They come in two types: long and short, nominally separated either side of a two second divide in gamma-ray emission duration. The short class (those with durations of less than two seconds) are believed to be due to the merger of two compact objects, most likely neutron stars. Within this population, a small subsection exhibit an apparent extra high-energy emission feature, which rises to prominence several seconds after the initial emission event. These are the extended emission (EE) bursts.

This thesis investigates the progenitors of the EE sample, including what drives them, and where they fit in the broader context of short GRBs. The science chapters outline a rigorous test of the magnetar model, in which the compact object merger results in a massive, rapidly-rotating neutron star with an extremely strong magnetic field. The motivation for this central engine is the late-time plateaux seen in some short and EE GRBs, which can be interpreted as energy injection from a long-lived central engine, in this case from the magnetar as it loses angular momentum along open field lines.

Chapter 2 addresses the energy budget of such a system, including whether the EE component is consistent with the rotational energy reservoir of a millisecond neutron star, and the implications the model has for the physical properties of the underlying magnetar.

Chapter 3 proposes a potential mechanism by which EE may arise, and how both classes may be born within the framework of a single central engine.

Chapter 4 addresses the broadband signature of both short and EE GRBs, and provides some observational tests that can be used to either support or contradict the model.

Declaration

I hereby declare that no part of this thesis has been previously submitted to this or any other University as part of the requirement for a higher degree. The work herein was conducted by the undersigned except for contributions as acknowledged in the text.

Benjamin Paul Gompertz
May 27, 2015

Acknowledgments

Firstly, I would like to thank my supervisors, Paul and Graham. Despite being two of the busiest men I have ever met, they have always found time to offer help and advice whenever I needed it, and have provided invaluable guidance both for research projects and career choices throughout my PhD. I have been very lucky to benefit from their formidable combined skill set, which has provided a series of fascinating topics and opportunities that I have enjoyed immensely.

A massive thank you to all the various residents of the G17 office who have helped to make my time in Leicester so illuminating and enjoyable; it's been a pleasure to come to work in such a friendly and convivial environment. A special mention to Owen, who helped me more than I think he realises in overcoming the dreaded 'imposter syndrome' when I first arrived, and made settling in a new city all the more easy. Special thanks also to Klaas, whose apparently infinite wisdom is matched only by his infinite patience with inane and banal questions on a daily basis. My gratitude doesn't stop at my own office, and I'd like to say a big thank you to all the other PhD students, postdocs, and staff who have been so welcoming.

Thanks to Kim for teaching me to analyse *Swift* data, and for bailing me out when the GRBs wouldn't behave! Also to Phil for his input and insight, even though he was driven to jumping offices half way through my PhD to get away from the questions. I am extremely grateful to Antonia for taking the time to teach me when I first arrived, as well as for getting me started on the whole magnetar thing, and to Alexander for the valuable knowledge in my final year. I'd like to thank Rhaana for her advice and support too.

This thesis would not have been possible without the love and support of my wonderful family, and I'd like to thank my mum for providing a great source of motivation by undertaking her own PhD at the same time as me, engaging my competitive nature in a friendly contest. A contest that I lost by a matter of mere months. I'd also like to thank my dad for instilling in me a love of words, thereby saving this thesis from incomprehensible nonsense. Or mitigating against it at least. Thanks to them and the rest of my family for their constant support, belief, and encouragement.

Finally, special thanks and eternal gratitude to my beautiful wife Lianne, whose love has pulled me through the tough patches and made the triumphs all the sweeter. None of this would have been possible without her, partly because I would still have been sleeping in until the afternoon. I love you.

I would not like to thank my dog, Newton.

Publications

Can magnetar spin-down power extended emission in some short GRBs?

B. P. Gompertz, P. T. O'Brien, G. A. Wynn, A. Rowlinson

2013, MNRAS 431, 1745

Magnetar powered GRBs: explaining the extended emission and X-ray plateau of short GRB light curves,

B. P. Gompertz, P. T. O'Brien, G. A. Wynn

2014, MNRAS 438, 240

Constraining properties of GRB magnetar central engines using the observed plateau luminosity and duration correlation,

A. Rowlinson, **B. P. Gompertz**, M. Dainotti, P. T. O'Brien, R. A. M. J. Wijers, A. J. van der Horst

2014, MNRAS 443, 1779

Broad-band modelling of short gamma-ray bursts with energy injection from magnetar spin-down and its implications for radio detectability,

B. P. Gompertz, A. J. van der Horst, P. T. O'Brien, G. A. Wynn, K. Wiersema

2015, MNRAS 448, 629

Contents

1	Introduction	1
1.1	History	2
1.1.1	Extra-galactic origin	2
1.1.2	Detection in X-rays	3
1.1.3	The <i>Swift</i> era	4
1.2	The <i>Swift</i> satellite	5
1.2.1	BAT	5
1.2.2	XRT	6
1.2.3	UVOT	8
1.2.4	Other missions	8
1.3	Classification of gamma-ray bursts	9
1.3.1	Long gamma-ray bursts	10
1.3.2	Short gamma-ray bursts	11
1.3.3	Extended emission gamma-ray bursts	13
1.4	Emission mechanics	14
1.4.1	Observational constraints	15
1.4.2	Prompt emission	17

1.4.3	Afterglow	18
1.4.4	X-ray afterglow	19
1.4.5	Broadband afterglows	21
1.4.6	Central engines	22
1.5	Magnetars	24
1.5.1	Neutron stars	26
1.5.2	Field amplification	27
1.6	This thesis	28
2	The extended emission energy budget	29
2.1	Introduction	31
2.1.1	The radiation field	31
2.1.2	Larmor's formula and the dipole approximation	34
2.1.3	The NS dipole moment	36
2.2	Sample selection and data reduction	37
2.3	Evidence for a common central engine	39
2.4	The magnetar model	40
2.4.1	Magnetic dipole spin-down	40
2.4.2	The extended emission tail	48
2.5	Discussion	49
2.6	Conclusions	50

3	Magnetic propellers in EE GRBs	52
3.1	Introduction	54
3.1.1	Plasma flow in a strong magnetic field	54
3.1.2	Magnetic pressure	56
3.1.3	Ram pressure	57
3.2	Emission mechanics	58
3.2.1	Prompt emission	58
3.2.2	Extended emission	59
3.2.3	Dipole spin-down	63
3.3	Testing parameter space	64
3.3.1	Type I - ‘Humped’	65
3.3.2	Type II - ‘Classic’	67
3.3.3	Type III - ‘Sloped’	67
3.3.4	Type IV - ‘Stuttering’	68
3.4	Fitting to observation	69
3.5	Discussion	74
3.5.1	Radio emission	78
3.6	Conclusions	81
4	Broad-band modelling of magnetars in SGRBs	83
4.1	Introduction	85

4.1.1	The synchrotron spectrum	86
4.1.2	Spectral break evolution	89
4.2	Data Sample	91
4.3	Model	93
4.3.1	Synchrotron emission	94
4.3.2	Energy injection	95
4.3.3	X-ray and optical fitting	97
4.4	Modelling results	100
4.5	Modelling discussion	104
4.5.1	Energetics	107
4.5.2	Magnetar properties	108
4.6	Implications for radio emission	110
4.7	Conclusions	116
4.8	Appendix A: Flux density equations	117
5	Conclusions and future prospects	118
5.1	Key conclusions	119
5.2	The current status of the magnetar model	120
5.2.1	The weaknesses of the magnetar model	121
5.3	Consistency tests	121
5.4	Future work	122

5.4.1 The square kilometre array and the survey science era 123

5.4.2 The advent of gravitational wave astronomy 124

References **126**

List of Tables

2.1	Sample of identified EE GRBs	38
2.2	Results of fitting the magnetic dipole spin-down model	45
2.3	Results for the birth spin period derived from the extended emission energy	49
3.1	Values used to test the morphological effects of parameter variation	64
3.2	Sample fitted with the magnetic propeller model	70
3.3	Propeller fit results	74
4.1	Time dependences of the peak flux and spectral breaks in the three phases of hydrodynamical blast wave expansion	91
4.2	Test sample for broadband fitting	93
4.3	Fitting parameters selected by data constraints	98
4.4	Limits on parameters used in the order of magnitude parameter space search	99
4.5	The range of parameters found in the models that matched the data	100
4.6	Inferred radiative efficiencies and jet opening angles	108
4.7	Radio telescope detection sensitivities	110
5.1	Planned aLIGO and AdV science runs	125

List of Figures

1.1	The isotropic distribution of BATSE-detected GRBs	3
1.2	The <i>Swift</i> satellite	5
1.3	The bimodal T_{90} distribution	10
1.4	The fireball model	15
1.5	The canonical X-ray afterglow	19
1.6	Known neutron star masses	25
1.7	Neutron star equations-of-state	27
2.1	$1/R$ acceleration field	33
2.2	Overlay of all bursts with extended emission	39
2.3a	Light curves fitted with the magnetic dipole spin-down model: 050724; 051227; 060614; 061006	41
2.3b	Light curves fitted with the magnetic dipole spin-down model: 061210; 070714B; 071227; 080123	42
2.3c	Light curves fitted with the magnetic dipole spin-down model: 111121A	43
2.4	Spin period before and after extended emission vs magnetic field strength	47
2.5	The observable region of parameter space	48
2.6	Spin period vs magnetic field strength for different GRB populations	51

3.1	A toy model of a magnetic propeller	61
3.2a	Synthetic light curve classes: I - ‘Humped’ and II - ‘Classic’	65
3.2b	Synthetic light curve classes: III - ‘Sloped’ and IV - ‘Stuttering’	66
3.3a	Combined propeller-dipole fits (050724; 051227; 060614)	71
3.3b	Combined propeller-dipole fits (061006; 061210; 070714B)	72
3.3c	Combined propeller-dipole fits (071227; 080123; 111121A)	73
3.4	Magnetar birth period as a fraction of break-up period	78
3.5	Dipole field vs spin period for propeller fits	79
4.1	Example X-ray and R-band fits to the test sample GRBs	101
4.2	Radio detections and upper limits	103
4.3	Magnetar spin period and dipole field relations	109
4.4a	Radio light curve predictions at 60 MHz	111
4.4b	Radio light curve predictions at 150 MHz	112
4.4c	Radio light curve predictions at 1.4 GHz	113
4.4d	Radio light curve predictions at 15 GHz	114
4.4e	Radio light curve predictions at 100 GHz	115

1

Introduction

Gamma-Ray Bursts (GRBs) are the brightest phenomena in the known Universe, releasing as much electromagnetic energy in a few tens of seconds as the entire Milky Way galaxy does in a few years. In almost four decades of study, great advances have been made in understanding the mechanisms that power this monumental energy release; however, many questions concerning their nature are still left unanswered. This thesis will focus on a small subset of GRBs, known as extended emission (EE) GRBs because of their distinctive emission features, and how they relate to the two main broad classifications of bursts: long GRBs (LGRB) and short GRBs (SGRB). Studying these rarer features of the GRB phenomenon is very useful in elucidating the workings of the samples as a whole, because it places the progenitor under extra constraint, demanding that it accounts for both regular events, but also contains caveats to allow abnormal behaviour.

1.1 History

The first GRB was detected on the 2nd of July 1967 (GRB 670702; YYMMDD) by the *Vela* satellites. This network of United States military satellites was originally designed to monitor the skies for evidence of secret nuclear testing by the USSR, but between July 1969 and July 1972, sixteen more short bursts of gamma radiation were detected and confirmed to be neither from the Earth nor the Sun. These findings were first made public six years after the first detection (Klebesadel et al., 1973). The observed transients had durations ranging from less than 0.1 seconds to ~ 30 seconds, with time-integrated flux densities in the region of $10^{-5} - 2 \times 10^{-4}$ erg cm $^{-2}$ in the energy range 0.2 – 1.5 MeV. Theorists put forward their various conjectures on the origin of these sources, and in 1975 the review article from the Texas Symposium on Relativistic Astrophysics featured over a hundred competing theoretical models, most of which could not be ruled out by the contemporary data (Ruderman, 1975). The brief flashes of gamma emission were hard to focus, and gave few clues as to their origin. Mazets & Golenetskii (1981) noted that there appeared to be several different types of burst, with different time profiles, durations and spectral shapes, but favoured a galactic origin (as was popular at the time) due to the incredible energy release required for the source to be extra-galactic.

1.1.1 Extra-galactic origin

The origin of GRBs remained a mystery until the launch of the Compton Gamma-Ray Observatory in 1991, which allowed the first all-sky survey for high energy transients using the Burst And Transient Source Experiment (BATSE) instrument (Fishman et al., 1985). The results showed an isotropic distribution across the sky (Meegan et al. 1992; Fig. 1.1¹), ruling out the Galactic plane as their origin unless they are very close by. The broad distribution of observed fluxes made a local population unlikely, and coupled with the isotropy provided strong evidence for a cosmological

¹http://imagine.gsfc.nasa.gov/docs/science/know_12/know_bursts.html

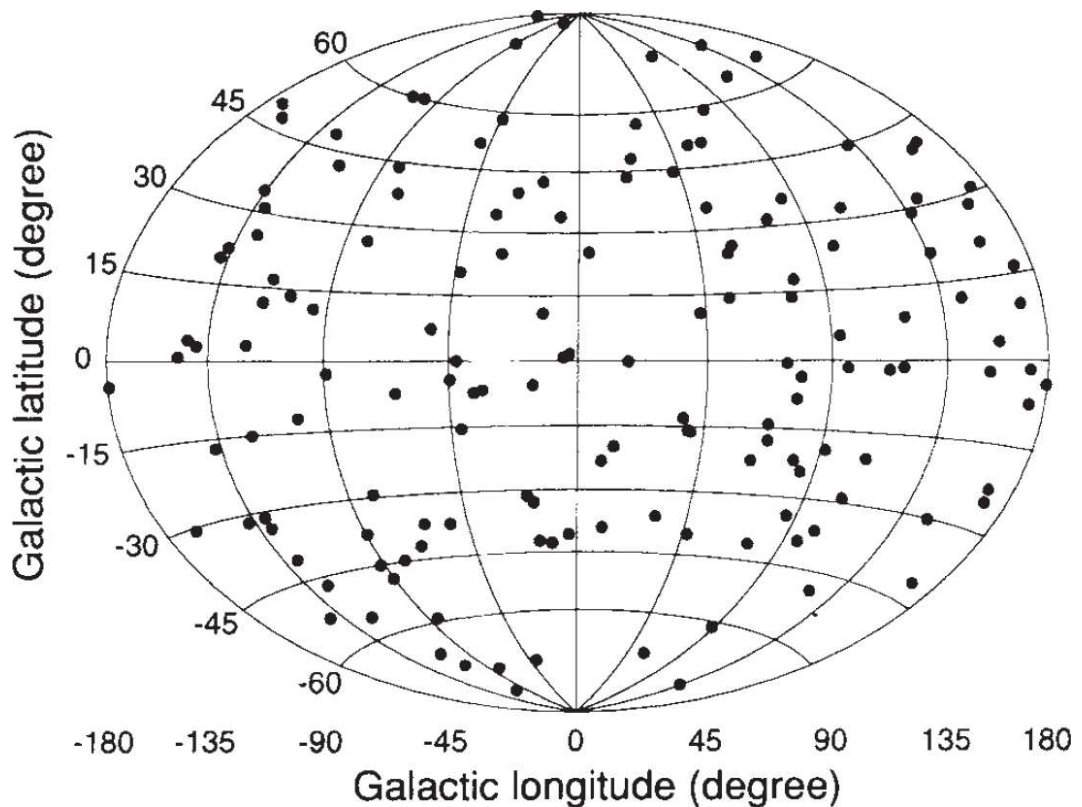


Figure 1.1: The isotropic distribution across the sky of the first GRBs detected by BATSE

source, although some models suggested a genesis in the Galactic halo. The implication of an extra-galactic source was an enormous energy release, since even at cosmological distances the bursts outshone galaxies and quasars by a very large factor.

1.1.2 Detection in X-rays

Gamma-rays are very difficult to localise with any great precision, but in 1997 the Italian-Dutch satellite *Beppo-SAX* (Boella et al., 1997) began to point its on-board X-ray telescope at GRB locations within 5 – 12 hours of the trigger time, resulting in the first X-ray afterglow detections, as well as localisations accurate to within a few arc minutes.² This enhanced positional information

²Arc minute localisations can in fact be achieved by gamma-ray imagers with coded masks, but GRB hunters were not equipped with them in the *Beppo-SAX* era.

allowed ground-based telescopes observing at various wavelengths to get in on the act, and it wasn't long before the first detection of an optical afterglow was made (van Paradijs et al., 1997), followed swiftly by the first redshift ($z \sim 0.835$; Metzger et al. 1997). This redshift identification proved that at least some GRBs occur at cosmological distances, and the burst in question (GRB 970508) was calculated to have an isotropic equivalent energy release $E_{\gamma,\text{iso}} = 7 \times 10^{51}$ erg.

1.1.3 The *Swift* era

The field of GRBs was further revolutionised in 2004 with the launch of the *Swift* satellite (Fig. 1.2; Gehrels et al. 2004). This dedicated GRB hunter was agile enough to point anywhere in the sky within around 100 seconds and able to acquire multi-wavelength observations from a single platform. Because of this, *Swift* has enabled the elucidation of GRB behaviour at times of minutes to hours after trigger, something that was previously impossible with any of the available observatories. X-ray light curves obtained by *Swift* demonstrated the smooth transition of the GRB prompt emission spike into the late-time decaying afterglow, and the first X-ray afterglow of the elusive SGRB class was detected in May 2005 (GRB 050509B), and later shown to be associated with an old elliptical host galaxy (Barthelmy et al., 2005b; Gehrels et al., 2005). The launch of *Swift* coincided with a rapid expansion of obtained redshifts, currently in excess of two hundred GRBs (Meszaros & Rees, 2014), largely due to the rapid and accurate afterglow positions the spacecraft provides. *Swift* also discovered the record holders for the most distant GRBs: $z = 8.2$ (GRB 090423; Tanvir et al. 2009) is the highest spectroscopically confirmed redshift, and $z \sim 9.4$ (GRB 090429B; Cucchiara et al. 2011) is the most distant photometric redshift, corresponding to an event that occurred over thirteen billion years ago. For a review of GRB progress in this period, see Gehrels et al. (2009); Gehrels & Razzaque (2013) and Meszaros & Rees (2014).

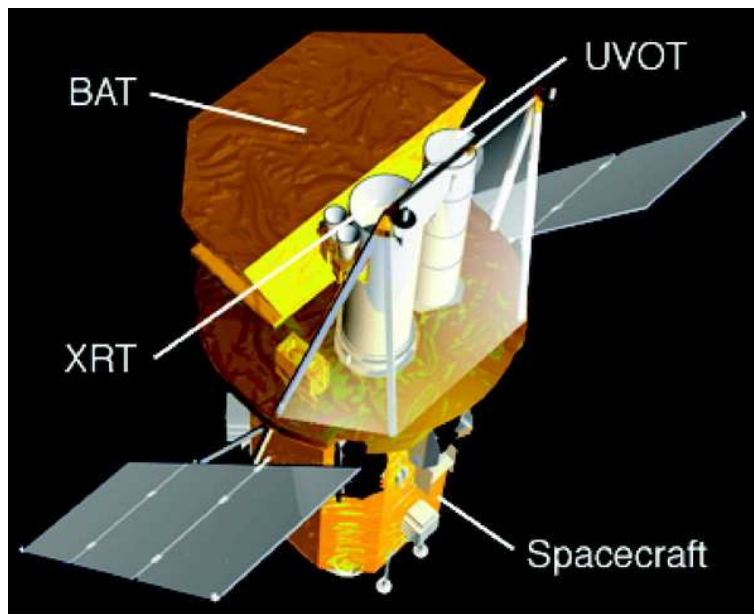


Figure 1.2: The *Swift* satellite, taken from Gehrels et al. (2004).

1.2 The *Swift* satellite

Much of the data used in this thesis was acquired by *Swift*, and so a more in-depth description of its operations than of other missions is warranted. Three instruments are carried on board: the Burst Alert Telescope (BAT; Barthelmy et al. 2005a), the X-Ray Telescope (XRT; Burrows et al. 2005) and the Ultra-Violet and Optical Telescope (UVOT; Roming et al. 2005).

1.2.1 BAT

BAT is a coded-aperture imaging telescope with a large field-of-view (FOV; 1.4 steradian half-coded). It is sensitive in the energy range 15 – 150 keV, with an energy resolution of ~ 7 keV and a fluence sensitivity of $\sim 10^{-8}$ erg cm $^{-2}$ (e.g. $\sim 10^{-9}$ erg s $^{-1}$ cm $^{-2}$ for 10 s). In normal operations, it performs an all-sky hard X-ray survey and monitors for hard X-ray transients, as well as being used to observe a series of target of opportunity (ToO) requests. A triggering algorithm constantly monitors for excesses in the detector count rate above the expected background level, mitigated

by a large number of selection criteria designed to account for varying background levels and constant sources on both short (≤ 64 ms) and long (≥ 64 ms) timescales. In addition to these rate triggers, BAT also searches for image triggers by combining the coded background snapshots the telescope automatically takes every 8 s (used for background subtraction in long rate triggers) on three different timescales in order to search for uncatalogued sources (Fenimore et al., 2003). Once triggered, on-board software identifies whether the source was significant ($> 6.5\sigma$) and uncatalogued, the position on the sky (with a 1 – 4 arcmin accuracy depending on burst intensity), and whether or not the spacecraft can safely slew to observe given the proximity of the Sun, Moon and Earth to the target field. This is all done very rapidly; the trigger alert is available after 18 (175) seconds in 50% (90%) of cases through the Tracking and Data Relay Satellite System (TDRSS; Poza 1979) and the Gamma-Ray Coordinates Network (GCN³; Barthelmy et al. 1994), followed by the burst position and the decision to slew and observe. Production of the gamma-ray light curve takes 130 seconds. *Swift* is then able to slew autonomously to point its narrow FOV instruments (XRT and UVOT) on target within around 100 seconds.

1.2.2 XRT

XRT is a sensitive, flexible, autonomous X-ray imaging spectrometer. A grazing incidence Wolter I telescope is used to focus X-rays onto a thermo-electrically cooled CCD, although the cooling system failed shortly after launch and is inoperational, meaning XRT is now ‘pointing cooled’ i.e. cooled by slewing the spacecraft so that the radiator points towards the cooler regions of the sky (away from the Sun, Moon and Earth). The instrument operates in the energy band 0.3 – 10 keV with a FOV of 23.6×23.6 arcminutes, angular resolution of 7 arcseconds (FWHM) and a detector sensitivity of 2×10^{14} erg s⁻¹ cm⁻² in 10⁴ s. XRT is able to refine the BAT localisations from 1 – 4 arcminutes to 2.5 arcseconds (usually closer to ~ 4 arcseconds with noise) just 10 seconds after target acquisition for a typical GRB, a level of precision which then allows ground-based

³Originally known as BACODINE (BATSE Coordinates Distribution Network)

telescopes to join the observations. From trigger to delivery, this information is available in just 1 – 2 minutes. XRT itself was intended to operate in 4 different observing modes; however, one of them, Photon Diode (PD) mode, was short lived due to a micrometeorite strike during the first six months of the mission. PD mode was intended for high accuracy timing use by reading the chip as if it were a single pixel, but the impact means that the signal is now swamped by noise. The three operational modes are:

1. Image Mode (IM): Used when XRT first slews to a target to give an image of the source, allowing an accurate position to be determined. Exposure times are 0.1 or 2.5 seconds, depending on source flux. Images are usually piled up due to the high source count rates encountered, and so provide no spectroscopic data, but do give good flux estimates.
2. Windowed-Timing (WT) mode: The 200 columns covering the central 8 arcminutes of the FOV are clocked continuously to provide timing information on the source, with imaging information preserved in one dimension (but lost along the other). WT mode has a 1.8 ms time resolution, and is used during slew and periods of high source flux to prevent the CCDs from becoming saturated.
3. Photon Counting (PC) mode: Uses a ‘normal’ CCD readout sequence to provide full imaging and spectroscopic resolution, but with a time resolution of only 2.5 seconds. PC mode is used once the flux has dropped below saturation levels, which usually occurs in the first few hundred seconds of a GRB. As such, PC mode is by far the most commonly used.

Data from XRT are automatically analysed by the UK *Swift* Science Data Centre (UKSSDC)⁴. Details of the analysis can be found in Evans et al. (2007, 2009).

⁴www.swift.ac.uk

1.2.3 UVOT

UVOT has a modified Ritchey-Chrétien optical configuration with a 30 cm primary mirror and an f-number of 12.7. In orbit, UVOT has imaging sensitivity comparable to a 4 m ground-based telescope. The instrument houses 2 filter wheels, both of which have 11 positions: Blocked (for detector safety), UV-grism, UVW2-filter, V-filter, UVM2-filter, optical grism, UVW1-filter, U-filter, 4x-magnifier, B-filter, White-light-filter. The filter characteristics are summarised in Roming et al. (2005) (Table 2). During slew, UVOT begins observing when a new GRB is within 10 arcmin of the target position, by default with the UVW2 filter. Once settled, UVOT creates a finding chart by taking a 100 s exposure with the V filter, which is sent to ground-based observers via TDRSS and GCN. The positional accuracy in this chart is ~ 0.3 arcseconds relative to the background stars in the FOV, and when combined with the XRT position can improve the X-ray positional accuracy to $\sim 1 - 2$ arcsec (Goad et al., 2007).

1.2.4 Other missions

Swift is not alone in its hunt for GRBs. Here, the other main operational GRB-detecting missions are summarised, though this list is far from exhaustive.

- The *Konus-Wind* instrument on board the Global Geospace Science satellite (GGW-Wind, launched in 1994; Aptekar et al. 1995) operates in the bandpass 10 keV – 10 MeV, and detects in excess of 100 GRBs per year. It is one of the satellites contributing to the Inter-Planetary Network (IPN), which uses timing analysis between pairs of satellites to triangulate GRB positions. Other current members include *Swift*, *HETE-II* and *Mars Odyssey*.
- The International Gamma-Ray Astrophysics Laboratory (INTEGRAL; Winkler et al. 1993) was launched in 2002, carrying 4 instruments on board. Its main skill (due to its high sensitivity) is identifying the population of faintest GRBs.

- *Suzaku* (Mitsuda et al., 2007) is a joint Japanese-US X-ray satellite which was launched in 2005. Its Hard X-ray Detector Wide-band All-sky Monitor (HXD-WAM, known as Suzaku-WAM; Takahashi et al. 2007) operates at 50 keV – 5 MeV, and in the first six years of observations detected more than 850 GRBs (Ohno et al., 2012), thanks in no small part to its large effective area.
- The *Fermi* satellite (Ritz et al., 2009) was launched in 2008, and carries two instruments on board. The Large Area Telescope (LAT; Atwood et al. 2009) operates in the range 20 MeV – 300 GeV, making it suitable for detecting high energy emission and peak energies (E_p), although most GRBs in its FOV are not detected. The Gamma-ray Burst Monitor (GBM; Meegan et al. 2009) provides coverage between 8 keV – 40 MeV, spanning hard X-rays right up to the more energetic gamma-rays. It typically detects a GRB every two days, which is more than *Swift*, though it lacks *Swift*'s arcsecond location accuracy.

1.3 Classification of gamma-ray bursts

Using the large sample collected by BATSE, Kouveliotou et al. (1993) were able to identify a bimodal distribution in both the temporal and spectral properties of GRB emission. These properties divide bursts into two broad classifications: long-soft and short-hard GRBs (LGRB and SGRB, respectively). The classes sit either side of a $T_{90} \sim 2$ seconds divide, where T_{90} is defined as the time in which the cumulative counts increase from 5% to 95% above the background level. SGRB spectra reveal higher peak energies than are found in LGRBs (i.e. they are spectrally harder), but it has been argued that this is a detector selection effect. For example, Sakamoto et al. (2006) showed that the *Konus* SGRB sample has a lower hardness ratio than found by BATSE, and the first two seconds of LGRBs are on average as spectrally hard as SGRBs, but then soften (Ghirlanda et al., 2004). The temporal bimodality, as observed by a number of different instruments, is shown in Fig. 1.3. The presence of such a clear dichotomy is strong evidence for two separate progenitors;

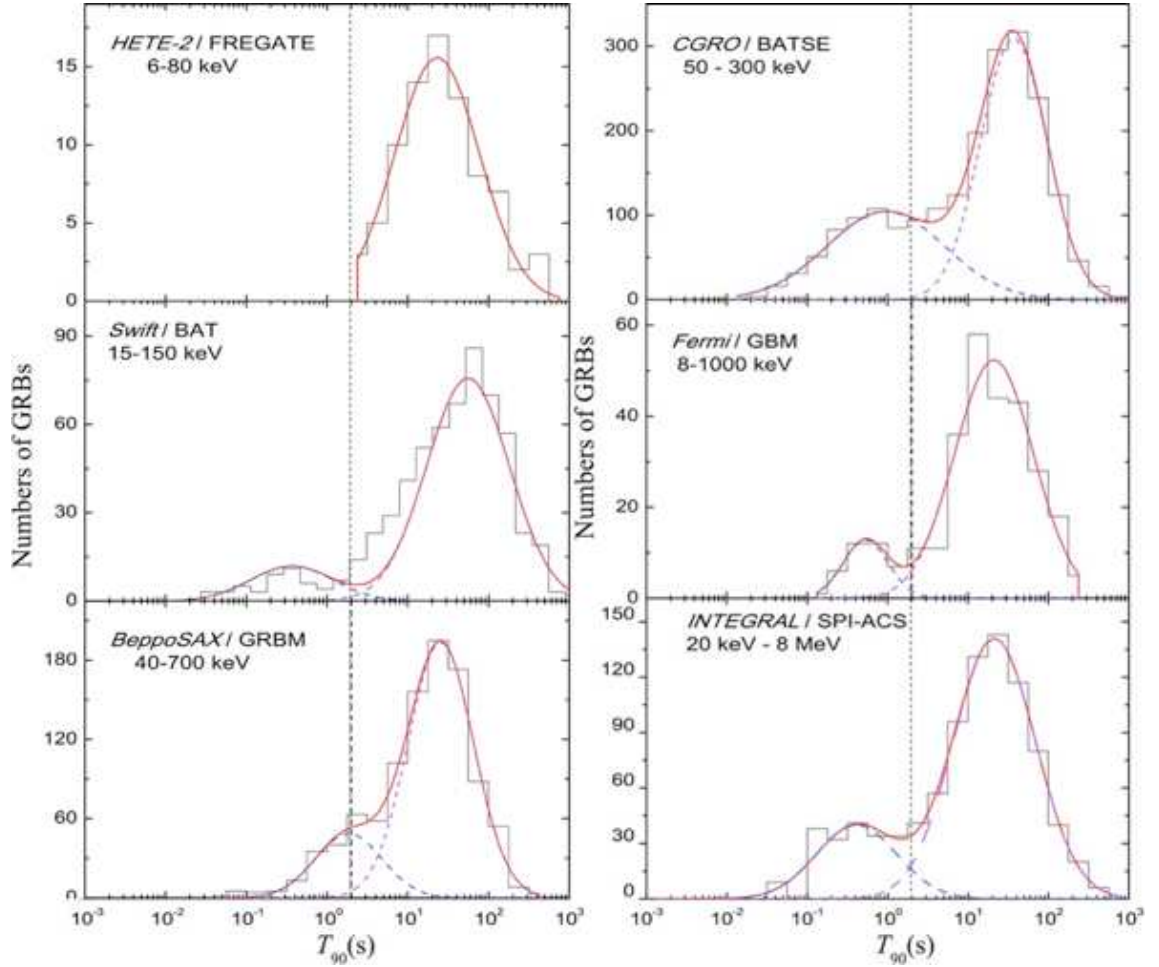


Figure 1.3: The observed bimodality in the T_{90} distribution, as seen by a variety of different instruments (Qin et al., 2013).

however, the distributions show significant overlap, indicating that a simple T_{90} cut may result in both populations being contaminated with interlopers from the tails of the opposing distribution. As a result, the T_{90} division has drawn some criticism, and alternatives have been proposed (e.g. Bromberg et al., 2013; Lü et al., 2014).

1.3.1 Long gamma-ray bursts

The first observational clues as to the genesis of LGRBs came in 1998, when supernova (SN) 1998bw was discovered in the error box of the position of GRB 980425 (Galama et al., 1998). Al-

though inconclusive at the time because the afterglow of the GRB was not seen, further supporting evidence for a GRB-supernova connection was obtained when some GRB optical afterglow light curves were found to contain small bumps at late times (e.g. Bloom et al., 1999a; Galama et al., 2000), a feature characteristic of SNe. The final piece of the puzzle fell into place in 2003 with GRB 030329, which had one of the brightest ever GRB afterglows. As the optical emission faded, a clear supernova signature (SN 2003dh) was revealed not only in the light curves, but crucially in the spectra as well (Hjorth et al., 2003; Stanek et al., 2003).

These findings are in agreement with the collapsar model (Woosley, 1993; MacFadyen & Woosley, 1999), in which LGRBs are produced during the death and subsequent core collapse of massive stars. This is further supported by the findings that LGRB host galaxies tend to be actively star forming and have moderately low metallicity (Bloom et al., 1998; Djorgovski et al., 1998; Fruchter et al., 1999; Bloom et al., 2002; Wainwright et al., 2007), since more massive stars are shorter lived and high metallicity can limit stellar growth. Population studies show that LGRBs occur in fainter, more irregular host galaxies than core-collapse SNe (Fruchter et al., 2006; Svensson et al., 2010), and closer to star forming regions, suggesting that they are associated with the deaths of the most massive stars and may be restricted to galaxies with limited chemical evolution. Conversely, some LGRBs have been found in high metallicity environments (Levesque et al., 2010a,b). Recently, Levan et al. (2014) have also proposed a new class of ‘ultra-long’ GRBs, which may be driven by the SNe of stars more diffuse than are normally considered for LGRB progenitors, or possibly by the tidal disruption of a white dwarf by a low-mass BH.

1.3.2 Short gamma-ray bursts

SGRBs are less well understood than LGRBs; they are much less frequently detected and much shorter lived, and so are still awaiting their ‘smoking gun’ equivalent of GRB 030329 for LGRBs. It is generally accepted that their origin is different from that of LGRBs because there is a clear

distinction between the spectral and temporal properties of the two classes. In particular, the absence of any observable SN in a number of deep searches is strong evidence against the collapsar model (e.g. GRB 050509B, Bloom et al. 2006; GRB 050709, Fox et al. 2005). SGRBs have been observed in a variety of host galaxies, including old ellipticals that show very little evidence of star formation (e.g. Gehrels et al., 2005), and young galaxies similar to what is seen for long bursts (e.g. D’Avanzo et al., 2009). They have also been observed with large offsets from any potential host (Berger, 2010; Tunnicliffe et al., 2014).

The favoured progenitor model for SGRBs is the merger of two compact objects (Paczynski, 1986; Fryer et al., 1999; Rosswog et al., 2003; Belczynski et al., 2006; Chapman et al., 2007). This hypothesis offers a natural explanation for the large offset between GRBs and star forming regions, because a SGRB cannot occur until both stars in the binary have evolved off the main sequence and collapsed, and the two resulting compact objects have merged. This can take up to 10^{10} years, and this long merger time, coupled with the large natal ‘kick’ velocity NSs often receive at birth (Bloom et al., 1999b; Grindlay et al., 2006) means that binary systems can be propelled to the outskirts of their host galaxies, or even expelled entirely. While it’s possible that those SGRBs seen close to star forming regions may have a collapsar origin, evolutionary channels that permit compact star mergers on short timescales are believed to exist (Belczynski et al., 2006). These associations could also be the result of natal kicks along the line of sight, which would not result in a projected offset. Further evidence supporting the compact binary merger progenitor was discovered with the detection of a possible ‘kilonova’ signature in GRB 130603B (Tanvir et al., 2013), a faint infrared transient which is believed to be due to the decay of neutron-rich radioactive species formed by the merger (Li & Paczyński, 1998).

1.3.3 Extended emission gamma-ray bursts

A possible third class of GRB was identified by Norris & Bonnell (2006), who discovered that 1/3 of their sample of SGRBs exhibited a rebrightening in their high-energy light curves that was phenomenologically and spectrally distinct from LGRB prompt emission. This ‘extended emission’ (EE) usually begins around 10 seconds after trigger, and typically has a lower flux than the prompt emission, but can last for hundreds of seconds, meaning the total fluence is often comparable (Perley et al., 2009). Some evidence of an EE component in SGRBs had been suggested in the pre-*Swift* era (Lazzati et al., 2001; Connaughton, 2002). This class of GRB poses a challenge to the long vs short dichotomy, because while its members appear to be SGRBs in terms of spectral hardness and host galaxy association, they often exhibit $T_{90} \gg 2$ seconds. EE GRBs were catalogued by Norris et al. (2010).

Central to this classification debate is GRB 060614 (Gehrels et al., 2006; Mangano et al., 2007), which had $T_{90} > 100$ seconds, but was found to be far away from the star forming region of the identified host galaxy at $z = 0.125$ (Price et al., 2006), which itself had a low star formation rate with respect to other LGRB host galaxies (Della Valle et al., 2006; Fynbo et al., 2006; Gal-Yam et al., 2006). Most damning to the LGRB connection was the lack of any identifiable SN signature, down to limits 100 times fainter than any other SN associated with a LGRB, and in fact fainter than any ever observed at all (Della Valle et al., 2006; Fynbo et al., 2006; Gal-Yam et al., 2006). The spectral lag was also identified as very short, consistent with SGRBs (Gehrels et al., 2006). Using an empirical relation between the isotropic energy and the spectral peak energy ($E_p \propto E_{\text{iso}}^{1/2}$ Amati et al., 2002; Amati, 2006), Zhang et al. (2007) generated a copy of GRB 060614 with 8 times less energy (consistent with GRB 050724, a fellow EE burst), and found that T_{90} was reduced to ~ 4.4 seconds in the BATSE bandpass, with the soft gamma-ray tails relocated to the X-ray band and a general phenomenology highly resembling GRB 050724. For these reasons, it seems likely this burst belongs to the merger population rather than the LGRB population, and that EE GRBs are more likely to be a subset of SGRBs rather than LGRBs.

A number of different mechanisms have been proposed to explain EE, including magnetar spin-down (See Section 1.4.6; Metzger et al., 2008; Bucciantini et al., 2012), a two-jet solution (Barkov & Pozanenko, 2011), fallback accretion (Rosswog, 2007), r-process heating of the accretion disc (Metzger et al., 2010), and magnetic reconnection and turbulence (Zhang & Yan, 2011).

1.4 Emission mechanics

GRB emission is traditionally divided into two broad categories: prompt emission, which refers to the initial burst of gamma-rays (sometimes including contemporaneous observations at lower frequencies), and afterglow, which effectively encompasses everything else, ranging from X-ray to radio frequencies. As pointed out by Zhang (2007), this nomenclature can be misleading; strong, hard X-ray flares can show up in gamma detectors, and under certain models the central engine that drives the prompt emission can remain active for extended periods, driving emission that could be classed as afterglow. It is therefore more physically informative to think of the emission as either ‘internal’ (i.e. driven by the central engine) or ‘external’ (i.e. originating in the medium surrounding the GRB). Here, the traditional notation is used, but the emission site is also discussed.

The broadband emission seen in both long and short GRBs can, in general, be successfully interpreted within the standard GRB fireball model (Figure 1.4; Goodman, 1986; Paczynski, 1986), which has been extensively reviewed (e.g. Piran, 1999; Mészáros, 2002; Zhang & Mészáros, 2004; Mészáros, 2006).

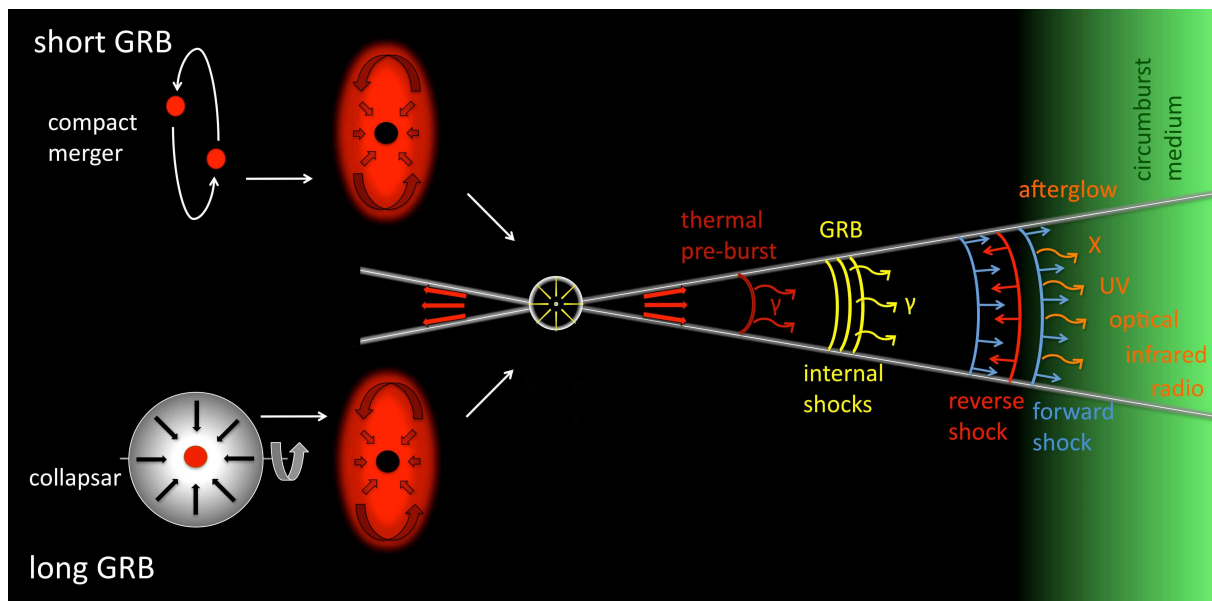


Figure 1.4: A schematic of the relativistic fireball model, taken from Gomboc (2012). The prompt and afterglow emission sites are highlighted.

1.4.1 Observational constraints

The millisecond variability observed in GRBs demands that the emission region be very compact, with an upper limit close to 1000 km (Schmidt, 1978), calculated using a simple causality argument:

$$D < c\Delta t \quad (1.1)$$

where D is the size of the emitting region, c is the speed of light and Δt is the minimum variability timescale observed. The cosmological distance of GRBs implies a gamma-ray energy release of the order 10^{52} erg, and when coupled with the required compactness of the progenitor, this demands that the radiation be extremely optically thick to pair creation, and so emit thermally with a blackbody spectrum. The observed spectra are non-thermal, a contradiction known as the compactness problem. The solution to the compactness problem is to assume that the source is

moving ultra-relativistically towards the observer, which increases the inferred size of the emission region by a factor of two times the Lorentz factor squared because the time term in Equation 1.1 should then be replaced with rest frame time. The rapid expansion of the emitting region is supported by radio observations, which were found to exhibit large-amplitude radio scintillation at early times before the signal subsequently dampened, indicating an initially small emitting region that underwent relativistic expansion (Frail et al., 1997; Goodman, 1997).

The requirement that the relativistically expanding medium be optically thin to high-energy photons places a lower limit on its bulk Lorentz factor (Γ), and similarly an upper limit can be derived from the fact that the external (afterglow) emission is absent during the prompt phase. The initial bulk Lorentz factors of the ejecta have been constrained via observation to be in the region of $\Gamma \sim 100 - 1000$ (Lithwick & Sari, 2001; Zou & Piran, 2010; Zou et al., 2011; Ghirlanda et al., 2012; Lü et al., 2012). The Lorentz factor is defined as

$$\Gamma = \frac{1}{\sqrt{1 - v^2/c^2}}, \quad (1.2)$$

so the associated ejection velocities are in the region of $0.99995c - 0.9999995c$. The Lorentz factor is a multiplicative factor when calculating relativistic mass ($m = \gamma m_0$), momentum ($p = \gamma m_0 v$) and energy (including both rest mass and kinetic energy; $E = \gamma m_0 c^2$), where m_0 is the rest mass and γ represents the Lorentz factor of an individual particle or discrete shell of ejecta.

The implied total isotropic broadband energy release can be as high as 10^{54} erg for some GRBs, a staggering output that strains the energy budget of even a compact object progenitor. This can be overcome if the outflow is collimated instead of isotropic, reducing the energy demand by a factor of 100 – 1000. This collimated outflow is supported observationally, as evidence for a jetted structure has been seen via achromatic jet breaks that manifest in the light curves (e.g. Frail et al., 1997; Harrison et al., 1999; Panaitescu & Kumar, 2001; Soderberg et al., 2006; Racusin et al.,

2009b). The relativistic outflow must be observed very close to the jet axis for the emission to trigger gamma-ray burst detectors, and so initially the emission is strongly beamed towards the observer with an opening angle $\theta = \frac{1}{\Gamma}$ (where Γ is the bulk Lorentz factor of the outflow). At this stage, the outflow cannot be distinguished from the isotropic case because all the observed emission comes from the jet cone due to beaming. As the blast wave decelerates, the Lorentz factor decreases, and so the beaming angle must increase. Once this beaming angle becomes greater than the physical opening angle of the collimated outflow, the observer can see past the jet for the first time, and starts to receive fluxes lower than the isotropic case. This causes a steepening in the light curves at all frequencies (i.e. the steepening is achromatic).

1.4.2 Prompt emission

The fireball model (Goodman, 1986; Paczynski, 1986) postulates a catastrophic event that deposits its gravitational energy into a thermally driven explosion. Internal thermal and/or magnetic pressures cause the fireball to expand and accelerate to relativistic speeds (Cavallo & Rees, 1978; Goodman, 1986; Paczynski, 1986, 1990), and the ejecta is distributed in shells which expand with a wide range of Lorentz factors. The kinetic energy of the expanding fireball is converted to electromagnetic (EM) radiation by internal shocks between shells (Rees & Meszaros, 1994), and this is generally believed to be the site of the prompt emission, although magnetic dissipation may be responsible for the prompt emission even without shocks (Zhang & Yan, 2011).

The prompt emission is typically made up of a number of Fast Rise Exponential Decay (FRED) pulses (Norris et al., 1996), sometimes referred to as the Initial Pulse Complex (IPC). The width of these pulses does not appear to evolve with time (Ramirez-Ruiz & Fenimore, 2000). LGRBs often exhibit spectral lag, meaning lower frequency photons arrive slightly later than their higher frequency counterparts. The delay in arrival times was found to be around 10 – 2000 ms between photons in the 100–200 keV and 15–25 keV bands (Ukwatta et al., 2010). SGRBs exhibit

negligible spectral lag (Norris & Bonnell, 2006; Yi et al., 2006).

Prompt emission spectra are usually fitted with the Band function (Band et al., 1993). This phenomenological model consists of a low-energy power law, with an exponential cutoff and a steeper power law at higher energies, though it is not clear what this implies physically. Hard to soft evolution is often apparent (Norris et al., 1986).

1.4.3 Afterglow

The expanding blast wave ploughs outwards into the circum-burst medium (CBM), sweeping up ambient particles as it goes. The fireball is decelerated once it has accumulated sufficient mass, entering a self-similar deceleration regime (Blandford & McKee, 1976). The deceleration radius, R_{dec} , marks the outer boundary for an emission process to be considered ‘internal’. The interaction between the blast wave and the CBM forms strong shocks at the head of the ejecta: a forward shock propagating outwards into the CBM, and a short-lived reverse shock propagating inwards back through the ejecta (Rees & Meszaros, 1992; Meszaros & Rees, 1993; Mészáros & Rees, 1997, 1999). Between them, these shocks produce the broadband afterglow.

The shock fronts radiate synchrotron emission through the action of electrons crossing the magnetised boundary between the ejecta and CBM. At early times, the energy in the shock may be so great that all the electrons are excited to states with cooling times shorter than the lifetime of the source, known as the ‘fast cooling’ regime. Once the synchrotron peak frequency, which corresponds to the minimum (and therefore most common) Lorentz factor of the electrons, has shifted below the cooling break, where the cooling time is equal to the lifetime of the source, the system has entered the far more common ‘slow cooling’ regime (Sari et al., 1998; Wijers & Galama, 1999). As the ejecta expand and cool, the peak frequency moves to increasingly long wavelengths, and will eventually slip below the self-absorption frequency, where the medium becomes optically thick, resulting in a marked decrease in luminosity.

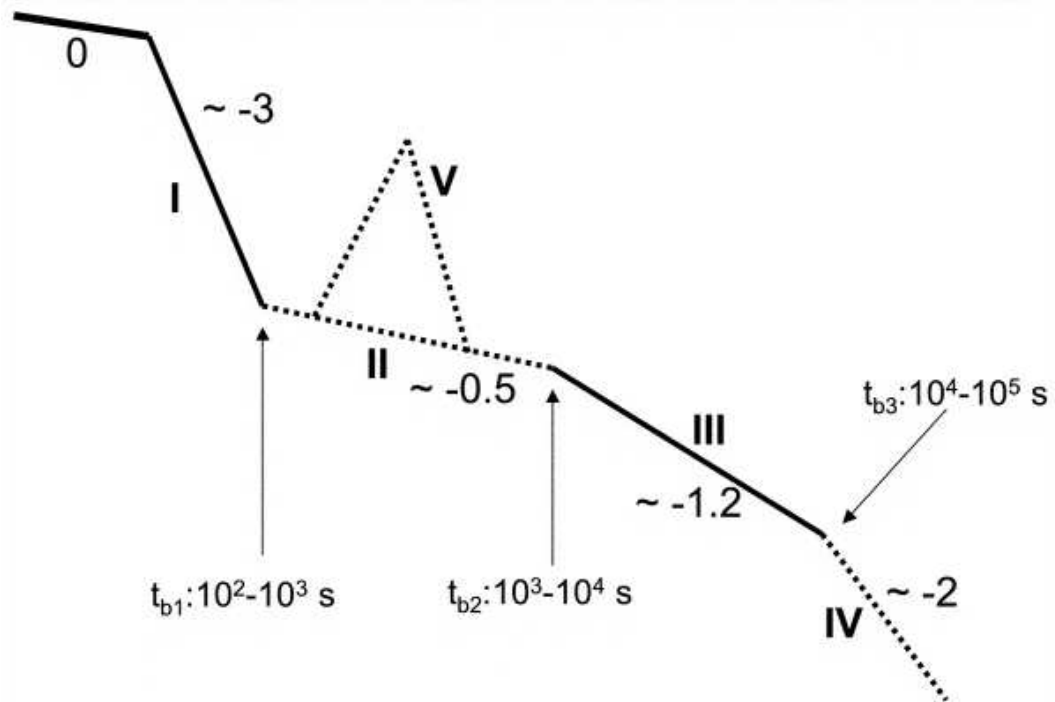


Figure 1.5: The ‘canonical’ X-ray afterglow, as presented in Zhang et al. (2006). Phase 0 denotes the prompt emission, with phases I, II, III, IV and V denoting the steep decay phase, shallow decay phase, normal decay phase, jet break, and flares, respectively. Segments I and III are the most common, and are therefore marked with solid lines. Typical temporal indices of the four power law segments are shown.

1.4.4 X-ray afterglow

The ‘canonical’ X-ray afterglow (Nousek et al., 2006; O’Brien et al., 2006; Zhang et al., 2006) is shown in Fig. 1.5, and consists of five distinct stages based on the observational data from the *Swift* XRT. There is a smooth transition between the prompt emission and afterglow phase.

1. **Steep decay phase:** Directly after the prompt emission, the X-ray afterglow decays very rapidly. This is thought to be due to the curvature effect (e.g. Kumar & Panaitescu, 2000; Dermer, 2004; Panaitescu et al., 2006; Willingale et al., 2010), where the curved shape of the emitting shell results in a noticeable range of light travel times, so that when the shell ceases to emit, the last light from high latitude regions arrives later than that from the central region, resulting in a rapidly diminishing flux as the emitting region shrinks, rather

than the sudden cutoff expected for temporally coincident cessation. The temporal decay slope predicted by the curvature effect to appear in the light curves is $\alpha = \beta + 2$, where β is the spectral index of the emission, and the flux density at a given frequency is $F_\nu = \nu^{-\beta}$.

2. **Shallow decay phase:** So-called because its temporal index is too shallow to be consistent with a forward shock decelerating in the ambient medium as predicted by the standard fireball model. This feature has been claimed as evidence for ongoing energy injection from the central engine, and is one of the features most cited in favour of the magnetar model (Fan & Xu, 2006; Rowlinson et al., 2010a, 2013). Its implication in the context of central engines is discussed in Section 1.4.6. The shallow decay phase is what is usually meant by a ‘plateau’ in the afterglow.
3. **Normal decay phase:** Unlike the previous two phases, the normal decay phase was observed pre-*Swift*. It has a typical slope of $\alpha = 1.2$, which is consistent with a decelerating shock in the slow cooling regime (Zhang et al., 2006).
4. **Jet break:** An achromatic steepening is observed in some GRBs, which is usually interpreted as the drop in flux associated with the beaming angle becoming greater than the physical opening angle of the jet, allowing the observer to ‘notice’ the jetted structure for the first time. This is further discussed in section 1.4.1.
5. **Flares:** Flaring activity has been observed in at least 47% of *Swift* GRB afterglows (Swenson & Roming, 2014). These flares are generally believed to share a common mechanism with the prompt emission (Burrows et al., 2005; Falcone et al., 2006; Curran et al., 2008; Chincarini et al., 2010; Margutti et al., 2011; Sonbas et al., 2013) because they exhibit highly comparable spectra. This implies long-lived emission or a restarting central engine, e.g. through late-time accretion, refreshed shocks, or magnetar activity.

1.4.5 Broadband afterglows

The first detection of a LGRB optical afterglow was made for GRB 970228 (van Paradijs et al., 1997), and the first SGRB detection was for GRB 050709 (Fox et al., 2005; Hjorth et al., 2005). Around 40% of *Swift* detected GRBs have optical counterparts observed by UVOT (Roming et al., 2009), with a further 20% – 30% recovered by ground-based observatories (Greiner et al., 2011). GRB optical light curves do not show the very steep decay phase observed in the X-ray band, but a shallow decay phase was observed in 39 of the 146 well-sampled optical light curves in Li et al. (2012). For both classes, a correlation has been found between the fluence of the prompt emission and the optical afterglow luminosity at a fixed time after trigger (Nysewander et al., 2009; Kann et al., 2011). For LGRBs with X-ray afterglows, Greiner et al. (2011) showed that the optical/NIR afterglow is detected in 90% (35/39 bursts in their sample) of cases when observations began within four hours of trigger. Broadband modelling of SGRBs suggests that the opening angles of the prompt emission jets are on average larger than those found in LGRBs, and that they also possess lower energies and occur in regions with lower ambient densities. The X-ray and optical light curves of 24 LGRBs were compared in Melandri et al. (2008), who found different behaviours between the two, including 10 of their sample which were inconsistent with the forward shock emission model as predicted by the standard fireball scenario.

The detection rate of GRB radio afterglows is only $\sim 30\%$ (Chandra & Frail, 2012), much lower than at X-ray ($\sim 95\%$) and optical ($\sim 70\%$) frequencies. The traditional wisdom is that this detection rate is low due to instrument sensitivities (e.g. Frail, 2005b); however, Hancock et al. (2013) have suggested that radio afterglows are intrinsically divided into two classes: *radio-bright* and *radio-faint*, with at least 30% of GRBs (the radio-faint class) having no detectable radio afterglow. Their sample of radio-bright GRBs exhibit higher gamma-ray fluences, isotropic energies, X-ray fluxes, and optical fluxes than the radio-faint class, suggesting two physically distinct populations. The radio afterglow can be significantly delayed for up to weeks or even months after trigger, because the peak frequency of the synchrotron spectrum can take a long time to pass through the

radio band (e.g. Sari et al., 1998; Wijers & Galama, 1999). A radio detection of a GRB provides a useful constraint on the isotropic energy release of the burst through radio calorimetry.

1.4.6 Central engines

The energy requirements and compactness constraints severely narrow the list of possible central engines. Candidates must be very compact, have a large energy reservoir, and be capable of launching relativistic outflows with Lorentz factors of at least ~ 100 . The two most commonly discussed central engines are accreting black holes (BH), and highly magnetised, rapidly-rotating neutron stars (NS), known as magnetars. Both of these central engines can be produced by core collapse (LGRBs; e.g. Popham et al., 1999; Dessart et al., 2008) or binary merger (SGRBs; e.g. Rosswog et al., 2003; Giacomazzo & Perna, 2013), but the discussion here focuses around the SGRB binary merger scenario.

Black hole central engine

In the BH central engine model, the merger of a NS with a stellar mass BH, or a binary NS system, leaves behind a BH of several M_{\odot} that is surrounded by an accretion disc with a mass in the range $0.01 - 1 M_{\odot}$ (Woosley, 1993; Popham et al., 1999). Jets are launched through magnetic processes, e^{\pm} pair annihilation, or neutrino interactions (Paczynski, 1991; Narayan et al., 1992; Katz, 1997; MacFadyen & Woosley, 1999; Rosswog et al., 2003; McKinney, 2006; Lei et al., 2013), tapping a small fraction of the gravitational energy of the system. Aside from possessing a plentiful supply of energy, the advantages of the BH central engine model are that the merger rate of NS-BH and NS-NS binaries in the Universe is consistent with the rate of GRBs (assuming strong beaming; Narayan et al., 1991; Phinney, 1991), and the presence of a BH helps provide a low-baryon environment, as is thought to be necessary when launching a relativistic jet.

The major disadvantage of the BH central engine is that it doesn't offer a natural cause for the late-

time flattening observed in $\sim 50\%$ (Rowlinson et al., 2013) of SGRB light curves, which is often taken to be evidence of energy injection from a long-lived central engine. This can be seen for up to 10^4 seconds after trigger, far longer than the viscous timescale for a realistic accretion disc. Several models have been put forward to correct this apparent discrepancy, including a prolonged coasting phase (Duffell & MacFadyen, 2014), fallback accretion (Rosswog, 2007), and a CBM cavity excavated by a pulsar (Holcomb et al., 2014). A refreshed shock from stratified shells of ejecta with a distribution of Lorentz factors has also been discussed (Rees & Mészáros, 1998).

Magnetar central engine

The magnetar central engine cannot be formed if one of the constituents is a BH, and so its progenitor set is more limited than in the BH case. NS binaries are typically favoured (e.g. Rosswog et al., 2003; Belczynski et al., 2006), but white dwarf binaries and the accretion-induced collapse of white dwarfs have also been suggested to contribute to the population (e.g. Chapman et al., 2007; Metzger et al., 2008). The merger remnant is a hyper-massive NS with a millisecond spin period and an intense dipole field of the order of 10^{15} G. The major success of the magnetar model is its ability to naturally explain the long-lived X-ray plateaux, which can be interpreted as energy injection into the forward shock from magnetic dipole spin-down as the rapidly-rotating NS loses angular momentum along open field lines at early times after birth (Usov, 1992; Zhang & Mészáros, 2001; Metzger et al., 2011; Rowlinson et al., 2013). The physics of magnetars is further discussed in Section 1.5.

Most of the criticism of the magnetar model centres around the prompt emission. The major issue is that, because the magnetar doesn't clear its local environment like the BH central engine does, the jet must be launched in a baryon-rich environment, and the resulting baryon loading makes it very difficult to launch jets with the requisite Lorentz factors (e.g. Drenkhahn & Spruit, 2002; Dessart et al., 2007). Simulations show that jets can be launched magnetically (e.g. Bucciantini et al., 2008, 2009, 2012), but with low Lorentz factors and for LGRB models invoking supernovae

that excavate a low density cavity, inconsistent with binary mergers. There is also significant doubt that a binary NS merger can resist collapse to a BH, although there are some recent merger simulations with a stable hyper-massive NS remnant (Giacomazzo & Perna, 2013; Hotokezaka et al., 2013). Finally, the energy available from a magnetar central engine is limited to the rotational energy of the central object, meaning that GRBs with beaming-corrected energies exceeding a few 10^{52} erg are inconsistent with the model; the available kinetic energy is approximately:

$$E_{\text{total}} \sim 3 \times 10^{52} \left(\frac{P}{1 \text{ ms}} \right)^{-2} \text{ erg} \quad (1.3)$$

where P is the spin period of the NS in ms (cf. Gao et al., 2013a; Metzger & Bower, 2014).

1.5 Magnetars

The existence of magnetars in the Milky Way Galaxy is well established through observation. Evidence comes from observations of soft gamma-ray repeaters (SGR; Norris et al., 1991), which were first detected on the 5th of March, 1979 (SGR 0526-66; Mazets et al., 1979) in the $\sim 10^4$ year old supernova remnant N49. The relative hardness and extreme luminosities of these events suggest they identify with NSs with dipole fields of the order of 10^{15} G (Thompson & Duncan, 1995), despite being millions of years old. Thompson & Duncan (1995) also present six independent arguments for a birth dipole field of the order of $\sim 10^{15}$ G for the magnetar behind the aforementioned SGR 0526-66. A number of other SGR events have been studied, and the central engines found to be magnetars with strong ($\sim 10^{14} - 10^{15}$ G) dipole fields (e.g. Kouveliotou et al., 1998, 1999; Woods et al., 1999; Esposito et al., 2010).

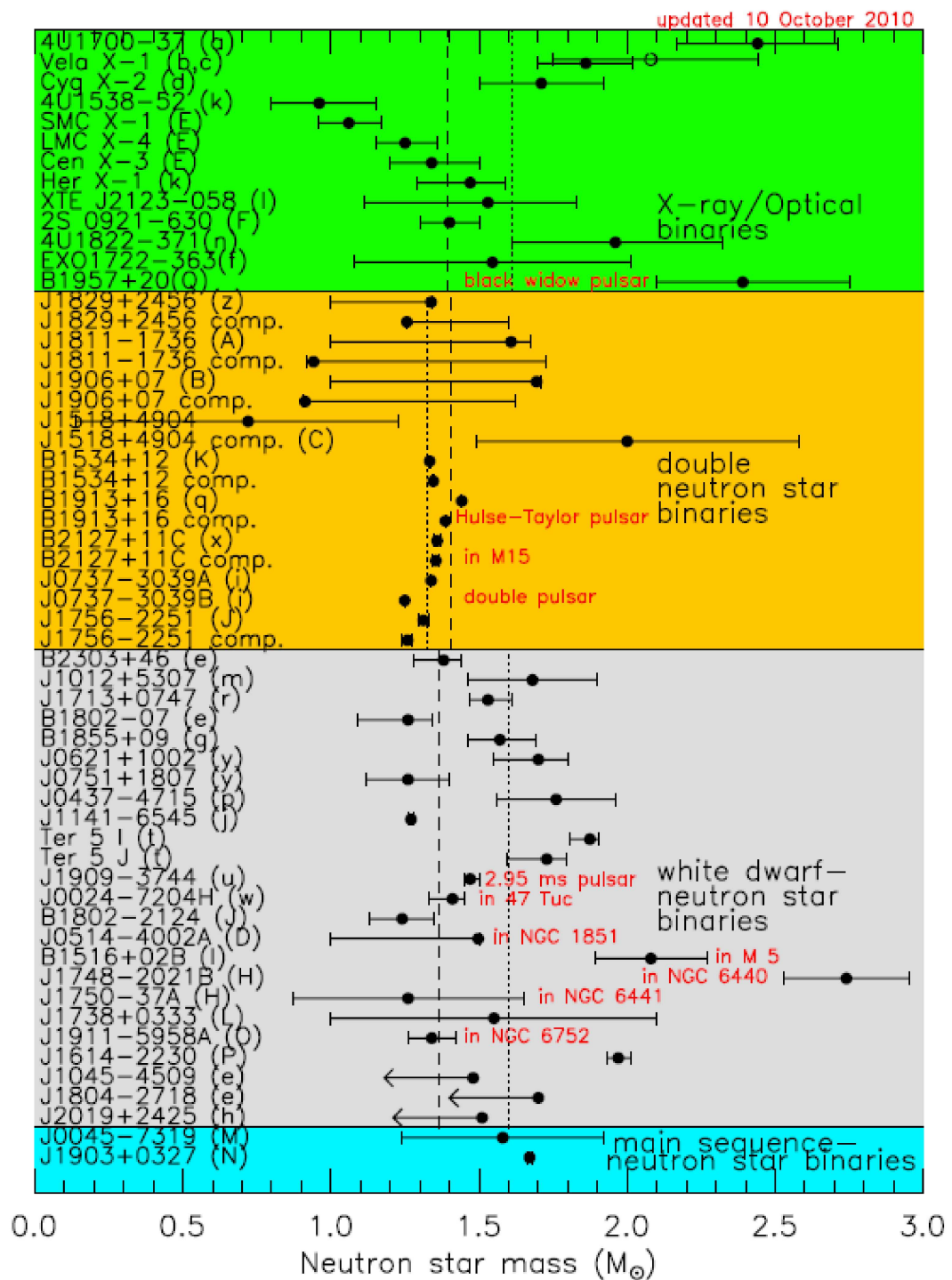


Figure 1.6: Neutron star mass measurements with $1\text{-}\sigma$ uncertainties, taken from Lattimer (2011). Uppermost region is for X-ray binaries, lowermost regions are for pulsar timing measurements. Dotted (dashed) lines indicate simple (weighted) mass averages for a region. B1516+02B and J1748-2021B do not have measured inclinations, and the error bars should be treated with caution.

1.5.1 Neutron stars

Neutron stars are most commonly created through core-collapse supernovae, but can also be formed via the accretion-induced collapse of a white dwarf. The range of known masses is $1.25 M_{\odot} - 2.01 M_{\odot}$ (Miller & Miller, 2015), which correspond to PSR J0737-3039B (Lyne et al., 2004) and PSR J0348+0432 (Antoniadis et al., 2013), respectively. The distribution of known NS masses is shown in Fig. 1.6. Accurate measurements of NS masses are vital in determining the NS equation of state, the pressure-density relation that determines the star's compressibility. A soft equation of state, indicating a more compressible composition, limits the maximum mass that can be achieved before the NS collapses to a black hole. For the scenario in which a magnetar is formed by binary merger, a reasonably hard equation of state is required, as the parent NSs are likely to have individual masses of around $1.4 M_{\odot}$, merging to form a NS in the region of $2 M_{\odot}$. Accurate mass measurements using Shapiro delay⁵ (Shapiro, 1964) have confirmed the existence of NSs in this mass range (e.g. Demorest et al., 2010). Some example NS equations of state are shown in Fig. 1.7.

Because the merger remnant will be rapidly-rotating, it also benefits from rotational support, further enhancing (at least temporarily) the maximum mass that can be formed. Uniform rotation can support a stable NS up to $1.2 \times M_{\text{max}}$ (Cook et al., 1992, 1994), where M_{max} is the maximum non-rotating mass (in M_{\odot}) allowed by the equation of state. This can be even higher if differential rotation is invoked (Baumgarte et al., 2000), or for an unstable product that will eventually collapse into a black hole. Taking the upper mass limit from Antoniadis et al. (2013), this implies a maximum stable merger remnant of $2.4 M_{\odot}$.

⁵A general-relativistic increase of light travel time through the curved space-time near a massive body, resulting in a measurable time-delay. For binary NSs, this manifests as a periodic signature in systems with a favourable inclination.

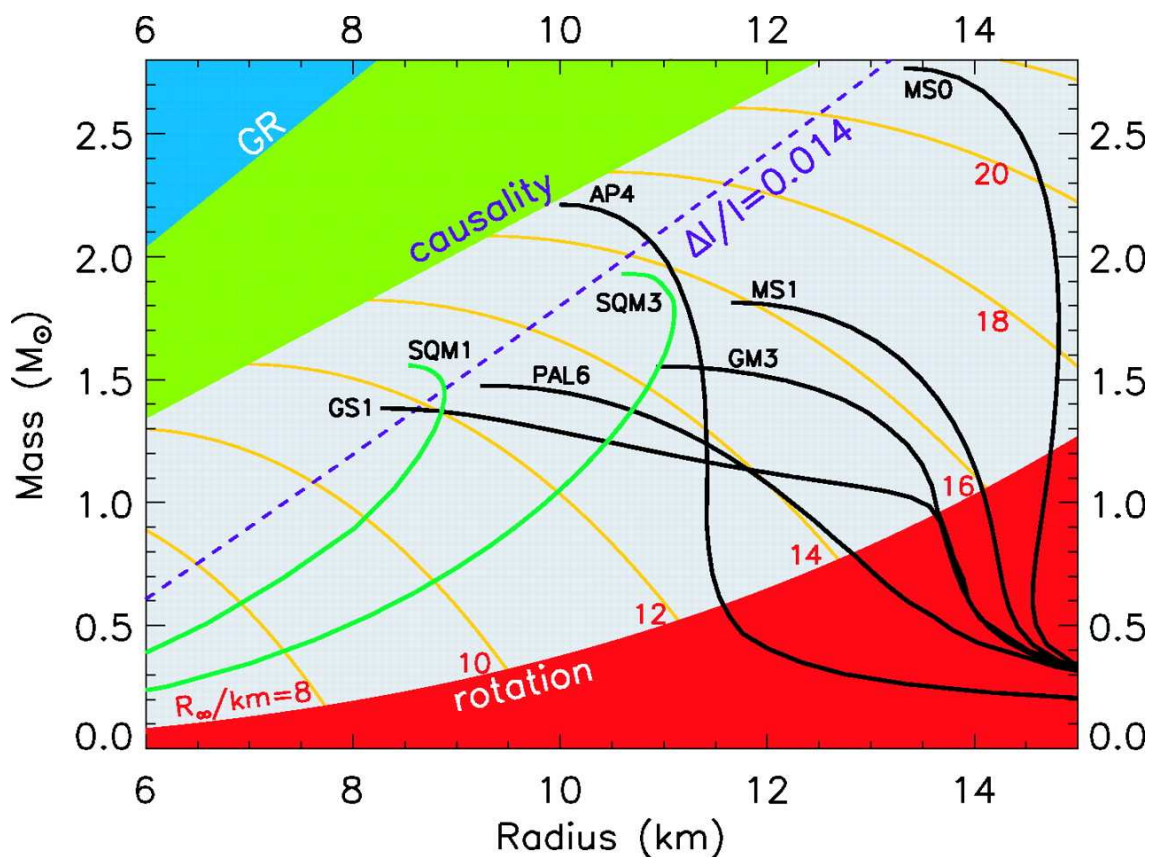


Figure 1.7: Mass-radius diagram for NSs, from Lattimer & Prakash (2004). Black (green) curves show a selection of normal (exotic) matter equations of state. Regions excluded by general relativity, causality ($v_{\text{sound}} > c$ on NS surface), and rotation (spin break-up limit) constraints are indicated.

1.5.2 Field amplification

Magnetars exhibit the strongest magnetic fields in the Universe, with surface dipole fields of the order of $10^{14} - 10^{15}$ G (e.g. Hurley et al., 2005; Palmer et al., 2005). A number of different processes have been proposed to generate these extreme values, the main ones being an $\alpha - \Omega$ dynamo (Duncan & Thompson, 1992; Thompson & Duncan, 1993), shear instabilities during compact object merger (Price & Rosswog, 2006), or magneto-rotational instabilities during core collapse (Akiyama et al., 2003; Thompson et al., 2005).

1.6 This thesis

The focus of this thesis will be on modelling the central engine and environments of EE GRBs, although some attention is paid to the SGRB class as a whole.

In Chapter 2, the sample of EE GRBs is identified, and the EE energy budget is assessed, and tested for compatibility with energy injection from a spinning-down magnetar. This is based on work originally published in Gompertz et al. (2013).

Chapter 3 is based on work published in Gompertz et al. (2014), and investigates one potential physical mechanism behind EE: a magnetic propeller, which accelerates fall-back material to super-Keplerian velocities in the aftermath of a compact binary merger that forms a magnetar. The first contiguous fits to both the extended tail and late-time X-ray afterglow are presented.

In Chapter 4, a template is developed for the expected radio signature of an expanding forward shock that is undergoing energy injection from a magnetar via magnetic dipole spin-down for both EE and SGRBs. The detectability of this signature is discussed in the context of present day and near-future radio telescopes. This is based on work originally published in Gompertz et al. (2015).

Chapter 5 recounts the key conclusions from the science chapters, and summarises our current understanding of the magnetar model. Suggestions for future work to enhance this understanding are also made.

2

Can magnetar spin-down power extended emission in some short GRBs?

This chapter presents the work originally published in Gompertz et al. (2013).

Abstract

Extended emission gamma-ray bursts are a subset of the ‘short’ class of burst which exhibit an early time re-brightening of gamma emission in their light curves. This extended emission arises just after the initial emission spike, and can persist for up to hundreds of seconds after trigger. When their light curves are overlaid, the sample of fourteen extended emission bursts show a remarkable uniformity in their evolution, strongly suggesting a common central engine powering the emission. One potential central engine capable of this is a highly magnetised, rapidly rotating neutron star, known as a magnetar. Magnetars can be formed by two compact objects coalescing, a scenario which is one of the leading progenitor models for short bursts in general. Assuming a magnetar is formed, a value for the magnetic field and late-time spin period for nine of the extended emission bursts is obtained by fitting the magnetic dipole spin-down model of Zhang & Mészáros (2001). Assuming the magnetic field is constant, and the observed energy release during extended emission is entirely due to the spin-down of this magnetar, the spin period at birth for the sample is derived. The resulting birth spin periods are in good agreement with those predicted for a newly born magnetar.

2.1 Introduction

This chapter introduces and investigates the process by which a newly-born millisecond magnetar sheds angular momentum along open magnetic field lines, known as *magnetic dipole* radiation. In systems such as those theorised for SGRBs, where jets have been launched by the merger of two compact objects and subsequently slowed by interactions with the CBM (see Section 1.4.3), the dipole emission from the NS is absorbed and reprocessed in the radiating shock that surrounds it. Magnetic dipole radiation is therefore not observed directly, but inferred from the light curves, where plateaux are seen and interpreted as energy injection from a long-lived central engine. The interpretation of the light curves, and the implications the observed plateaux hold for the central magnetar are discussed in Section 2.4.1. Here, the origin of this radiation is discussed to introduce the chapter. The derivation is based on Chapter 3 of Rybicki & Lightman (1986) and Section 10.5 of Shapiro & Teukolsky (1986).

2.1.1 The radiation field

A particle¹ at time t has conditions determined by those at the retarded time, t' . This is a light travel time concept; an observer attempting to measure conditions at a point r and time t will instead receive information propagating from point r' at the speed of light, and the actual time at which this information was emitted, t' , is the retarded time:

$$t' = t - \frac{r - r'}{c}. \quad (2.1)$$

This is a simple speed-distance-time argument. A particle at a given retarded position and time has velocity $u = \dot{r}'(t')$ and acceleration $\dot{u} = \ddot{r}'(t')$.

¹A test particle is used in this description, but is a misnomer in terms of dipole radiation from a magnetar; the field responds to conditions on the NS surface rather than a particle (or cloud of particles) orbiting around it.

The electric field induced by a particle with charge q moving with a velocity u at point r and time t is given by

$$E(r, t) = q \left[\frac{(n - \beta)(1 - \beta^2)}{\kappa^3 R^2} \right] + \frac{q}{c} \left[\frac{n}{\kappa^3 R} \wedge \{(n - \beta) \wedge \dot{\beta}\} \right], \quad (2.2)$$

where $\beta = \frac{u}{c}$, $\kappa = 1 - n \cdot \beta$ and n is the unit vector $\frac{\mathbf{R}}{R}$, where $\mathbf{R}(t') = r - r'(t')$ and $R(t') = |\mathbf{R}(t')|$. The first term is the velocity field, which falls off as $1/R^2$ and is just the generalisation of Coulomb's law to moving particles. If the particle moves with constant velocity, only this term contributes to the electric field.

The second term is the acceleration field, and falls off as $1/R$. This field is proportional to the particle's acceleration, and perpendicular to n . This electric field, and corresponding magnetic field, comprises the radiation field:

$$E_{\text{rad}}(r, t) = \frac{q}{c} \left[\frac{n}{\kappa^3 R} \wedge \{(n - \beta) \wedge \dot{\beta}\} \right], \quad (2.3)$$

$$B_{\text{rad}}(r, t) = [n \wedge E_{\text{rad}}]. \quad (2.4)$$

These properties are consistent with the radiation solutions of the source-free Maxwell equations. B_{rad} is perpendicular to both E_{rad} and n , and has a magnitude equal to E_{rad} . Figure 2.1 demonstrates how the $1/R$ decrease occurs, rather than the $1/R^2$ profile associated with a non-accelerated charge. A particle moving along the curved blue path constantly experiences an acceleration towards the centre, which translates into a linear deceleration at each position on the track. Information on this deceleration propagates outwards at the speed of light, but beyond a radius of ct the field lines are not 'informed' of the deceleration, and so the field lines beyond this limit are radial, and point towards the position that the particle would be in if no deceleration had occurred. Within ct the field lines expand radially from the true position of the particle.

For these two regions to be consistent with Gauss' law and flux conservation, they must connect through a transition region as illustrated in Figure 2.1. The radial thickness of the transition zone

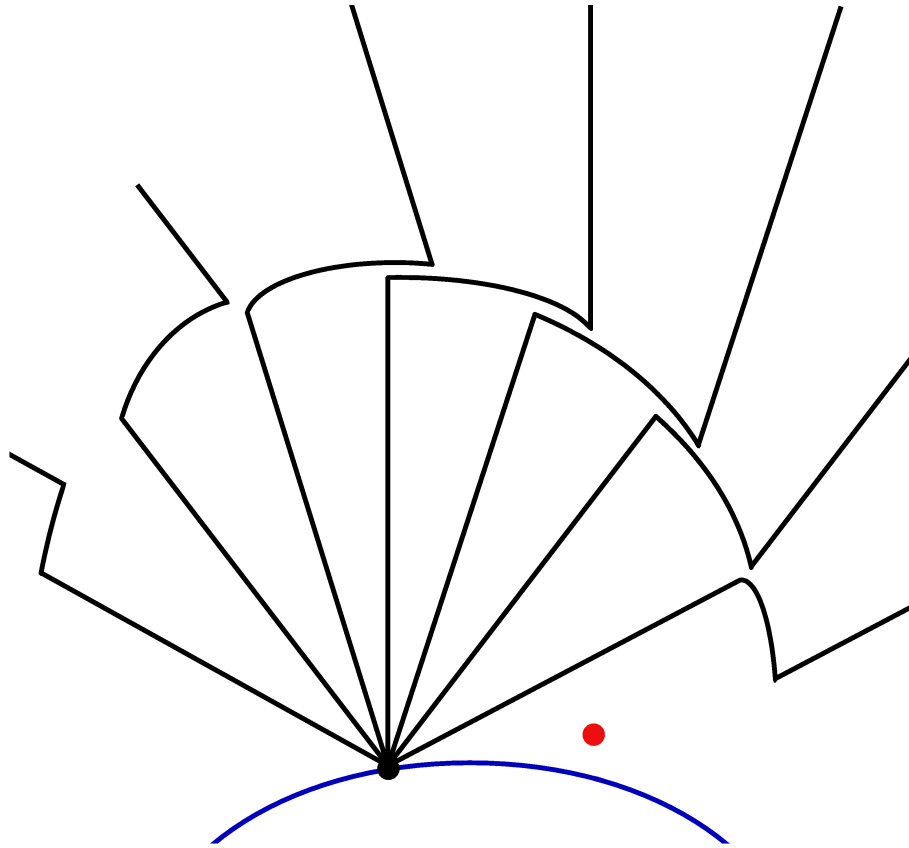


Figure 2.1: The $1/R$ acceleration field. The charged particle (black circle) follows the curved path (blue line). Curved motion describes a linear deceleration. Field lines within a radius ct ‘receive’ information of this deceleration and point towards the particle, but outside of this radius the field lines are not yet ‘informed’, and so point to where the particle would have been with no deceleration (red circle).

is the time interval over which the deceleration occurs. The number of field lines passing through the transition zone annulus is conserved, and so from geometric arguments the field intensity in this zone is proportional to $1/R$. The thickness of the annulus is constant for each wavefront, and since $R = ct$ the annulus position varies as R . The field strength is therefore proportional to $1/R$

The discussion can be specialised to the non-relativistic case, where

$$|\beta| = \frac{u}{c} \ll 1. \quad (2.5)$$

In this regime, the order of magnitude comparison between E_{rad} and E_{vel} is

$$\frac{E_{\text{rad}}}{E_{\text{vel}}} \sim \frac{R\dot{u}}{c^2}. \quad (2.6)$$

If the particle has a characteristic frequency of oscillation ν , then $\dot{u} \sim u\nu$, and equation 2.6 becomes

$$\frac{E_{\text{rad}}}{E_{\text{vel}}} \sim \frac{Ru\nu}{c^2} = \frac{u}{c} \frac{R}{\lambda}. \quad (2.7)$$

This equation shows that each field component is dominant in a different zone; the velocity field dominates a ‘near’ zone ($R \lesssim \lambda$) by a factor of $\gtrsim c/u$, whereas in the ‘far’ zone ($R \gg \lambda c/u$) the radiation field dominates, and increases its domination with increasing R .

2.1.2 Larmor’s formula and the dipole approximation

When $\beta \ll 1$, equations 2.3 and 2.4 simplify to

$$E_{\text{rad}} = [(q/Rc^2)n \wedge (n \wedge \dot{u})] \quad (2.8)$$

and

$$B_{\text{rad}} = [n \wedge E_{\text{rad}}]. \quad (2.9)$$

The magnitudes of both are given by

$$|E_{\text{rad}}| = |B_{\text{rad}}| = \frac{q\dot{u}}{Rc^2} \sin\alpha, \quad (2.10)$$

where α is the angle between the unit vector n , which is orthogonal to E and B , and the direction of acceleration. The Poynting vector is in the direction of n , and has the magnitude

$$S = \frac{c}{4\pi} E_{\text{rad}}^2 = \frac{c}{4\pi} \frac{q^2 \dot{u}^2}{R^2 c^4} \sin^2 \alpha, \quad (2.11)$$

representing an outward flow of energy in the n direction. The Poynting vector can be multiplied by the area ($dA = R^2 d\Omega$), represented by Ω at the field point, to obtain the energy (dW) emitted per unit time into a solid angle $d\Omega$ about n :

$$\frac{dW}{dt d\Omega} = \frac{q^2 \dot{u}^2}{4\pi c^3} \sin^2 \alpha. \quad (2.12)$$

The total power emitted into all angles can be obtained by integrating over all solid angles:

$$\begin{aligned} P &= \frac{dW}{dt} = \frac{q^2 \dot{u}^2}{4\pi c^3} \int \sin^2 \alpha d\Omega \\ &= \frac{q^2 \dot{u}^2}{2c^3} \int_{-1}^1 (1 - \mu^2) d\mu. \end{aligned} \quad (2.13)$$

This leads to Larmor's formula for emission from a single accelerated charge:

$$P = \frac{2q^2 \dot{u}^2}{3c^3}. \quad (2.14)$$

Obtaining the radiation field by summing the contribution from each particle is very complicated for many-particle systems because the above equations refer to the conditions at retarded times, and the retarded time will be different for each particle. However, if the typical timescale for changes within the system, τ , is much greater than the crossing time L/c , where L is the typical size of the system, then the differences in retarded times become negligible.

τ can also be characterised as the time it takes for a particle to change its motion substantially. If l is the characteristic scale of the particle's orbit, then $\tau \sim l/u$. Having $\tau \gg L/c$ then implies $u/c \ll l/L$, which is equivalent to the non-relativistic condition $u \ll c$ because $l < L$. The non-relativistic form of the radiation fields can therefore be used.

The radiation field for a system of many particles can be written as

$$E_{\text{rad}} = \sum_i \frac{q_i}{c^2} \frac{n \wedge (n \wedge \dot{u}_i)}{R_i}. \quad (2.15)$$

Evaluating the field at a large distance, R_0 , from the source means that the differences in R_i are negligible, giving

$$E_{\text{rad}} = \frac{n \wedge (n \wedge \ddot{d})}{c^2 R_0}, \quad (2.16)$$

where

$$d = \sum_i q_i r_i \quad (2.17)$$

is the electric dipole moment. This dipole approximation to Larmor's formula (equation 2.14) can then be used to express the emission from a system of multiple charges:

$$P = \frac{2\ddot{d}^2}{3c^3}. \quad (2.18)$$

By analogy with the Larmor formula for electric dipole radiation, the power radiated by a magnetic dipole is

$$P = \frac{2\ddot{m}^2}{3c^3}, \quad (2.19)$$

where m is the magnetic dipole moment. This is the source of dipole radiation discussed in this chapter.

2.1.3 The NS dipole moment

In the simplified *oblique rotator* model, the NS is assumed to rotate uniformly at a frequency Ω , with a dipole moment m oriented at an angle α to the rotation axis. m is related to the dipole field

at the magnetic pole of the star (B_p) by

$$|m| = \frac{B_p R^3}{2}, \quad (2.20)$$

where R is the stellar radius. This configuration has a time-varying dipole moment as seen from infinity, and energy is radiated away at the rate described in equation 2.19. Writing

$$m = \frac{1}{2} B_p R^3 (e_{\parallel} \cos\alpha + e_{\perp} \sin\alpha \cos\Omega t + e'_{\perp} \sin\alpha \sin\Omega t), \quad (2.21)$$

where e_{\parallel} is the unit vector parallel to the NS rotation axis and e_{\perp} and e'_{\perp} are the two other mutually orthogonal vectors, and substituting into equation 2.19, we get

$$P = \frac{B_p^2 R^6 \Omega^4 \sin^2\alpha}{6c^3}; \quad (2.22)$$

the magnetic dipole spin-down emission.

2.2 Sample selection and data reduction

The data used here were collected by the *Swift* satellite (Gehrels et al., 2004). Three instruments are carried on board: The Burst Alert Telescope (BAT; Barthelmy et al., 2005a), which has an energy range of 15 – 150 keV, the X-Ray Telescope (XRT; Burrows et al., 2005), energy range 0.3 – 10 keV and the Ultra-Violet and Optical Telescope (UVOT; Roming et al., 2005).

Raw BAT data for each burst were collected from the UK *Swift* Science Data Centre (UKSSDC) archives and processed using the *Swift* BAT pipeline tool BATGRBPRODUCT. For all EE GRBs, the BAT data were analysed by creating light curves with a variety of binning in signal-to-noise ratios (SNR) and time, looking for evidence of EE at the 3σ level where EE was consistently seen over more than 30 s. Using this method, a sample of fourteen GRBs with EE was collected,

GRB	Γ	z	Ref.
050724	1.77	0.2576 ¹	Covino et al. (2005)
050911	1.94	0.1646 ²	Page et al. (2005)
051227	1.46	2.8 ^{3a}	Barbier et al. (2005)
060614	1.79	0.1254 ⁴	Parsons et al. (2006)
061006	2.03	0.4377 ⁵	Schady et al. (2006)
061210	2.20	0.4095 ⁶	Cannizzo et al. (2006)
070714B	1.15	0.9224 ⁷	Racusin et al. (2007)
071227	1.54	0.381 ⁸	Sakamoto et al. (2007)
080123	1.99	(0.39)	Ukwatta et al. (2008)
080503	1.76	(0.39)	Mao et al. (2008)
090531B	2.07	(0.39)	Cummings et al. (2009)
090715A	1.38	(0.39)	Racusin et al. (2009a)
090916	1.57	(0.39)	Troja et al. (2009)
111121A	1.50	(0.39)	D’Elia et al. (2011)

Table 2.1: Selected sample of EE GRBs. Bracketed values for redshift, z , indicate no published value was available. In these cases the mean value of the EE sample where z is known was used. ^aupper limit. ¹Prochaska et al. (2005); ²Berger & Boss (2005); ³D’Avanzo et al. (2009); ⁴Price & Rosswog (2006); ⁵Berger (2007); ⁶Cenko et al. (2006); ⁷Graham et al. (2009); ⁸D’Avanzo et al. (2007)

including twelve which were identified as extended by Norris et al. (2010). This sample is shown in Table 2.1.

The XRT data were downloaded from the UKSSDC spectrum repository (Evans et al., 2009), and were corrected for absorption using a ratio of (counts to flux un-absorbed)/(counts to flux observed). Details of the data reduction process can be found in Evans et al. (2007, 2009). Standard HEASOFT tools were used during data reduction.

To plot the BAT data alongside the XRT, the BAT light curves were extrapolated from their 15 – 150 keV bandpass down to the XRT bandpass of 0.3 – 10 keV using a correction factor comprised of the net count rate in the 15 – 150 keV range and the extrapolated flux in the 0.3 – 10 keV range, found using a power law fit to the pre-slew BAT spectrum in XSPEC (Arnaud, 1996). These combined light curves were made by taking the 4 ms BAT light curves from the BATGRBPRODUCT pipeline and binning them with a SNR of 4, the one exception being GRB 080123, which was done with a SNR of 3. The light curves were then k-corrected, using the method described in

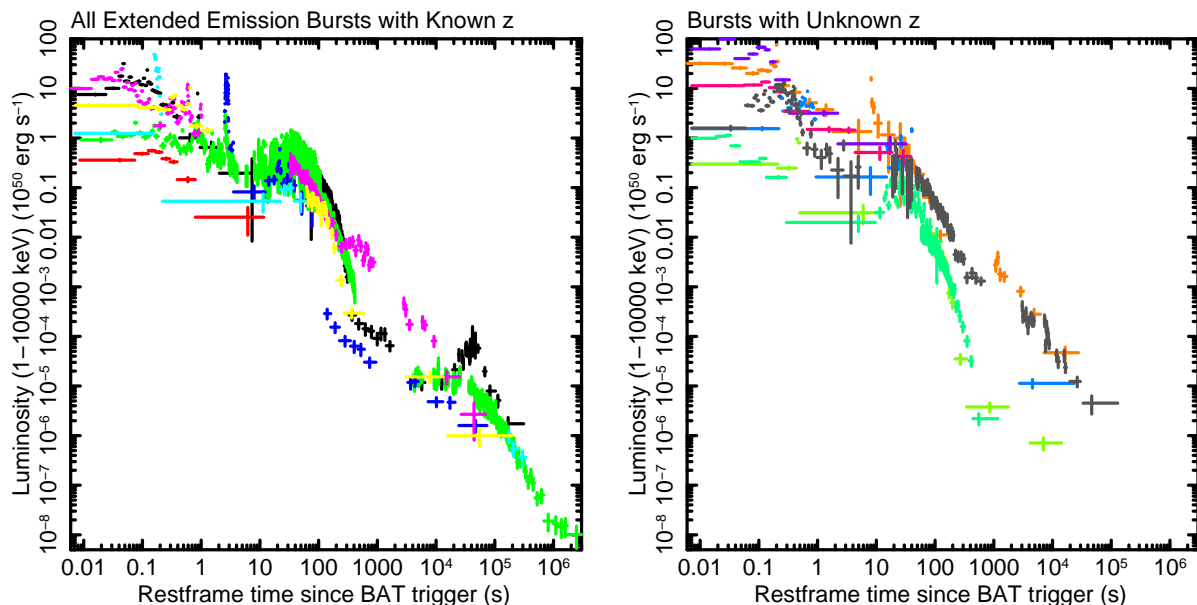


Figure 2.2: Overlay of all bursts with extended emission, showing the apparently common evolutionary path. Left: bursts with known z . Black - 050724; red - 050911; green - 060614; blue - 061006; light Blue - 061210; pink - 070714B; yellow - 071227. Right: bursts using the sample average $z = 0.39$. Orange - 051227 (Using the upper limit $z = 2.8$, D’Avanzo et al. 2009); lime Green - 080123; mint Green - 080503; blue - 090531B; purple - 090715A; red - 090916; grey - 111121A.

Bloom et al. (2001) to give bolometric (1 – 10000 keV) rest-frame light curves. The redshifts used during k-correction are displayed in Table 2.1. Where no constraints on redshift were available, the average for the sample, $z = 0.39$, was used. The value of $z = 2.8$ quoted for GRB 051227 is an upper limit (D’Avanzo et al., 2009).

2.3 Evidence for a common central engine

Fig. 2.2 shows the EE sample from Table 2.1 plotted together. The left panel shows bursts with known redshift, whilst the right panel is the rest of the sample using the mean redshift value from bursts where z is known. A striking similarity can be seen between the evolution of all EE bursts, particularly the ones where z is known. The luminosity of the individual plateaux appear to be highly comparable between bursts, and the timescales in which these plateaux turn over

also show a great deal of regularity. Such uniformity is highly suggestive of a common central engine, and hints at a unique difference between SGRBs and EE GRBs, but one that is common amongst the EE sample. One possible explanation for this uniformity is the correlation noted by Bucciantini et al. (2012) between magnetar outflow energy and jet opening angle, resulting in relatively constant isotropic power (within a factor ~ 3) for a given ejecta mass. GRB 051227 has been plotted in the right panel of Fig. 2.2, since it does not have a firm redshift. Using $z = 2.8$ gives its EE tail (the 1st plateau at around $10 \lesssim t \lesssim 100$ s) a slightly higher luminosity than those in the left panel. D’Avanzo et al. (2009) give a tentative lower limit of $z \gtrsim 0.8$, and claim that the colour observations of the possible host galaxy are consistent with those of an irregular galaxy at $z \sim 0.8$. Using $z = 0.8$ would place GRB 051227 at around the same luminosity level as the known redshift bursts in Fig. 2.2. $z = 2.8$ is used for this burst in the following analysis to place it at an extreme luminosity.

2.4 The magnetar model

2.4.1 Magnetic dipole spin-down

The magnetic dipole spin-down model is detailed in Zhang & Mészáros (2001), and has been used on both SGRBs (e.g. Fan & Xu, 2006; Rowlinson et al., 2013) and LGRBs (e.g. Troja et al., 2007; Lyons et al., 2010; Dall’Osso et al., 2011; Bernardini et al., 2012). In this chapter, the model is fitted to the the late-time plateau, seen emerging from beneath the fading EE tail in Fig. 2.3 at times of around 100 – 1000 s. This allows the magnetic field and spin period of the central magnetar to be derived, although the calculated spin period must then be corrected for spin-down during EE to get the true birth period (see Section 2.4.2).

The basic outline is that the central engine, in this case a magnetar, emits both an initial impulse

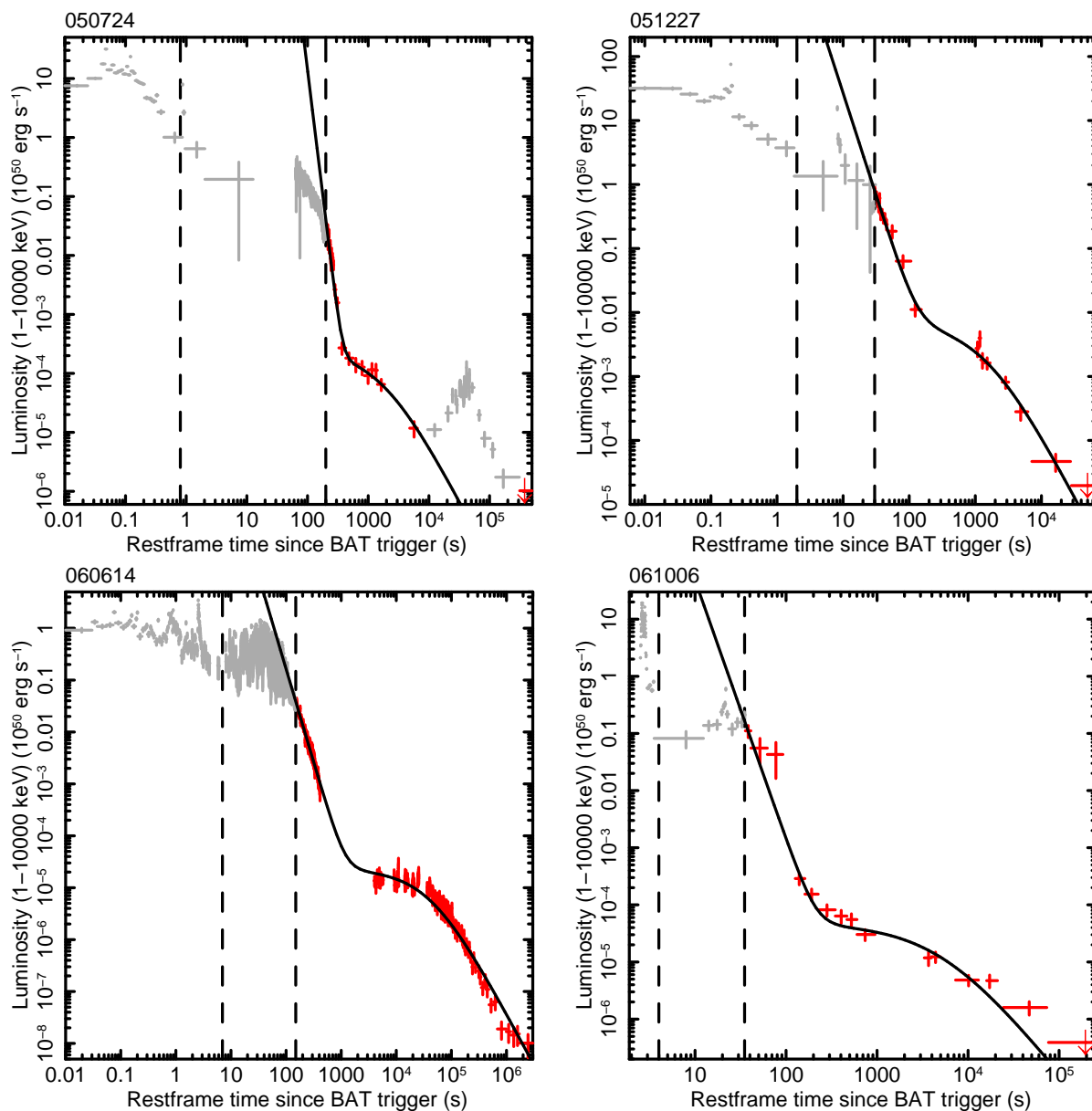


Figure 2.3a: Light curves fitted with the magnetic dipole spin-down model. Red points have been fitted to, grey points have not, most noticeably the late-time flare in GRB 050724 and the ~ 400 s flare in GRB 070714B. The vertical dashed lines indicate the extended emission region, between which extended emission energy is calculated by integrating under the curve.

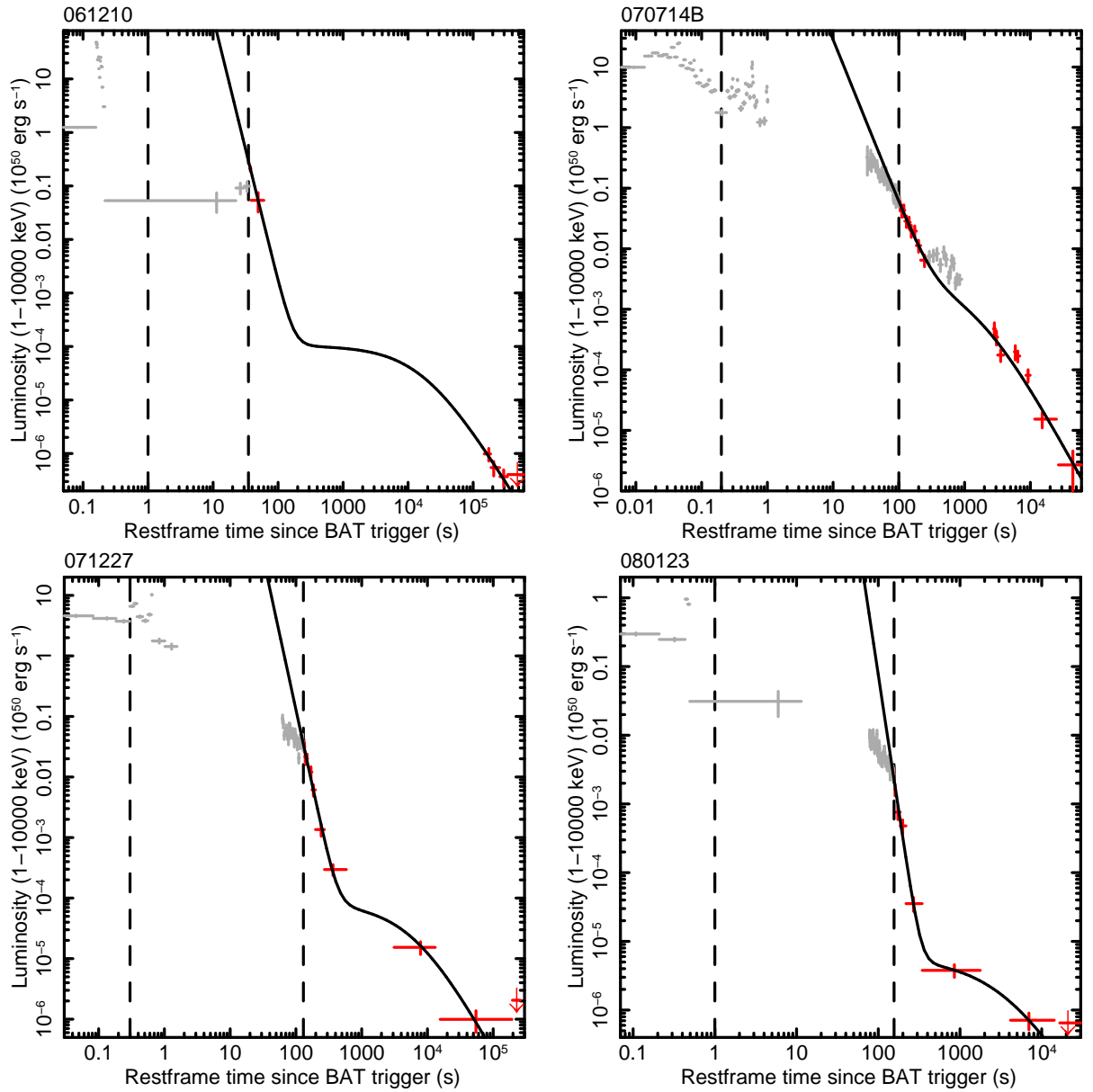


Figure 2.3b: Dipole model fits to 061210, 070714B, 071227 and 080123.

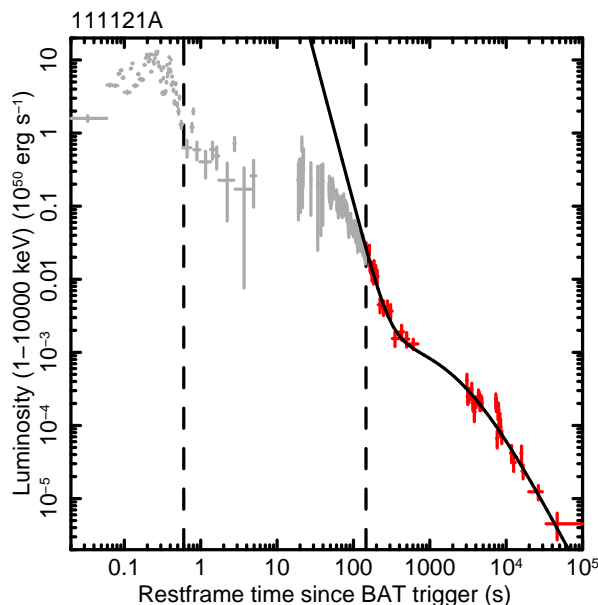


Figure 2.3c: Dipole model fit to 111121A.

energy E_{imp} as well as a continuous injection luminosity which varies as a power law in the emission time. The initial impulse energy represents the prompt emission of the burst (excluding EE), and is a short, violent event which transitions into a power law decay at very early times. The continuous injection luminosity is the product of the magnetar spinning down, and begins as soon as the magnetar is formed. Although it is present throughout, it's at a much lower level than the initial impulse, and so is initially hidden beneath the more luminous component. At a critical time, T_c , the prompt emission has faded enough so that the injection luminosity begins to dominate the light curve, causing it to flatten. This effect can be seen in the red data points in Fig. 2.3. The plateau then re-steepens after the characteristic timescale for dipole spin-down, T_{em} . At this point, the magnetar reveals itself as either unstable, collapsing into a BH with a sudden drop in the light curve, or stable, continuing to decay with a comparatively shallow power law.

To derive the parameters that control the injection luminosity plateau, the dimensions of the plateau itself must be ascertained by fitting. The area of interest for fitting is the point at which the continuous injection (dipole spin-down) luminosity emerges from beneath the initial impulse energy and the fading EE tail, shown by the red data points in Fig. 2.3. Obtaining fits that describe

the luminosity and duration of this plateau allows the magnetic field and spin period of the sample to be found. The key equations for the model are:

$$T_{\text{em},3} = 2.05 (I_{45} B_{\text{p},15}^{-2} P_{0,-3}^2 R_6^{-6}) \quad (2.23)$$

$$L_{0,49} \sim (B_{\text{p},15}^2 P_{0,-3}^{-4} R_6^6) \quad (2.24)$$

$$B_{\text{p},15}^2 = 4.2025 I_{45}^2 R_6^{-6} L_{0,49}^{-1} T_{\text{em},3}^{-2} \quad (2.25)$$

$$P_{0,-3}^2 = 2.05 I_{45} L_{0,49}^{-1} T_{\text{em},3}^{-1} \quad (2.26)$$

where $T_{\text{em},3}$ is the characteristic timescale for dipole spin-down in 10^3 s, $L_{0,49}$ is the plateau luminosity in 10^{49} erg s $^{-1}$, I_{45} is the moment of inertia in units of 10^{45} g cm 2 , $B_{\text{p},15}$ is the magnetic field strength at the poles in units of 10^{15} G, R_6 is the radius of the NS in 10^6 cm and $P_{0,-3}$ is the spin period of the magnetar in ms. The mass of the magnetar was set to $1.4 M_{\odot}$ and the radius was 10^6 cm. Using these values, the moment of inertia, I , is 9.75×10^{44} g cm 2 . Equations 2.23–2.26 are taken from Zhang & Mészáros (2001) and were combined into a QDP Component Definition (COD) file for fitting to data by Rowlinson et al. (2013) during their work. This COD file was used to obtain fits as previously in the current work. It has been assumed that emission is both isotropic and 100% efficient, since little is known about the precise emission mechanism and beaming angle. Lyons et al. (2010) discussed the effects of beaming in the context of the magnetar model, and showed that a narrower opening angle results in higher B and P (slower spin). This is illustrated by their Fig. 4.

The magnetic dipole spin-down model was fitted to the late-time data of the rest-frame light curves of nine GRBs with EE. Of the original sample of fourteen bursts, five did not contain sufficient data points for accurate model fitting and were dropped from the sample. GRB 050911, GRB 090715A and GRB 090916 do not have XRT data available, and the XRT data for GRB 090531B contains only a single point and an upper limit. GRB 080503 either has an incredibly weak dipole plateau or none at all (Perley et al., 2009), so values for magnetic field and spin period were unobtainable. Table 2.2 contains the results of the fitting to the nine remaining GRBs.

GRB	Region (s)	P_0 (ms)	B (10^{15} G)	α	Reduced χ^2
050724	≥ 200	$21.8^{+1.23}_{-1.08}$	$23.9^{+4.23}_{-3.41}$	$8.43^{+0.01}_{-0.01}$	2.71
051227	≥ 30	$4.56^{+0.27}_{-0.24}$	$5.49^{+0.64}_{-0.57}$	$3.20^{+0.22}_{-0.18}$	1.04
060614	≥ 150	$14.8^{+0.15}_{-0.14}$	$3.29^{+0.06}_{-0.06}$	$3.59^{+0.04}_{-0.04}$	1.43
061006	≥ 20	$29.1^{+1.60}_{-1.42}$	$18.4^{+3.07}_{-2.78}$	$4.53^{+0.24}_{-0.26}$	2.40
061210	≥ 35	$10.6^{+5.39}_{-7.35}$	$3.61^{+0.43}_{-0.33}$	$4.94^{+0.03}_{-0.03}$	0.57
070714B	≥ 100	$7.12^{+0.94}_{-1.04}$	$8.38^{+0.95}_{-0.85}$	$2.69^{+0.43}_{-0.31}$	1.31
071227	≥ 130	$19.9^{+2.56}_{-2.56}$	$11.3^{+4.06}_{-2.74}$	$5.02^{+0.53}_{-0.30}$	0.57
080123	≥ 156	$97.3^{+11.1}_{-8.64}$	$71.6^{+22.4}_{-15.9}$	$7.91^{+0.02}_{-0.02}$	1.95
111121A	≥ 146	$7.25^{+0.19}_{-0.22}$	$6.72^{+0.28}_{-0.32}$	$3.95^{+0.41}_{-0.36}$	1.27

Table 2.2: Results of fitting the magnetic dipole spin-down model to the sample of extended emission bursts. P_0 is the spin period after EE in ms, B is the magnetic field in 10^{15} G. α is the power law of the decay slope. All errors are 1σ .

Fig. 2.3 shows the individual fits for each of the nine bursts, along with the estimated EE region, denoted by the vertical dashed lines. The start of the EE region is taken as the first upturn in the light curve after the initial prompt emission spike. EE is said to have ceased at the time of the final power law decay before the onset of the magnetic dipole spin-down plateau. Using these definitions, the fluence ratios of Perley et al. (2009) and the EE duration times of Norris et al. (2010) are reasonably recreated. For each burst, a solution was found in which the data was accurately traced by the model, and the results returned for the values of B and P_0 lie unambiguously in allowed parameter space.

P_0 is referred to as the initial spin period of the magnetar by Rowlinson et al. (2013). Whilst this is true for short bursts where spin down only occurs due to EM dipole radiation, the story is more complicated for EE bursts. Since the assumed mechanism behind the EE tail is the extraction of rotational energy from the spin of the magnetar, the spin period during this time must be variable. In fact, during this time the magnetar may be spun up by accretion on to the surface, or down by a variety of mechanisms in addition to the constant dipole spin down that exists in the pure short GRB case. Thus, for these EE bursts, P_0 has been taken as the spin period after EE. This issue is returned to in Section 2.4.2.

The derived values of B and P_0 are plotted against each other in Fig. 2.4, where the three vertical and two horizontal lines denote allowed parameter space for the birth of a magnetar powering a GRB. The lower limit on spin period is the spin break-up frequency for a $1.4 M_{\odot}$ NS with a radius of 10 km (Lattimer & Prakash, 2004). Also plotted is the limit for a $2.1 M_{\odot}$ NS with the same radius, shown by the dashed line. These limits may vary with uncertainties in the equation of state of the NS. Usov (1992) calculated the minimum allowed spin frequency at birth if the progenitor is the accretion-induced collapse of a WD. Based on conservation of angular momentum, the upper spin period limit would be 10 ms for this type of progenitor. The minimum magnetic field required to produce a GRB observable in the gamma band (Thompson, 2007), sets the lower boundary for B at 10^{15} G. The initial impulse energy of the burst is accounted for by a power law with a decay slope α after the prompt emission. In practice, this power law simply models the light curves in the region between the EE tail and the dipole spin-down plateau. It can be seen from the results and the fits in Fig. 2.3 that all magnetars in this sample are stable.

For a dipole plateau to appear, T_{em} must be greater than T_c , otherwise the continuous injection luminosity is spent before the prompt emission has faded sufficiently for it to be observable. This places an observational constraint on the results; magnetic fields and spin periods that combine to produce very short or faint plateaux cannot be measured as they do not show up in the light curve. This constraint is even more relevant in EE GRBs than SGRBs, as the EE serves to lengthen T_c , placing a higher requirement on T_{em} . Fig. 2.5 shows the region of parameter space that is observable, with the results for B and P found by fitting plotted for reference. These results are not corrected for EE. The minimum luminosity has been set as 10^{44} erg s $^{-1}$ and minimum T_{em} as 500 s for EE GRBs, $T_{\text{em}} > 50$ s for SGRBs. These are based on inspection of the light curves, and as such are not hard limits but rather representative of likely values.

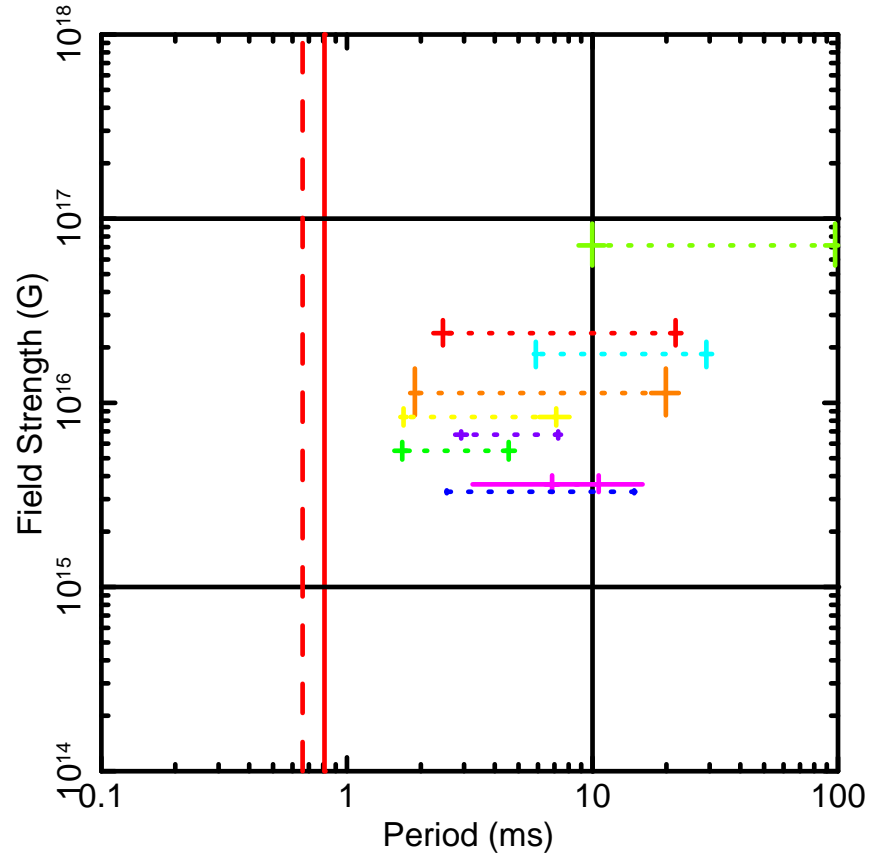


Figure 2.4: Plot of the spin period before and after extended emission against magnetic field strength. Spin period evolves from the left (P_i , birth) of the dotted lines, through extended emission, to the right (P_0). Limits (denoted by solid lines): Vertical left (red) - spin break-up frequency for a $1.4 M_{\odot}$ (solid) and $2.1 M_{\odot}$ (dashed) NS with a 10 km radius (Lattimer & Prakash, 2004); Vertical right (black) - minimum allowed spin frequency at birth, based on conservation of angular momentum during the accretion-induced collapse of a WD (Usov, 1992); Horizontal lower - minimum magnetic field required to produce a GRB observable in the gamma band (Thompson, 2007); Horizontal upper - generous limit on the maximum attainable dipole field before the onset of fast field decay (Goldreich & Reisenegger, 1992). Bursts: red - 050724; green - 051227; dark blue - 060614; light blue - 061006; pink - 061210; yellow - 070714B; orange - 071227; light green - 080123; purple - 111121A.

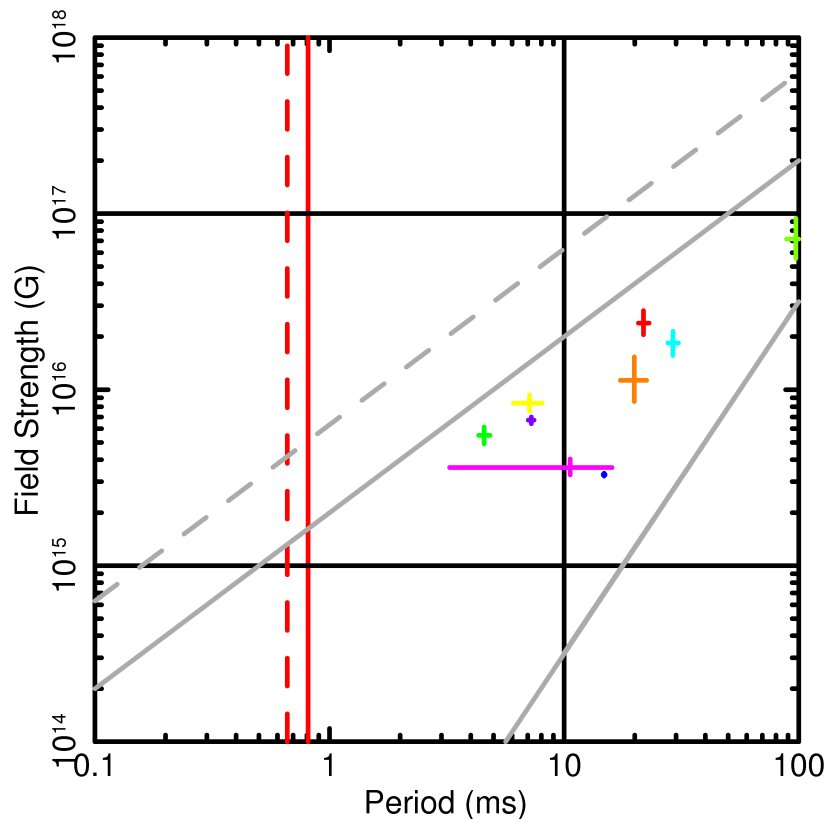


Figure 2.5: The observable region of parameter space. The lower solid grey line is the luminosity limit, set to 10^{44} erg s^{-1} . Below this line, the plateau is too faint to be observable. The upper solid grey line is the duration limit, $T_{\text{em}} = 500$ s. Above this line, T_{em} is too short to produce a plateau in the light curve; dipole emission dies away before EE has faded sufficiently for it to show up. The dashed grey line is the equivalent limit for SGRBs, based on a minimum T_{em} of 50 s. Limits and bursts as Fig. 2.4.

2.4.2 The extended emission tail

Once a fit has been found for the late-time data of a specific burst, the magnetic field strength, B , and the spin period after EE, P_0 become known quantities. The energy release of the EE tail can be calculated fairly simply by estimating the points on the light curve where EE begins and ends and integrating under the curve between these two points, ie $dE = L dt$. This is done using linear interpolation between points, and the calculated EE energies are displayed in Table 2.3. Assuming a constant magnetic field, and that energy injection during the EE period is entirely from the spin-down emission of the magnetar, the spin period the magnetar possessed at birth, P_i ,

GRB	T_{start} (s)	T_{stop} (s)	ΔE (10^{50} erg)	P_i (ms)
050724	0.8	200	31.3 ± 5.36	2.46 ± 0.21
051227	2	30	58.9 ± 8.13	1.68 ± 0.12
060614	7	150	28.7 ± 0.31	2.55 ± 0.01
061006	4	35	3.52 ± 0.11	7.17 ± 0.12
061210	1	35	2.39 ± 0.30	6.85 ± 0.43
070714B	0.2	100	62.9 ± 3.65	1.70 ± 0.05
071227	0.3	130	53.5 ± 4.40	1.89 ± 0.08
080123	1	156	1.91 ± 0.46	9.98 ± 1.20
111121A	0.6	146	18.9 ± 2.08	2.92 ± 0.16

Table 2.3: Results for the birth spin period, P_i , derived from the extended emission energy, ΔE . T_{start} and T_{stop} mark the beginning and end of the extended tail where the energy is estimated. All errors are 1σ .

can be calculated using

$$\Delta E = 2\pi^2 I (P_i^{-2} - P_0^{-2}) \quad (2.27)$$

where ΔE is the energy in the EE tail, I is the moment of inertia, P_0 is the spin period of the magnetar after EE and P_i is the birth spin period. Table 2.3 contains the results from this process, including the time boundaries for EE, the energy found by integration, and the resultant value derived for P_i .

2.5 Discussion

The calculated spin periods for the birth of the magnetar lie comfortably within allowed parameter space (Fig. 2.4) and are consistent with values predicted in the literature (Usov, 1992; Thompson et al., 2004; Chapman et al., 2007). Bursts that do not have a set redshift may vary on the energy scale, with an error of 0.5 in z roughly corresponding to an order of magnitude in the luminosity scale. Rowlinson et al. (2010a, 2013) discussed the effect of varying redshift on the results for B and P_0 in their work, and the argument is well illustrated by Fig. 9(b) in Rowlinson et al. (2013). The general result is that a higher z corresponds to a lower rotation period (ie faster spin) and lower magnetic field. A good example is the change in results if the sample average redshift $z = 0.39$

is used for GRB 051227; fitting the magnetic dipole spin-down model then gives a magnetic field of $B = 22.0_{-2.27}^{+2.54} \times 10^{15}$ G and a spin period of $P_0 = 30.2_{-1.59}^{+1.79}$ ms. The light curve is also far less luminous. The EE energy release is just $\Delta E = 1.34 \pm 0.19 \times 10^{50}$ erg, which translates into $P_i = 11.1 \pm 0.77$ ms.

Fig. 2.6 shows where the values found for B and P_i place the EE bursts relative to other SGRB and LGRB populations taken from Fig. 9(a) of Rowlinson et al. (2013). It can be seen that the EE bursts show properties that most closely resemble the unstable magnetar population of SGRBs. Since both magnetic field and spin period are very similar between these two groups, the difference must lie in some other property, perhaps mass or formation mechanism. This key difference must prevent the EE sample bursts from collapsing into BHs, and enable, perhaps even cause, the release of EE energy. Rosswog (2007) showed that accretion discs and fallback accretion exhibit a much wider spread of behaviours when the compact objects involved in the merger have different masses. In their work, a NS – NS binary showed fairly homogeneous behaviour, whilst a NS – BH merger produced a much broader spread of fallback activity. A magnetar cannot be formed from a BH, but the same principle of unequal masses can be achieved by a system involving a NS – WD merger, or, with the discovery of increasingly massive NSs (Demorest et al., 2010), possibly a more exotic NS – NS system.

2.6 Conclusions

EE GRB light curves show a remarkable uniformity when plotted alongside each other, particularly amongst the bursts where redshift is known. This consistency in plateau luminosity and turnover times suggests EE GRBs share a common progenitor mechanism which distinguishes them from ordinary SGRBs.

The magnetic dipole spin-down model of Zhang & Mészáros (2001) has been fitted to the late-

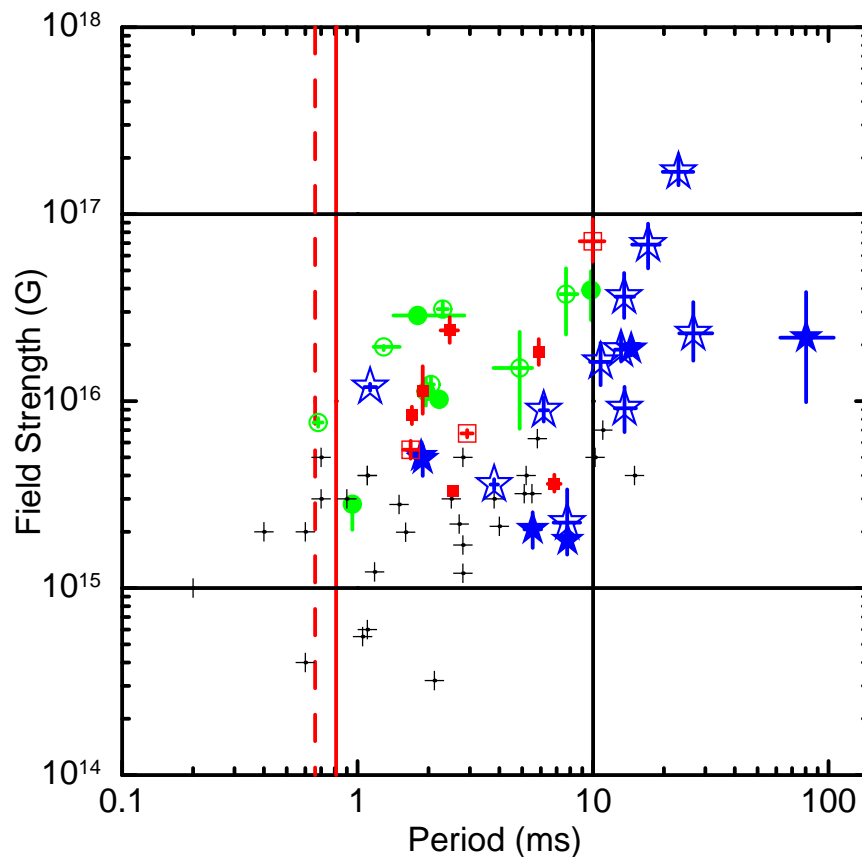


Figure 2.6: A plot of magnetic field strength versus spin period. Limits (black and red lines) as Fig. 2.4. Blue stars: stable magnetars and green circles: unstable magnetars which collapse to form a BH (Rowlinson et al., 2013). Black ‘+’ symbols are the LGRB candidates identified by Lyons et al. (2010); Dall’Osso et al. (2011); Bernardini et al. (2012). The red squares are the magnetic fields and birth spin periods (P_i) of this work. Filled symbols have observed redshifts, open symbols use the sample average redshift, which is $z = 0.39$ for EE bursts and $z = 0.72$ for the SGRBs from Rowlinson et al. (2013).

time data of the light curves of nine GRBs under the assumption that the central engine is a highly magnetised NS. These fits have yielded values for the magnetic field strength and late-time spin period. Calculations of the energy contained in the EE region of bursts in this sample have also been performed. Assuming this energy release is due to the spin-down of the central magnetar, and assuming a constant magnetic field, the spin periods these magnetars possessed at birth are inferred. The spin periods found are in good agreement with published values for the birth of a magnetar (e.g. Usov, 1992; Thompson et al., 2004; Chapman et al., 2007). These results are consistent with the idea that EE GRBs could be powered by a spinning-down magnetar.

3

Magnetar powered GRBs: Explaining the extended emission and X-ray plateau of short GRB light curves

This chapter presents the work originally published in Gompertz et al. (2014).

Abstract

Extended emission (EE) is a high-energy, early time re-brightening sometimes seen in the light curves of short gamma-ray bursts (GRBs). Here, the first contiguous fits to the EE tail and the later X-ray plateau are presented, unified within a single model. The central engine is a magnetar surrounded by a fall-back accretion disc, formed by either the merger of two compact objects or the accretion-induced collapse of a white dwarf. During the EE phase, material is accelerated to super-Keplerian velocities and ejected from the system by the rapidly rotating ($P \approx 1 - 10$ ms) and very strong (10^{15} G) magnetic field in a process known as magnetic propelling. The X-ray plateau is modelled as magnetic dipole spin-down emission. First, the range of GRB phenomena that the propeller could potentially reproduce are explored, using a series of template light curves to devise a classification scheme based on phenomenology. Fits to the light curves of nine GRBs with EE are then obtained, simultaneously fitting both the propeller and the magnetic dipole spin-down and finding typical disc masses of a few $10^{-3} M_{\odot}$ to a few $10^{-2} M_{\odot}$. This is done for ballistic, viscous disc and exponential accretion rates. The minimum conversion efficiency of kinetic energy to EM emission for propellered material is found to be $\gtrsim 10\%$ and the best fitting results come from an exponential accretion profile.

3.1 Introduction

This chapter follows on from the findings and conclusions of Chapter 2, and introduces a potential mechanism that may be responsible for converting the rotational energy of the NS into the observed EE tail. The investigated mechanism is a magnetic propeller, an effect in which the magnetic pressure of an intense dipole field exceeds the ram pressure of an incoming accretion flow, and begins to dominate its dynamical behaviour. The numerical setup required for this process to be tested against observations is introduced in Section 3.2.2, and the concept is introduced here through the derivation of the time variability of a strong magnetic field in a moving plasma. The ram pressure and the magnetic field pressure are also derived. These derivations are based on Section 3.7 of Frank et al. (2002).

3.1.1 Plasma flow in a strong magnetic field

Currents in a moving plasma will modify a magnetic field, and the field itself will act upon charges in the plasma to produce currents, so the interaction between the two can be very complicated. However, the following derivation highlights the fact that if the electrical conductivity of the plasma is sufficiently high (a condition usually realised in practice), then the plasma and magnetic field will move together, as the field becomes *frozen in* to the ionised gas.

The behaviour of a magnetic field, B , is described by Maxwell's laws. Ampere's law with Maxwell's correction is

$$\nabla \wedge B = \mu_0 J + \mu_0 \epsilon_0 \frac{\partial E}{\partial t}, \quad (3.1)$$

where J is the current density. The term $\frac{\partial E}{\partial t}$ is the displacement current, which accounts for magnetic fields induced by a time-varying electric field. In astrophysics, this can usually be neglected, leaving

$$\nabla \wedge B = \mu_0 J. \quad (3.2)$$

In the presence of an external B-field, with a conductor moving at a velocity v , the current density is related to the electromagnetic field by a form of Ohm's law appropriate to moving media, namely

$$J = \sigma(E + v \wedge B), \quad (3.3)$$

where $v \wedge B$ accounts for the current induced by the Lorentz force ($F = qv \wedge B$) on charge (q) carriers, and σ is the electrical conductivity. Substituting equation 3.3 into equation 3.2 and taking the curl of both sides then gives

$$\nabla \wedge (\nabla \wedge B) = \mu_0 \sigma (\nabla \wedge E + \nabla \wedge (v \wedge B)), \quad (3.4)$$

and the electric field term can be eliminated by applying Faraday's law ($\nabla \wedge E = -\frac{\partial B}{\partial t}$), leaving

$$\nabla \wedge (\nabla \wedge B) = \mu_0 \sigma \left(-\frac{\partial B}{\partial t} + \nabla \wedge (v \wedge B) \right). \quad (3.5)$$

A vector identity is applicable to the left hand side of equation 3.5, in the form

$$\nabla \wedge (\nabla \wedge A) = -\nabla^2 A - \nabla(\nabla \cdot A). \quad (3.6)$$

In the context of magnetic fields, this can be further simplified using another of Maxwell's equations, which states that there can be no magnetic monopoles by equating the divergence of a magnetic field to zero, or numerically

$$\nabla \cdot B = 0. \quad (3.7)$$

This identity can then be applied to equation 3.5 to get the time variability of the B-field,

$$\frac{\partial B}{\partial t} = \frac{1}{\mu_0 \sigma} \nabla^2 B + \nabla \wedge (v \wedge B). \quad (3.8)$$

The rate of change of the magnetic field is therefore governed by two terms, where the first term describes the diffusion of the field, and the second accounts for the convection of the field by the

fluid. It can be seen that the contribution from diffusion to any changes in B diminishes with increasing σ , and so in a plasma with sufficiently high electrical conductivity, diffusion can be neglected. This means that any change in the magnetic field is directly linked to the fluid flow. When the field lines and plasma flow are locked together like this, the motion of both is dictated by whichever exerts the greatest pressure.

3.1.2 Magnetic pressure

Each charge in the plasma is subject to the Lorentz force, so the magnetic force density is

$$f_{\text{mag}} = J \wedge B. \quad (3.9)$$

By re-arranging equation 3.2, and substituting to eliminate J , this becomes

$$f_{\text{mag}} = \frac{1}{\mu_0} (\nabla \wedge B) \wedge B. \quad (3.10)$$

Two further vector identities are employed here:

$$A \wedge (\nabla \wedge A) = \frac{1}{2} \nabla(A \cdot A) - (A \cdot \nabla)A \quad (3.11)$$

and

$$A \wedge B = -B \wedge A, \quad (3.12)$$

which combine to give

$$(\nabla \wedge A) \wedge A = -\frac{1}{2} \nabla(A \cdot A) + (A \cdot \nabla)A. \quad (3.13)$$

Applying the identity in equation 3.13 to equation 3.10 then gives

$$f_{\text{mag}} = \frac{1}{\mu_0} \left(-\nabla \frac{B^2}{2} + (B \cdot \nabla)B \right). \quad (3.14)$$

By comparing equation 3.14 to the Euler equation,

$$\rho \frac{\partial v}{\partial t} + \rho v \cdot \nabla v = -\nabla P + f, \quad (3.15)$$

it is apparent that the term $-\nabla \frac{B^2}{2}$ behaves like hydrostatic pressure (the $-\nabla P$ term in the Euler equation), and so by analogy the magnetic pressure is therefore

$$P_{\text{mag}} = \frac{B^2}{2\mu_0}. \quad (3.16)$$

The last term in equation 3.14 is not as important here, but describes a magnetic tension along the field lines.

The dipole field at a given radius (r) from the centre of the NS is $B = \frac{\mu}{r^3}$, where $\mu = B_* R_*^3$ is the magnetic moment of a NS with surface field strength B_* and radius R_* . The pressure experienced from the NS's dipole field at r can therefore be expressed as

$$P_{\text{mag}} = \frac{\mu^2}{2\mu_0 r^6}. \quad (3.17)$$

3.1.3 Ram pressure

The continuity equation states

$$\frac{\partial \rho}{\partial t} + \nabla \cdot (\rho v) = 0, \quad (3.18)$$

i.e. variations in density with time ($\frac{\partial \rho}{\partial t}$) are balanced by diffusion in the fluid ($\nabla \cdot (\rho v)$). For a steady state flow where $\frac{\partial \rho}{\partial t} = 0$, $\nabla \cdot (\rho v)$ must equal 0 as well. In spherical polar coordinates from the centre of a star, fluid variables are independent of θ and ϕ by spherical symmetry; the gas velocity only has a radial component. Taking this as negative to consider the infall of material, the

continuity equation reduces to

$$\frac{1}{r^2} \frac{d}{dr} (r^2 \rho v) = 0, \quad (3.19)$$

which integrates to $r^2 \rho v = \text{constant}$. Since $\rho(-v)$ is the inward flux of material, this constant must be related to the accretion rate \dot{M} :

$$4\pi r^2 \rho(-v) = \dot{M}. \quad (3.20)$$

Assuming a free-fall velocity of material,

$$v_{\text{ff}} = \left(\frac{2GM}{r} \right)^{1/2}, \quad (3.21)$$

and re-arranging equation 3.20, the ram pressure is

$$P_{\text{ram}} = \rho v^2 = \frac{\dot{M}}{4\pi r^2} \left(\frac{2GM}{r} \right)^{1/2}. \quad (3.22)$$

3.2 Emission mechanics

3.2.1 Prompt emission

Within the framework of the compact object binary merger, prompt emission is often said to be the accretion of a disc or torus onto the newly formed proto-magnetar (Narayan et al., 2001; Metzger et al., 2008, 2010; Bucciantini et al., 2012). This is assumed in this work, with the focus more on the mechanics behind the EE tail and the late-time plateau. As the compact objects spiral inwards, simulations suggest that some material (possibly up to $10^{-1} M_{\odot}$; Lee et al., 2009) is ejected by tidal disruption into a tidal tail through the outer Lagrange point. Lee et al. (2009) find that this material returns at $\sim 1 - 10$ s, and creates a new ring at a radius of around 300 – 500 km, with

a mass $M_{\text{fb}} \approx 10^{-2} M_{\odot}$. Similar behaviour was found by Rosswog (2007), who showed that the range of fallback behaviours is much more varied in an unequal mass binary. For the formation of a magnetar, this would mean a NS – WD system, or a NS binary involving a more massive NS (see e.g. Demorest et al., 2010). The result is that after the torus is accreted and prompt emission has been produced, a rapidly-rotating magnetar is left, surrounded by a $\sim 10^{-6} - 10^{-1} M_{\odot}$ accretion disc with a radial extent of a few hundred km.

3.2.2 Extended emission

The model used for EE in this chapter is the magnetic propeller model of Piro & Ott (2011) and is summarised in Fig. 3.1. The magnetic pressure for a given radius (see Section 3.1.2) is

$$P_{\text{mag}} = \frac{\mu^2}{2\mu_0 r^6}. \quad (3.23)$$

Material falling in from the accretion disc also exerts its own force, opposing that of P_{mag} . This is the ram pressure (see Section 3.1.3), given by

$$P_{\text{ram}} = \frac{\dot{M}}{8\pi} \left(\frac{2GM_*}{r^5} \right)^{1/2}, \quad (3.24)$$

where M_* is the mass of the magnetar. Equating these two pressures gives the radius at which in-falling material comes under strong influence from the dipole field, known as the Alfvén radius, r_m .

$$r_m = \mu^{4/7} (GM_*)^{-1/7} \dot{M}^{-2/7}. \quad (3.25)$$

This is one of the two key radii that determine the behaviour of the magnetar, the other being the co-rotation radius, r_c , the radius at which material orbits at the same rate as the stellar surface.

$$r_c = (GM_*/\Omega^2)^{1/3} \quad (3.26)$$

where $\Omega = \frac{2\pi}{P}$ is the angular frequency of the magnetar and P is the spin period. If $r_c > r_m$, the accretion disc is rotating more rapidly than the magnetic field at the point the field becomes dynamically important, so the effect of the interaction is to slow the material and allow it to accrete (Fig. 3.1a and 3.1b). The accreting material also spins up the magnetar, and therefore the field. If $r_c < r_m$ however, the magnetic field is spinning faster than the material, and the interaction causes particles to be accelerated to super-Keplerian velocities and ejected from the system. The magnetar loses angular momentum to the expelled material via the magnetic field and is slowed. This condition, with $r_c < r_m$, is the propeller regime (Fig. 3.1c and 3.1d). Since material cannot be accelerated to the speed of light (or above), r_m must be capped at some realistic fraction, k , of the light cylinder radius, r_{lc} . This radius marks the point at which the magnetic field lines must orbit at the speed of light to maintain their rigid rotation with the stellar surface, and is defined as

$$r_{lc} = c/\Omega. \quad (3.27)$$

The value of k naturally sets the maximum particle ejection velocity as $v = kc$.

These two regimes, propeller and accretion, both affect the spin period of the central magnetar. If $r_m > R$, the accretion torque, N_{acc} , is given by

$$N_{acc} = n(\omega)(GM_*r_m)^{1/2}\dot{M}. \quad (3.28)$$

$n(\omega)$ is the dimensionless torque, where the ‘fastness parameter,’ $\omega = \Omega/(GM_*/r_m^3)^{1/2} = (r_m/r_c)^{3/2}$ and $n = 1 - \omega$. If $r_m < R$, the torque becomes

$$N_{acc} = (1 - \Omega/\Omega_K)(GM_*R)^{1/2}\dot{M}, \quad (3.29)$$

where $\Omega_K = (GM_*/R^3)^{1/2}$. The accretion torque will spin up the magnetar when $r_m < r_c$, but goes negative in cases where $r_m > r_c$ to account for the angular momentum lost with propellered

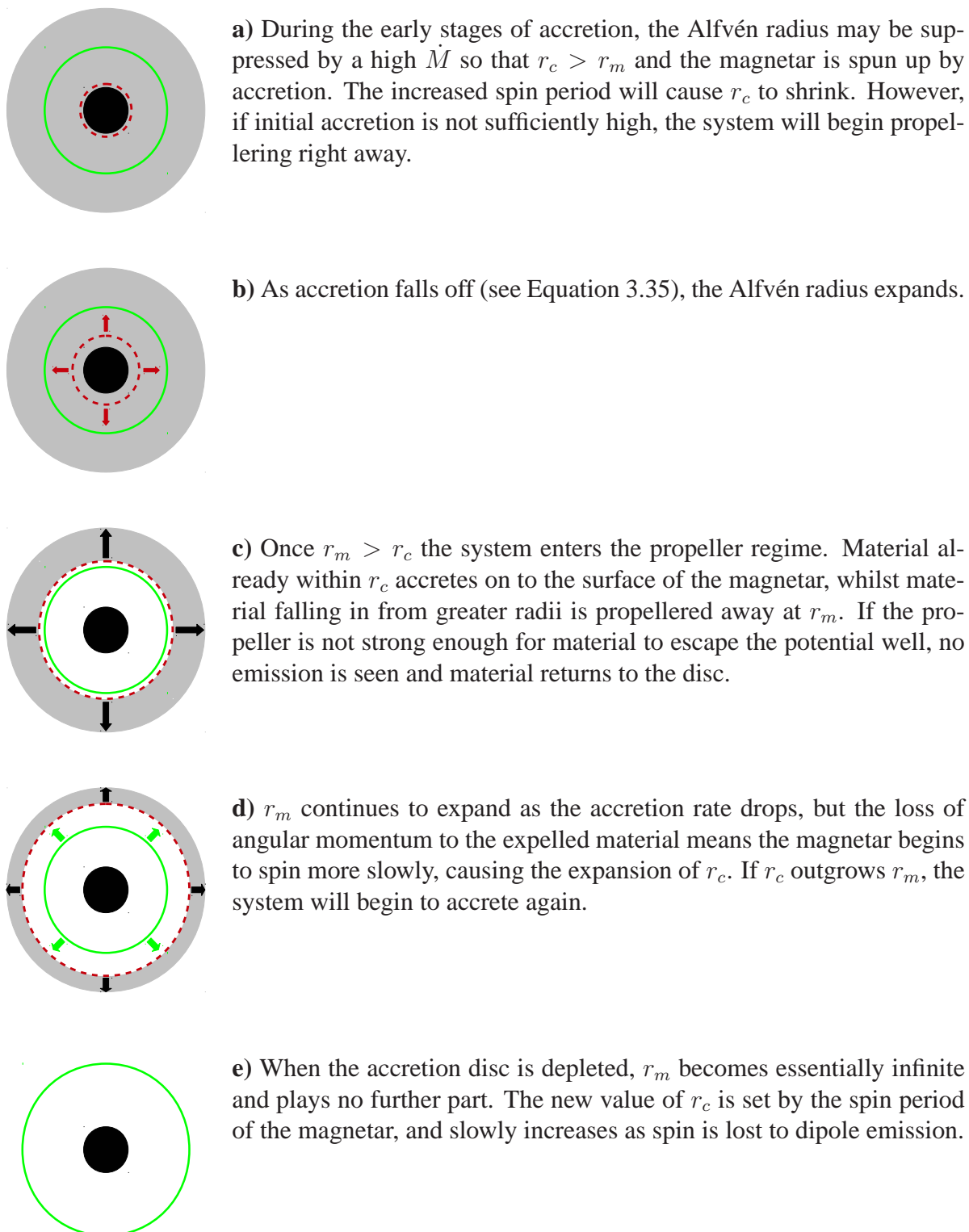


Figure 3.1: A toy model describing the interaction of the Alfvén radius (r_m) and the co-rotation radius (r_c) during the propelling and accretion regimes. The black circle is the central magnetar. The grey region represents the accretion disc. The red dashed line indicates the Alfvén radius, whilst the green solid line denotes the co-rotation radius. Not all stages may be present in an individual burst. Some may occur twice.

material. The other contribution to the torque comes from dipole spin-down, N_{dip} , and is given by

$$N_{\text{dip}} = -\frac{2}{3} \frac{\mu^2 \Omega^3}{c^3} \left(\frac{r_{\text{lc}}}{r_m} \right)^3. \quad (3.30)$$

Equation 3.30 takes into account the enhanced dipole spin-down that results from the additional open field lines created by an accretion disc truncating the magnetosphere at a radius less than r_{lc} , and is taken from Equation 2 of Bucciantini et al. (2006), who give a good discussion of this point. From these two contributions, the change in spin can be calculated by

$$\dot{\Omega} = \frac{N_{\text{dip}} + N_{\text{acc}}}{I}, \quad (3.31)$$

where $I = 0.35 M_* R^2$ is the moment of inertia. As the spin changes, the rotation parameter, $\beta \equiv T/|W|$ must be tracked, where $T = \frac{1}{2} I \Omega^2$ is the rotational energy and $|W|$ is the binding energy. The prescription from Lattimer & Prakash (2001) is used for $|W|$,

$$|W| \approx 0.6 M_* c^2 \frac{GM_*/Rc^2}{1 - 0.5(GM_*/Rc^2)}. \quad (3.32)$$

R is kept constant, even if M_* is increased by accretion, since this is consistent with most equations of state (Lattimer & Prakash, 2001). If $\beta > 0.27$, dynamical bar-mode instability will radiate or hydrodynamically readjust angular momentum, so $N_{\text{acc}} = 0$ when $\beta > 0.27$. Collecting all these terms together, the kinetic luminosity of the propeller material is

$$L_{\text{prop}} = -N_{\text{acc}} \Omega - GM_* \dot{M} / r_m. \quad (3.33)$$

The first term is the emission luminosity, and is negative because N_{acc} has been defined as negative when the magnetar is spinning down. The second term represents the energy required to escape from the gravitational potential well. This equation implicitly assumes material outflow originates from the inner edge of the disc. It therefore represents a lower limit for kinetic luminosity, as material escaping from further out will lose less energy in doing so.

A thick disc is assumed, with scale height, H , equal to the outer disc radius R_d . Fallback material returns to the disc at the ballistic fallback rate of $t^{-5/3}$, but must shed its angular momentum before accreting onto the central NS. In systems such as these, the accretion rate is commonly modelled as a viscous disc with a $t^{-4/3}$ profile (see e.g. Cannizzo et al., 2011); however, in the presence of strong outflows (Fernández & Metzger, 2013), the accretion rate will proceed as an exponential. All three accretion profiles are modelled in an effort to gauge the sensitivity of the results to them. The initial accretion rate is given the form (cf. King & Ritter, 1998))

$$\dot{M}_0 = M_d 3\nu / R_d^2, \quad (3.34)$$

where M_d is the initial disc mass and ν is the viscosity. Accretion then proceeds either as one of the two power laws mentioned above, or as an exponential decay of the form

$$\dot{M} = \dot{M}_0 e^{-3\nu t / R_d^2}. \quad (3.35)$$

3.2.3 Dipole spin-down

To explain the late-time plateau ($\sim 10^3 - 10^4$ s), the contribution to the light curve from dipole spin-down is invoked, based on the model in Zhang & Mészáros (2001). This has been done previously on LGRBs (Lyons et al., 2010; Dall’Osso et al., 2011; Bernardini et al., 2012), SGRBs (Fan & Xu, 2006; Rowlinson et al., 2013) and EE GRBs by Gompertz et al. (2013). These works assumed a constant rate of spin-down, and therefore a constant level of dipole luminosity; however, during EE the spin period may be highly variable, making this a simplified approximation. Since the evolution of the spin period in the magnetic propeller model is recorded, the time-varying equations (Zhang & Mészáros, 2001) for dipole emission can be used. The luminosity

B	($10^{15}G$)	1	5	10	50	-
P	(ms)	1	5	10	-	-
M_d	(M_\odot)	10^{-5}	10^{-4}	10^{-3}	10^{-2}	10^{-1}
R_d	(km)	100	500	1000	-	-
α		0.1	0.2	0.3	0.4	0.5
c_s	(10^7cm s^{-1})	1	2	3	-	-
M_*	(M_\odot)	1.4	2.0	2.5	-	-

Table 3.1: Values used to test the morphological effects of parameter variation. The total number of combinations resulted in 8100 synthetic light curves. B - Magnetic field; P - Spin period; M_d - Disc mass; R_d - Disc radius; α - Viscosity in the disc; c_s - Sound speed in the disc; M_* - Mass of the central magnetar.

contribution from dipole spin-down is

$$L_{\text{dip}} = \mu^2 \Omega^4 / 6c^3. \quad (3.36)$$

This emission component can be highly variable during propellering, but will settle to a constant level once the accretion disc has been consumed. As the propeller luminosity fades, L_{dip} will begin to show up in the light curve, causing the flattening seen in the late-time plateau.

3.3 Testing parameter space

To fully understand the morphological effects of the various parameters in the propeller model, the values given in Table 3.1 were assembled in every possible combination of spin period, P , magnetic field, B , disc mass M_d , disc radius, R_d , disc viscosity, α , sound speed in the disc c_s and NS mass, M_* . The result was a sample of 8100 synthetic light curves. A constant B is assumed throughout the duration of each, and the efficiency of both the propeller and dipole emission was set at 100% since it serves only to normalise the luminosity in these cases. k was set to 0.9.

Initially, 540 light curves (all combinations of P , B , M_d , R_d and M_* with a constant $\alpha = 0.1$ and $c_s = 10^7 \text{cm s}^{-1}$) were examined in order to determine a classification system based on

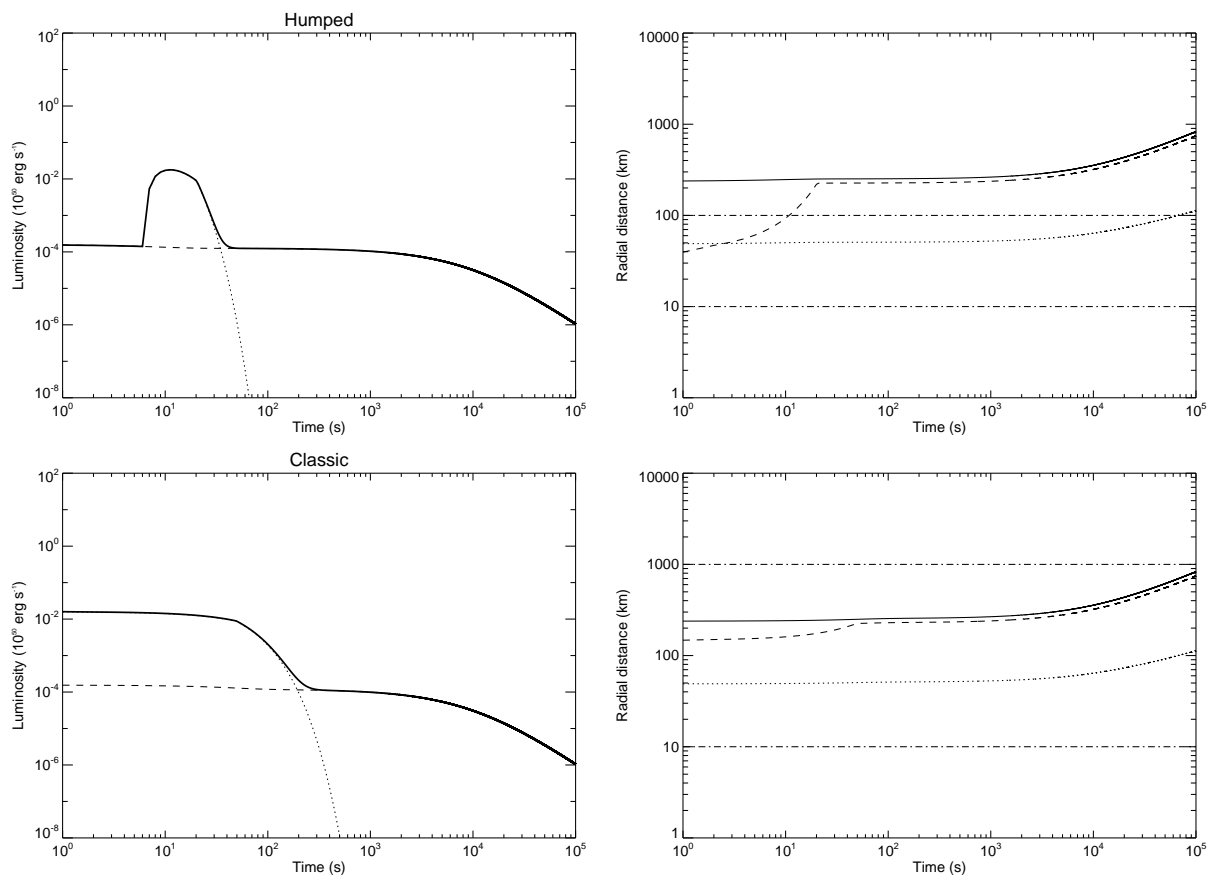


Figure 3.2a: Top to bottom: Type I - ‘Humped’; Type II - ‘Classic’. Each row shows plots for one example of one class. Intended to highlight phenomenology only; they are not fully representative of the full range of morphology or energetics of their respective classes. These light curves do not contain the prompt spike. Left: synthetic light curves representing the four identified phenomenological classes. Dotted line - propeller luminosity. Dashed line - dipole luminosity. Right: dotted (dashed) line shows the position of the co-rotation (Alfvén) radius in km against time. Solid line shows the position of the light cylinder radius. Lower dot-dash line is the magnetar radius, upper dot-dash line is the outer disc radius.

phenomenology. After inspection, four clear types were identified. Example light curves of each type can be seen in Fig. 3.2. Note that these light curves do not contain the prompt emission spike.

3.3.1 Type I - ‘Humped’

A ‘Humped’ burst is born without propelling, initially powered by dipole emission alone (although this would be hidden beneath the prompt emission). As they progress, conditions for the

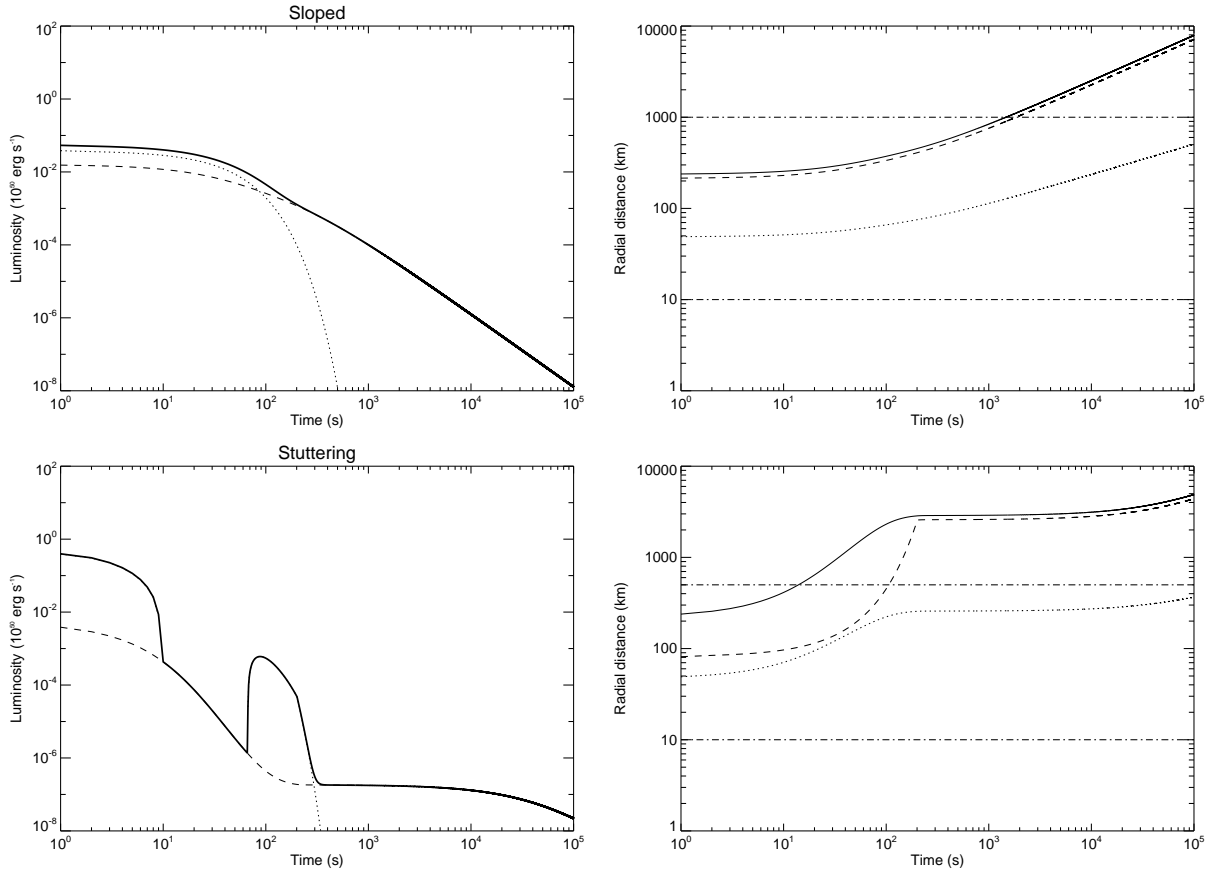


Figure 3.2b: continued. Top to bottom: Type III - ‘Sloped’; Type IV - ‘Stuttering’.

initiation of propellering are met, and the light curve is given a ‘hump’ by the rapid rise to prominence of the propeller luminosity. Propellering can be delayed like this for one of two reasons:

- \dot{M} is high and/or P is low so that $r_c > r_m$ and the system is in the accretion regime.
- \dot{M} is high and/or P is low enough that material cannot escape the potential well and Equation 3.33 is negative, despite $r_m > r_c$.

These two possibilities can be distinguished by their light curves; bursts with strong initial accretion display a rising dipole luminosity at early times as the magnetar is spun up, whereas bursts with propellers too weak to enable matter to escape the potential well have flat dipole luminosity

profiles at early times (e.g. Fig. 3.2). 152 of the 540 synthetic bursts (28%) are type I.

3.3.2 Type II - ‘Classic’

The ‘Classic’ type can be formed by some combination of almost all parameters. They exhibit a relatively flat and well-defined propeller plateau, transitioning into a relatively flat and well-defined dipole plateau. In the extremes of parameter space (e.g. very high B and low P), the other types are usually more prevalent, but a type II can still be formed given the right conditions. The division between this class and the type I or III bursts is rather loose, highlighting the smooth transition of parameters into ‘extreme’ regimes. This class could also be further sub-divided into those experiencing rapid spin-down (shown by descending L_{dip} at early times) and those which are comparatively stable (flat L_{dip} at early times, see Fig. 3.2). The divide between these is a combination of initial spin P and the properties of the accretion disc; fast spinners spin down more rapidly, particularly when \dot{M} is high, as this boosts the accretion torque. 202 of the 540 synthetic bursts (37%) are type II.

3.3.3 Type III - ‘Sloped’

‘Sloped’ bursts are the result of the dipole component contributing strongly or even dominating the light curve during the propeller regime. In these cases, the two emission components appear to act as one, resulting in a poorly defined dipole plateau and a single component look to the light curve. This comes about when B is high and/or spin is rapid, which are the conditions required for strong dipole emission. These types actually have the most powerful potential propellers, which is shown when the disc is small or loosely bound; In these conditions, L_{prop} can rise above the already highly luminous L_{dip} , creating the brightest type II (Classic) bursts seen. A sloped burst may not be recognised as extended when observed, and would instead be classified as either a

LGRB or SGRB. If accretion discs with increasingly low masses are considered, this could be the dividing point between EE GRBs and SGRBs. 63 of the 540 synthetic bursts (12%) are type III.

3.3.4 Type IV - ‘Stuttering’

Light curves in the final burst category begin with propeller-like behaviour like a type II, but this rapidly vanishes after a few tens of seconds. After a short dipole-only phase, again lasting a few tens of seconds, the propeller is reborn, creating a hump much like a type I. The main factors governing this behaviour are B and M_d . A high disc mass means that \dot{M} is initially high. Propeller-like behaviour can still occur, due to the high magnetic field, but spin is lost rapidly through the accretion torque until it is too slow to power effective propeller-like behaviour. At this point, L_{prop} shuts off and the light curve proceeds on L_{dip} alone. In the absence of propeller-like behaviour, the rate of spin-down is greatly reduced, so that as the accretion rate begins to drop, the propeller makes a revival in much the same way as the type I bursts do. If the prompt emission is particularly strong or lasts a long time, a type IV may be observationally indistinguishable from a type I. Of the 540 synthetic bursts, 68 are type IV (13%).

In addition to the four classes, a total of 22 bursts (4%) did not produce detectable propeller emission (i.e. the emission was less luminous than that of the dipole), and a further 33 (6%) were unclassified due to incoherent and unrealistic light curves. These were exclusively bursts with the maximum (5×10^{16} G) magnetic field, indicating that magnetic fields much greater than this probably do not create EE GRBs; even at this B , particular conditions are required to produce a light curve in the correct energy region.

The parameters α and c_s were then re-introduced as variables. As expected, no new phenomenological classes were identified, and no existing classes dropped out. The overall effect was a greater range of morphologies within each class, specifically a general shortening/contraction of

propeller regimes with increased α and/or c_s , and a slight elevation of peak luminosity.

It is clear from the results in Fig. 3.2 that the propeller model is capable of producing a variety of phenomena similar to those seen in GRB light curves, and given that we have restricted the behaviour of the fallback disc by requiring that it is fully formed and accreting at $t = 0$, it seems likely the range is even greater. Piro & Ott (2011) have investigated the role propeller might play in the supernovae that power LGRBs, and Bernardini et al. (2013) suggest it as a source of the precursor emission seen in some of the BAT6 sample. In addition, the smooth nature of propeller emission means it could conceivably reproduce the giant flares seen in some bursts (e.g. Burrows et al., 2005). It may also be capable of uniting SGRBs with EE GRBs, as discussed in Section 3.5.

3.4 Fitting to observation

The data sample to be used in fitting was taken from Gompertz et al. (2013). Only bursts for which a value for B and P were found are included, and a constant B for the duration of each light curve is assumed. Table 3.2 lists the sample of nine EE GRBs used. The model was written in IDL and made use of MPFIT (Markwardt, 2009). Initial guesses for B and P during fitting were taken from Gompertz et al. (2013)¹. These parameters were left fixed, leaving a two parameter fit comprised of M_d and R_d . If no suitable fit was obtained then P was set as a free parameter. If a fit was still not forthcoming, B was unfrozen and allowed to vary as well. For all fits, The central magnetar was $1.4 M_\odot$ with a radius of 10 km. α was held at 0.1 and c_s as 10^7 cm s^{-1} . The conversion efficiency of kinetic energy to EM radiation in propellered material was set to 40%, and the dipole efficiency to 5%. k , the maximum fraction of r_{lc} allowed for r_m , was 0.9. Some flares were excluded from the fits. One at around a thousand seconds in GRB 070714B, and more noticeably the late-time giant flare in GRB 050724.

¹Corrected values for B and P were used; an error was discovered in the k-correction calculations that means the results in that paper work out too high by a factor of $(1+z)$ in Luminosity.

GRB	Γ	z	Ref.
050724	1.77	0.2576 ¹	Covino et al. (2005)
051227	1.46	2.8 ^{2a}	Barbier et al. (2005)
060614	1.79	0.1254 ³	Parsons et al. (2006)
061006	2.03	0.4377 ⁴	Schady et al. (2006)
061210	2.20	0.4095 ⁵	Cannizzo et al. (2006)
070714B	1.15	0.9224 ⁶	Racusin et al. (2007)
071227	1.54	0.381 ⁷	Sakamoto et al. (2007)
080123	1.99	(0.39)	Ukwatta et al. (2008)
111121A	1.50	(0.39)	D’Elia et al. (2011)

Table 3.2: Selected sample of EE GRBs. Bracketed values for redshift, z , indicate no published value was available. In these cases the mean value of the EE sample where z is known was used. ^aupper limit. ¹Prochaska et al. (2005); ²D’Avanzo et al. (2009); ³Price et al. (2006); ⁴Berger (2007); ⁵Cenko et al. (2006); ⁶Graham et al. (2009); ⁷D’Avanzo et al. (2007)

The results of the fitting process can be seen in Table 3.3 and Fig. 3.3. The light curves in Fig. 3.3 are a smoothed version of the original fit; once a fit was found, a plot was created using the resulting parameters running from 1 to 10^5 s to show the global trend. In this way, the predicted behaviour from the fit can be observed during gaps in the light curve data. All light curves and associated results represent the global minimum χ^2 value.

Fig. 3.4 shows the effect that varying the efficiency of the propeller has on the result for P , the parameter most directly responsible for the luminosity output. It shows that for most bursts, efficiencies less than 10% require a spin period more rapid than that of the break-up frequency for the magnetar. This can be compensated for somewhat by varying B , M_d and R_d and exploring other regions for parameter space, but the general message is clear: the conversion of kinetic energy to EM waves must be fairly efficient for magnetic propelling to be successful. Efficiencies of less than $\sim 10\%$ will not produce the required luminosity.

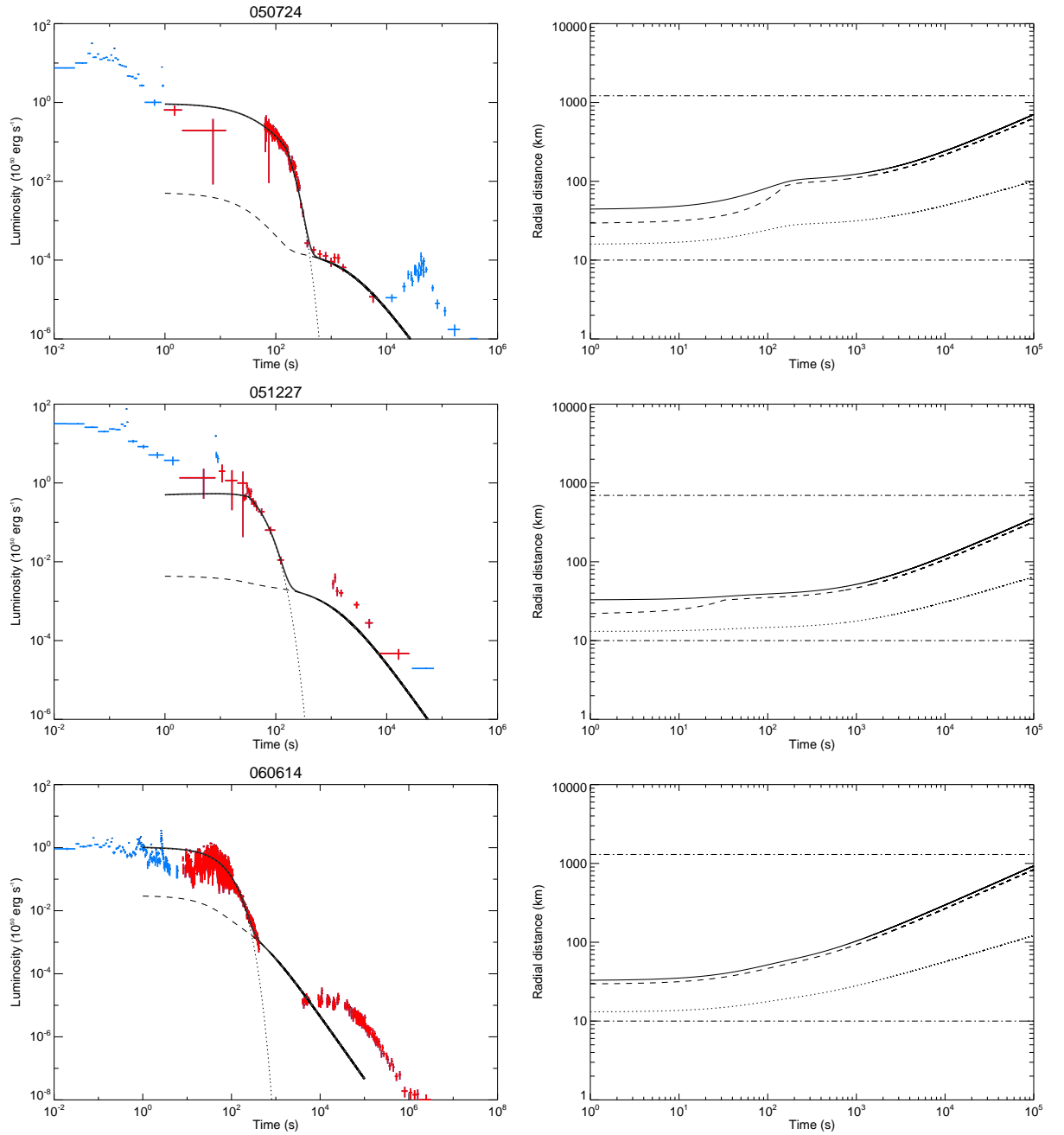


Figure 3.3a: Each row shows details for one burst. Left: black line - model fit, describing the summed contribution from the propeller (dotted line) and dipole (dashed line); red points - data that have been fitted to; blue points - data not fitted to. Right: dotted (dashed) line shows the position of the co-rotation (Alfvén) radius in km against time. Solid line marks the light cylinder radius. Lower dot-dashed line is the magnetar radius, upper dot-dashed line is the outer disc radius.

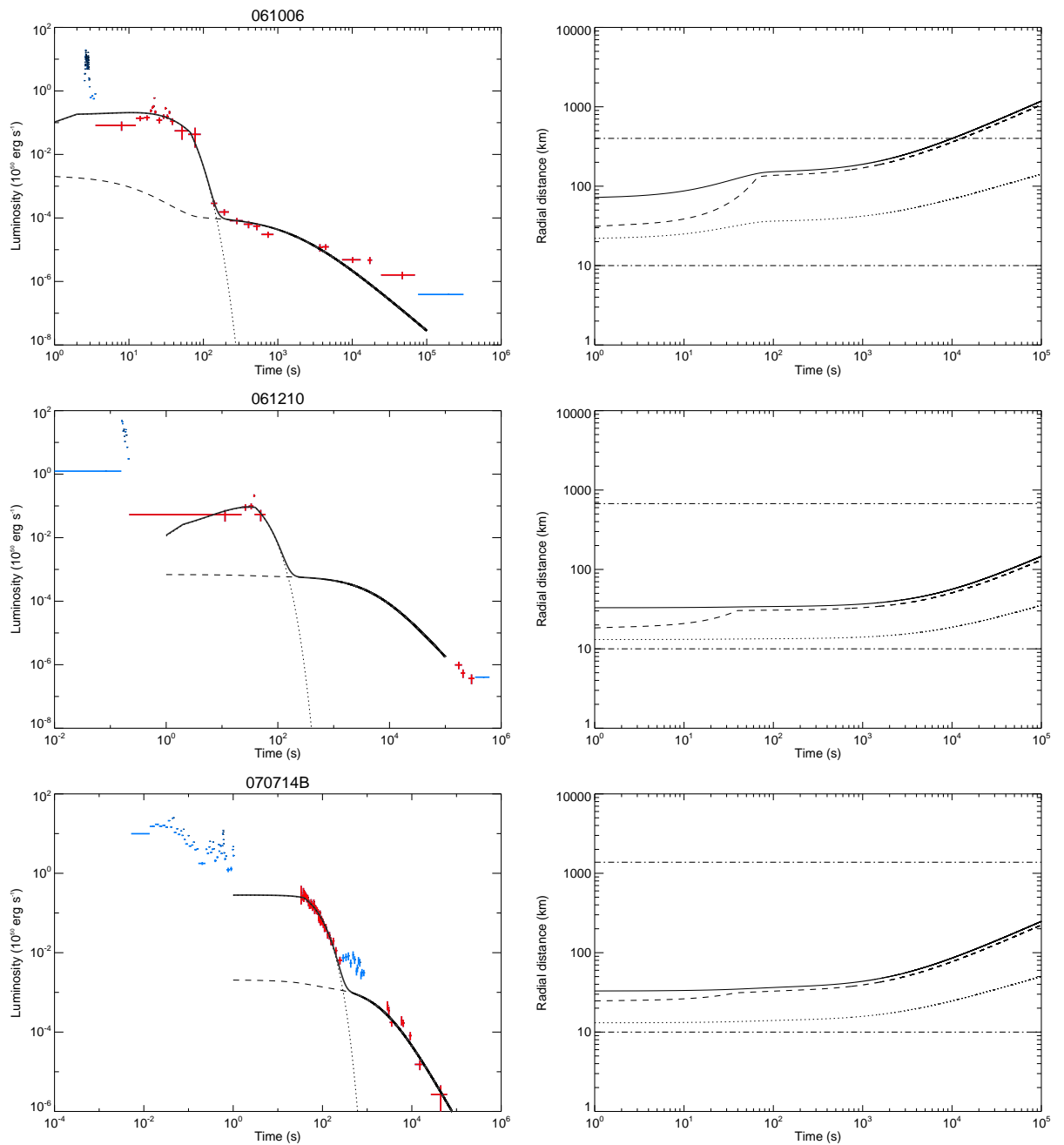


Figure 3.3b: Combined dipole and propeller fits to 061006, 061210 and 070714B.

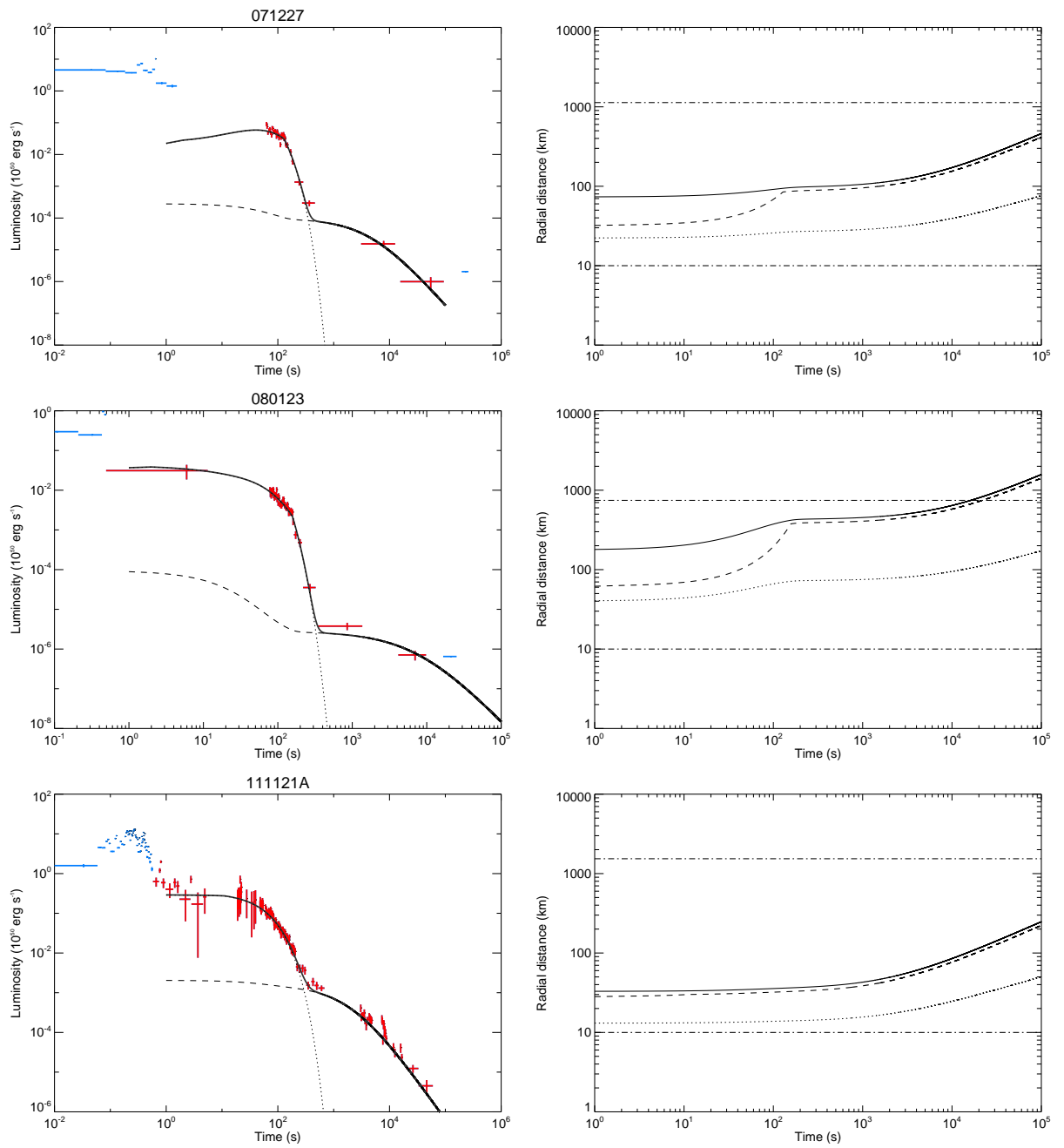


Figure 3.3c: Combined dipole and propeller fits to 071227, 080123 and 11121A.

GRB	P (ms)	B (10^{15} G)	M_d (M_\odot)	R_d (km)
050724	0.93 ± 0.04	0.88 ± 0.04	$(2.63 \pm 0.13) \times 10^{-2}$	1217 ± 4
051227	0.69 [L]	0.45 ± 0.19	$(1.10 \pm 0.18) \times 10^{-2}$	695 ± 41
060614	0.69 [L]	1.17 ± 0.05	$(1.20 \pm 0.01) \times 10^{-2}$	1300 ± 4
061006	1.51 ± 0.21	1.48 ± 0.07	$(2.01 \pm 0.37) \times 10^{-2}$	400 ± 2
061210	0.69 [L]	0.18 ± 0.05	$(3.20 \pm 2.88) \times 10^{-3}$	674 ± 753
070714B	0.69 [L]	0.31 ± 0.05	$(6.91 \pm 0.28) \times 10^{-3}$	1378 ± 72
071227	1.54 ± 0.12	0.57 ± 0.08	$(7.63 \pm 1.02) \times 10^{-3}$	1131 ± 17
080123	3.75 ± 0.46	1.92 ± 0.16	$(5.82 \pm 1.10) \times 10^{-3}$	742 ± 6
111121A	0.69 [L]	0.31 ± 0.03	$(4.80 \pm 0.10) \times 10^{-3}$	1538 ± 43

Table 3.3: Results from fitting the propeller model to nine EE GRBs, showing the best fit values for the spin period (P), dipole field strength (B), accretion disc mass (M_d), and the outer disc radius (R_d). Values with an [L] came up against the parameter limit for the minimum allowed spin period, and therefore do not have associated errors. Errors are 1σ .

3.5 Discussion

The derived accretion disc masses and radii are all broadly consistent with theoretical predictions (Lee et al., 2009), lying in the range of a few $10^{-3} M_\odot$ to a few $10^{-2} M_\odot$ and $\sim 400 - 1500$ km respectively. For only one burst, GRB 071227, is the initial spin period consistent with that in Gompertz et al. (2013). This is not surprising; the two studies were done with different efficiencies for the dipole (5% in this chapter vs 100% in Gompertz et al. 2013), and the rate of spin-down was enhanced by the inclusion of an accretion disc (Equation 3.30) which was not present in the previous work.

Most bursts in the sample show evidence of a smooth connection from the prompt to EE phase; however, GRB 060614 and GRB 061006 appear to struggle to capture the rising profile of propellerling at early times. This could be explained by the simplicity in the model used; the accretion disc was assumed to be present at $t = 0$ s, meaning accretion began immediately and at its peak strength. In reality, material would still be falling back at this time, so that accretion would initially be much gentler, but would grow in strength as the disc was fed. Lee et al. (2009) predict the material would return on a time-scale of ~ 10 s, which would help explain these features.

The model has some trouble fitting the extended tail and dipole plateau in GRB 060614 simultaneously. The problem is caused by the longer than normal plateau, which turns over at around 10^5 s rather than the $10^3 - 10^4$ s seen in the other bursts. Sustaining the plateau for this long requires a low value for B ($\sim 10^{14}$ G) or a long spin period (~ 10 ms), but the very luminous extended tail in this burst demands exactly the opposite. Fitting tends to favour the demands of the EE, since this is where more of the data points are found. The problem can be partially solved by varying the efficiency between the two components, since this has the effect of increasing or decreasing the power law slope that connects them, but for reasonable values of efficiency, a discrepancy still remains. One potential solution to this dilemma is the possibility that the magnetic field is not constant in this burst (or, probably more accurately, more varying than the other bursts). An order of magnitude decay in the magnetic field can extend the duration of the dipole plateau by more than an order of magnitude temporally, more than enough for the requirements of 060614, although how, and if any emission would be observable is unclear. The model can also be seen to be struggling under the luminosity demands of GRB 051227, but this is almost certainly due to it having been placed at its redshift upper limit of $z = 2.8$. Indeed, when a higher efficiency is used (analogous to a lower z), this burst is well described by the model.

According to Metzger et al. (2011) and Bucciantini et al. (2012), bursts with dipole fields $\gtrsim 10^{15}$ G will produce winds that are sufficiently clean to become optically thin at the jet energy dissipation radius on time-scales suitable for EE. The results for B find good agreement with this threshold, especially since the value for dipole efficiency is somewhat tentative at 5%, and could easily be increased, resulting in a further increase in B .

As can be seen in Fig. 3.3, most (if not all) burst light curves are type II. This is certainly the most likely of the four types identified in Section 3.3, as the template light curves returned a ‘classic’ type 37% of the time, but these synthetic curves suggest we should have roughly three type I, four type II and one each from types III and IV from the sample of nine (although these are small number statistics). From the best fit curves, GRB 061210 and GRB 071227 could be considered

candidates for the type I population, which just leaves an absence of ‘sloped’ and ‘stuttering’ bursts. The reason for this could well be that these classes are not readily identified as EE. As previously mentioned in Section 3.3.3, a type III ‘sloped’ burst could easily be identified as a LGRB or SGRB due to the single component look given to the light curve when propelling and dipole emission produce similar luminosities. Similarly, the type IV ‘stuttering’ bursts could be mistaken for a SGRB with a flare, or a LGRB with $T_{90} \approx 10$ s. These rarer classes could then simply be absent from the accepted EE population, whilst the type I and II bursts, which are indistinguishable when given the right prompt emission or data availability, constitute the entire EE category. This could have a knock-on effect in M_d ; the derived values for M_d are typically quite low (a few $10^{-3} M_{\odot}$), but the missing classes are those that typically exhibit the most massive discs, skewing the mean values towards the lower end. However, the predicted paucity of type III and IV propellers means that this effect may not be particularly large.

Whilst the results using the exponential accretion rate enjoy a reasonable degree of success, the two power law accretion rates appear rather less suited to the task. In all cases, the obtained best fits were of lesser quality than those found with an exponential decay, and the fits were frequently unable to model both emission components simultaneously, instead settling for the EE alone. In both power law cases, fitting the steep decays after the cessation of EE meant that the dipole emission was also forced to drop off rapidly, plummeting to a level far below that of the plateau in the data. There was no significant difference between the $t^{-4/3}$ and $t^{-5/3}$ profiles. From this, it seems that an exponential accretion rate may be required for magnetic propelling to be a viable mechanism in EE GRBs. Another key requirement for a successful propeller is that the conversion efficiency of kinetic energy to EM radiation for propellered material needs to be fairly high ($\gtrsim 10\%$). It is believed that the efficiency of the highly relativistic prompt emission can be $\gtrsim 50\%$ (Nousek et al., 2006), so an efficiency in the region of 10 – 40% is not entirely unreasonable for the slightly softer EE, but it is uncertain whether this level of efficiency could be maintained over the entire extended tail.

Fig. 3.5 shows where the results place these EE bursts relative to other GRBs, both short and long. Whilst they appear to populate their own region of low B-field and spin period, caution is required when drawing conclusions from this plot. Firstly, these results were obtained using efficiencies of 40% in the propeller and 5% in the dipole, whereas, for example, the short sample from Rowlinson et al. (2013) were examined using 100% efficient emission. Secondly, and probably more importantly, the rate of dipole spin-down is enhanced by the presence of the accretion disc in the current work, making a direct comparison with previous results difficult, since they did not have this enhanced rate. If the enhanced rate is not used, then the values found for B and P in EE bursts lie in the same region of parameter space as those for the SGRB sample. Even if their spin periods and dipole fields are not unique, the degree to which magnetic propelling influences the light curves offers a natural explanation for the difference between the two classes, since any propeller luminosity is predicated on the presence of an accretion disc; remove the disc and you're left with an ordinary SGRB. In fact, the disc does not need to be completely absent. If the disc mass is below around $10^{-6} M_{\odot}$ it becomes difficult to produce a propeller luminosity much above $10^{49} \text{ erg s}^{-1}$ as the accretion rate is too low. As a result, emission becomes dominated by the dipole contribution and light curves take on forms increasingly resembling SGRBs (e.g. Rowlinson et al., 2013).

Creating discs of different masses requires varying conditions in the progenitor system. Two potential factors during binary merger are the mass ratio and the equation of state. Hotokezaka et al. (2013) find the rest mass and kinetic energy of ejected material is greater with decreasing mass ratio (more asymmetric binaries) when the equation of state allows for more compact NSs. Rosswog (2007) also showed that binary systems with significantly unequal masses exhibit progressively more varied fallback behaviours with decreasing mass ratio. If material returns to the newly formed magnetar at earlier times and in greater quantities as described in Lee et al. (2009), then the conditions for propelling may be met. EE then, could be the product of an unequal mass binary merger, whilst SGRBs are born of more equal mass binaries. The comparative rarity of EE events may be attributed to the lesser abundance of more massive ($\gtrsim 1.4 M_{\odot}$) NSs (Valentim

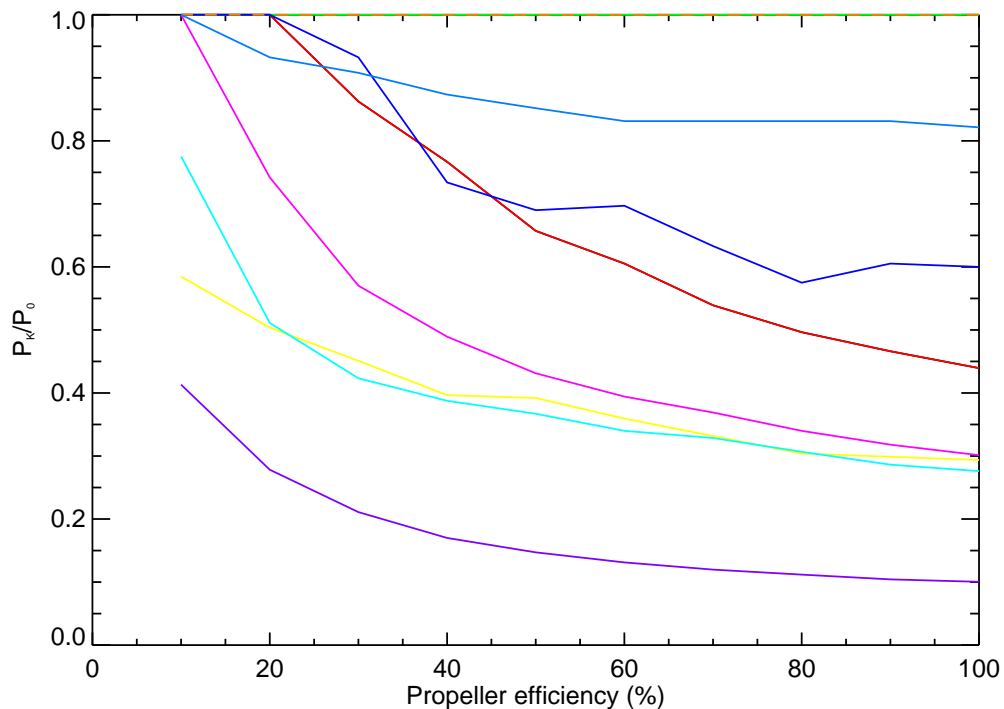


Figure 3.4: Spin break-up period (P_K) over initial spin period (P_0) versus propeller emission efficiency. A value of 1 on the y-axis indicates the burst is born with $P_0 = P_K$, with decreasing fractions representing increasingly higher initial spin periods. Dipole efficiency is 10% throughout. Red - 050724; Green - 051227; Blue - 060614; Yellow - 061006; Magenta - 061210; Orange - 070714B; Cyan - 071227; Light green - 080123; Violet - 111121A.

et al., 2011; Lattimer, 2012) and hence fewer unequal mass NS binaries.

3.5.1 Radio emission

The radio afterglow is one of the main proving grounds for the magnetar model. The presence (or lack) of radio emission on time-scales of a few months to years after a burst is detected will place firm limits on the circum-burst medium (CBM), or, in cases where the local density is already known, the magnetar model. Recently Metzger & Bower (2014) claim to have ruled out long-lived millisecond magnetars as the central engine for two bursts: GRB 060505 and GRB 050724, the latter of which features in this study. The authors found that a few 10^{52} erg ejected at $\beta_0 \sim 1$

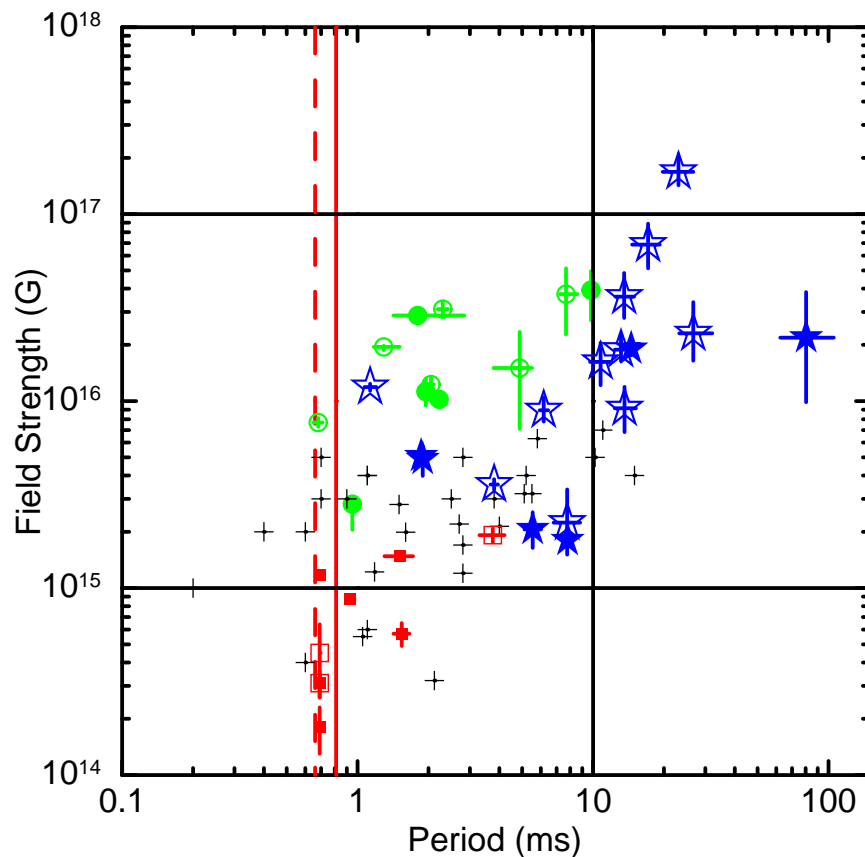


Figure 3.5: A plot of magnetic field strength versus spin period. The solid (dashed) red line represents the spin break-up period for a collapsar (binary merger) progenitor (Lattimer & Prakash, 2004). Blue stars: stable magnetars and green circles: unstable magnetars which collapse to form a BH (Rowlinson et al., 2013). Black ‘+’ symbols are the LGRB candidates identified by Lyons et al. (2010); Dall’Osso et al. (2011); Bernardini et al. (2012). The red squares are the magnetic fields and spin periods of the present work. Filled symbols have observed redshifts, open symbols use the sample average redshift, which is $z = 0.39$ for EE bursts and $z = 0.72$ for the SGRBs from Rowlinson et al. (2013).

should have been detectable during their observation ~ 2.5 years after the burst for $\epsilon_B = 0.1$, unless the CBM is 0.05 cm^{-3} or less. Panaitescu (2006) have independently constrained the CBM around GRB 050724 to be $0.1 < n < 10^3 \text{ cm}^{-3}$; however, Berger et al. (2005) find it to be consistent with values as low as $n \approx 0.02 \text{ cm}^{-3}$, with a best fit value $n \approx 0.1 \text{ cm}^{-3}$. The lack of detection could be explained if the value of n lies at the lower end of this range. For higher densities ($n \gtrsim 0.05 \text{ cm}^{-3}$) the lack of observation could be explained by a lower value of ϵ_B . GRB 050724 is not typical even amongst the oddball sample of EE bursts, since it has the longest and one of the most luminous EE tails observed. In addition, it is unique in the class in having an as

yet unexplained giant flare seen in the X-ray light curve at \sim a few 10^4 s after trigger.

For EE, ejecting the majority of a $10^{-3} M_{\odot}$ fallback disc at initial velocities of up to $0.9c$ could produce a distinct feature in the radio signature of the GRB. The details of this signature are saved for future study, but constraints on the model placed by previous radio band observations of EE bursts are discussed. Of the nine EE GRBs in this sample, only GRB 050724 has a detection in radio emission, with three more (051227, 061210 and 070714B) having upper limits (Chandra & Frail, 2012). All observations were taken using the VLA. Using the equations in Nakar & Piran (2011) (and supplementary information), the peak synchrotron frequency in the radio band is found to be more than an order of magnitude redder than the 8.46 GHz observing frequency of the VLA. The peak flux in the detector bandpass is also found to be at least an order of magnitude lower than the afterglow detection in GRB 050724 (Berger et al., 2005), which was made during the late-time giant X-ray flare seen in the light curve at around $10^4 - 10^5$ s. The detected radio emission was fairly typical of SGRB radio afterglows, and therefore may well have been the radio signature of the prompt emission, rather than that of the EE tail. The peak flux in the detector bandpass was also at least an order of magnitude lower than the upper limits for GRB 051227 (Frail, 2005a), GRB 061210 (Chandra & Frail, 2006) and GRB 070714B (Chandra & Frail, 2007). Radio observations of GRB afterglows may therefore not currently be constraining for EE if the underlying mechanism is a magnetic propeller, but are now at a level where they are becoming highly constraining to a millisecond pulsar (magnetar) central engine, and will become more so with the upgraded VLA (Perley et al., 2011).

A major caveat to an EE-driven radio signature is the relative Lorentz factors involved in the prompt emission and EE tail. A maximum ejection velocity of $0.9c$ corresponds to a Lorentz factor of just 2.29, whereas the prompt emission is believed to have an initial Lorentz factor in the region of 100 – 1000 (Lithwick & Sari, 2001; Zou & Piran, 2010; Zou et al., 2011; Ghirlanda et al., 2012; Lü et al., 2012). There is therefore significant doubt that the EE ejecta can catch up to the forward shock driven by the prompt ejecta. For an adiabatic expansion, the bulk Lorentz factor of the blast

wave evolves as $\Gamma \propto t^{-3/8}$ ($t^{-1/4}$) in a homogeneous (wind) medium, or $\Gamma \propto t^{-3/7}$ ($t^{-1/3}$) in the radiative case (van der Horst, 2007), where a homogeneous medium is one with a density profile that scales as r^0 , and a wind medium as r^2 . The time taken for the prompt-driven blast wave to decelerate to $0.9c$ is at least 0.08 d, where $\Gamma_0 = 100$ with radiative expansion into a homogeneous medium, and could be up to 1156 y if $\Gamma = 1000$ and the expansion proceeds adiabatically into a wind medium. In both cases, the effects of energy injection have been neglected, meaning that the deceleration is even less rapid within the framework of the magnetar model. Meanwhile, the propeller driven shell has itself decelerated, and although will likely encounter a more rarified CBM and therefore decelerate more slowly, the aforementioned thresholds only represent the time at which it will stop losing ground on the forward shock, even neglecting its own deceleration.

For the purpose of the present chapter, the inability of the propeller ejecta to catch up to the forward shock is not important, since the suggested X-ray emission site is internal, and likely to do with collisions between discrete shells of propeller-driven ejecta. The evidence for this comes from the temporal decay indices at the end of the EE plateaux, which can be as steep as t^{-8} (Gompertz et al., 2013), completely inconsistent with forward shock emission (e.g. Sari et al., 1998; Wijers & Galama, 1999). Nonetheless, it provides a strong argument against an EE contribution to the GRB afterglow.

3.6 Conclusions

Using magnetic propelling and dipole spin-down, the first simultaneous fits to both the extended tail and the afterglow plateau were obtained for a sample of nine EE GRBs. The results show typical disc masses of a few $10^{-3} M_{\odot}$ to a few $10^{-2} M_{\odot}$, spin periods of a few ms, and magnetic fields of around 10^{15} G. The ability to reconcile two emission features within a single central engine suggests there may be some weight to the idea that a highly magnetised NS is responsible for these phenomena. Whilst it is possible that the values for magnetic field and spin period

are different in EE GRBs and SGRBs, it is hard to argue conclusively that this is the case. It may be that the difference could also be due to subtleties in the progenitor, specifically the mass ratio, where unequal mass binaries produce the fallback material required to power magnetic propelling, whilst more equal mass binaries do not. Radio observations of EE GRBs are now at a level close to where magnetar spin-down can be ruled out, but do not appear to be constraining to the EE tail if the underlying mechanism is indeed a magnetic propeller. The major constraint currently is the requirement that the conversion of kinetic energy to EM radiation in accelerated material be at least $\gtrsim 10\%$.

4

Broad-band modelling of short gamma-ray bursts with energy injection from magnetar spin-down and its implications for radio detectability

This chapter presents the work originally published in Gompertz et al. (2015).

Abstract

The magnetar model has been proposed to explain the apparent energy injection in the X-ray light curves of short gamma-ray bursts (SGRBs), but its implications across the full broadband spectrum are not well explored. Here, the broadband modelling of four SGRBs with evidence for energy injection in their X-ray light curves is investigated by applying a physically motivated model in which a newly formed magnetar injects energy into a forward shock as it loses angular momentum along open field lines. By performing an order of magnitude search for the underlying physical parameters in the blast wave, the characteristic break frequencies of the synchrotron spectrum are constrained against their manifestations in the available multi-wavelength observations for each burst. The application of the magnetar energy injection profile restricts the successful matches to a limited family of models that are self-consistent within the magnetic dipole spin-down framework. Synthetic light curves are produced that describe how the radio signatures of these SGRBs ought to have looked given the restrictions imposed by the available data, and the detectability of these signatures with present-day and near-future radio telescopes is discussed. The results show that both the Atacama Large Millimetre Array and the upgraded Very Large Array are now sensitive enough to detect the radio signature within two weeks of trigger in most SGRBs, assuming the sample is representative of the population as a whole. It is also found that the upcoming Square Kilometre Array will be sensitive to depths greater than those of the lower limit predictions.

4.1 Introduction

This chapter expands the discussion of the magnetar model to the broadband view. The application of the dipole and propeller models seen in the previous chapters focused on the X-ray emission of EE GRBs. Typically in these analyses, the energy released by the dipole spin-down and magnetic propeller mechanisms is assumed to be injected into the forward shock, where it is reprocessed and re-emitted with a particular transition efficiency. This is a useful first-order assumption for probing the compatibility of the models with the observed X-ray emission, but reveals no information on the spectral properties, and hence the broadband signature, of the sources. However, some work on extending the spectrum to optical frequencies has been attempted (Rowlinson et al., 2013).

In this chapter, broadband modelling of SGRB and EE GRB light curves is attempted, with the dipole spin-down (and magnetic propeller where applicable) profile used as the specific energy injection term. In this way, the compatibility of the magnetar energy injection scenario with observations from across the entire electromagnetic spectrum can be tested. With the spectrum constrained, predictions can be made for how this signature ought to have looked at any frequency, and this is also discussed in the context of present day and near-future radio telescopes.

Although some mention of synchrotron physics was made in the original work (see Section 4.3.1), the physics behind the forward shock merits a more detailed introduction, and this is given here in a discussion based on Chapter 2 of van der Horst (2007). This introduction provides an opportunity to specifically state the equations that went into the computational model used in the analysis, which was not convenient in the published paper.

4.1.1 The synchrotron spectrum

It is assumed that the blast wave accelerates electrons to a power-law distribution of Lorentz factors γ_e , with a power-law index p and a minimum Lorentz factor of γ_m , i.e. $N(\gamma_e)d\gamma_e \propto \gamma_e^{-p}d\gamma_e$, with $\gamma_e \geq \gamma_m$. The spectral power an observer receives from a single electron can be approximated by (cf. Kaplan & Tsytovich, 1973)

$$P_x(x) = 3 \left(\frac{3}{2} \right)^{\frac{1}{3}} \frac{q_e^3 B_s \Gamma}{m_e c^2} x^{\frac{1}{3}} e^{-x}, \quad (4.1)$$

where q_e (m_e) is the electron charge (mass) in statC (g), B_s is the magnetic field strength of the shock, Γ is the Lorentz factor of the shocked medium (in the frame of the un-shocked medium), and $x = \frac{\nu}{\nu_e}$. ν is the observing frequency and $\nu_e = \Gamma \gamma_e^2 q_e B_s / (2\pi m_e c)$ is the characteristic synchrotron frequency. The total power emitted is then just the integral of equation 4.1 over the full distribution of γ_e .

The electron distribution function $N(\gamma_e)$ is not actually a single power-law because the electrons lose energy by emitting radiation. Those with the highest Lorentz factors emit the fastest, and the electron distribution function therefore steepens at the cooling Lorentz factor γ_c , where the synchrotron cooling timescale is equal to the lifetime of the source. Electrons with $\gamma_e > \gamma_c$ cool on timescales less than the lifetime of the source, and their distribution function becomes $N(\gamma_e)d\gamma_e \propto \gamma_e^{-p-1}d\gamma_e$ when $\gamma_c < \gamma_m < \gamma_e$, or $N(\gamma_e)d\gamma_e \propto \gamma_e^{-2}d\gamma_e$ when $\gamma_c < \gamma_e < \gamma_m$. In the case where $\gamma_m > \gamma_c$, all the electrons have a Lorentz factor of $\gamma_e > \gamma_c$, and so all cool rapidly; a condition known as the fast cooling regime. In the case of $\gamma_m < \gamma_c$, a fraction of electrons will have $\gamma_e > \gamma_c$, with the rest having $\gamma_e < \gamma_c$. The cooling effect and the form of the distribution function means that the latter fraction will be larger. This is the slow cooling regime.

By integrating $N(\gamma_e)$ over γ_e and demanding that the distribution function be continuous at the spectral breaks (i.e. at γ_c or γ_m for slow and fast cooling respectively), the distribution function

can be expressed in four regions:

$$N(\gamma_e)d\gamma_e = n_e(p-1) \left(1 - \frac{1}{p} \left(\frac{\gamma_c}{\gamma_m}\right)^{-(p-1)}\right)^{-1} \left(\frac{\gamma_e}{\gamma_m}\right)^{-p} d\left(\frac{\gamma_e}{\gamma_m}\right) \quad (4.2)$$

if $\gamma_m < \gamma_e < \gamma_c$,

$$N(\gamma_e)d\gamma_e = n_e(p-1) \left(1 - \frac{1}{p} \left(\frac{\gamma_c}{\gamma_m}\right)^{-(p-1)}\right)^{-1} \left(\frac{\gamma_c}{\gamma_m}\right)^{-(p-1)} \left(\frac{\gamma_e}{\gamma_c}\right)^{-p-1} d\left(\frac{\gamma_e}{\gamma_c}\right) \quad (4.3)$$

if $\gamma_m < \gamma_c < \gamma_e$,

$$N(\gamma_e)d\gamma_e = n_e \left(1 - \frac{p-1}{p} \left(\frac{\gamma_m}{\gamma_c}\right)^{-1}\right)^{-1} \left(\frac{\gamma_e}{\gamma_c}\right)^{-2} d\left(\frac{\gamma_e}{\gamma_c}\right) \quad (4.4)$$

if $\gamma_c < \gamma_e < \gamma_m$, and

$$N(\gamma_e)d\gamma_e = n_e \left(1 - \frac{p-1}{p} \left(\frac{\gamma_m}{\gamma_c}\right)^{-1}\right)^{-1} \left(\frac{\gamma_m}{\gamma_c}\right)^{-1} \left(\frac{\gamma_e}{\gamma_m}\right)^{-p-1} d\left(\frac{\gamma_e}{\gamma_m}\right) \quad (4.5)$$

if $\gamma_c < \gamma_m < \gamma_e$. The first two cases are the slow cooling regime, and the latter two represent fast cooling. n_e is the total electron number density. The total power can then be calculated. For the slow cooling case

$$\begin{aligned} P_\nu = & 3 \left(\frac{3}{2}\right)^{\frac{1}{3}} \frac{n_e q_e^3 B \Gamma(p-1)}{m_e c^2} \left(1 - \frac{1}{p} \left(\frac{\nu_c}{\nu_m}\right)^{-\frac{p-1}{2}}\right)^{-1} \\ & \cdot \left\{ \left(\frac{\nu}{\nu_m}\right)^{-\frac{p-1}{2}} \left[\Gamma_f\left(\frac{p}{2} - \frac{1}{6}, \frac{\nu}{\nu_c}\right) - \Gamma_f\left(\frac{p}{2} - \frac{1}{6}, \frac{\nu}{\nu_m}\right) \right] \right. \\ & \left. + \left(\frac{\nu_c}{\nu_m}\right)^{-\frac{p-1}{2}} \left(\frac{\nu}{\nu_c}\right)^{-\frac{p}{2}} \left[\Gamma_f\left(\frac{p}{2} + \frac{1}{3}\right) - \Gamma_f\left(\frac{p}{2} + \frac{1}{3}, \frac{\nu}{\nu_c}\right) \right] \right\}, \quad (4.6) \end{aligned}$$

and for fast cooling

$$\begin{aligned}
P_\nu = & 3 \left(\frac{3}{2} \right)^{\frac{1}{3}} \frac{n_e q_e^3 B \Gamma}{m_e c^2} \frac{1}{2} \left(1 - \frac{p-1}{p} \left(\frac{\nu_m}{\nu_c} \right)^{-\frac{1}{2}} \right)^{-1} \\
& \cdot \left\{ \left(\frac{\nu}{\nu_c} \right)^{-\frac{1}{2}} \left[\Gamma_f \left(\frac{5}{6}, \frac{\nu}{\nu_m} \right) - \Gamma_f \left(\frac{5}{6}, \frac{\nu}{\nu_c} \right) \right] \right. \\
& \left. + \left(\frac{\nu_m}{\nu_c} \right)^{-\frac{1}{2}} \left(\frac{\nu}{\nu_m} \right)^{-\frac{p}{2}} \left[\Gamma_f \left(\frac{p}{2} + \frac{1}{3} \right) - \Gamma_f \left(\frac{p}{2} + \frac{1}{3}, \frac{\nu}{\nu_m} \right) \right] \right\}. \tag{4.7}
\end{aligned}$$

Both of these expressions use the incomplete Gamma function $\Gamma_f(y, a)$, which takes the form

$$\Gamma_f(y, a) = \int_a^\infty \frac{x^y e^{-x}}{x} dx. \tag{4.8}$$

This emission is also subject to synchrotron self-absorption, which comes into play in optically thick media where the optical depth $\tau_\nu \geq 1$. The absorption coefficient, upon which the optical depth depends, is given in the slow cooling case by

$$\begin{aligned}
\alpha_\nu = & 3 \left(\frac{3}{2} \right)^{\frac{1}{3}} \frac{n_e q_e^3 B \Gamma}{8\pi m_e^2 c^2 \gamma_m \nu^2} \frac{p-1}{2} \left(1 - \frac{1}{p} \left(\frac{\nu_c}{\nu_m} \right)^{-\frac{p-1}{2}} \right)^{-1} \\
& \cdot \left\{ (p+2) \left(\frac{\nu}{\nu_m} \right)^{-\frac{p}{2}} \left[\Gamma_f \left(\frac{p}{2} + \frac{1}{3}, \frac{\nu}{\nu_c} \right) - \Gamma_f \left(\frac{p}{2} + \frac{1}{3}, \frac{\nu}{\nu_m} \right) \right] \right. \\
& \left. + (p+3) \left(\frac{\nu_c}{\nu_m} \right)^{-\frac{p}{2}} \left(\frac{\nu}{\nu_c} \right)^{-\frac{p+1}{2}} \left[\Gamma_f \left(\frac{p}{2} + \frac{5}{6} \right) - \Gamma_f \left(\frac{p}{2} + \frac{5}{6}, \frac{\nu}{\nu_c} \right) \right] \right\}, \tag{4.9}
\end{aligned}$$

and in the fast cooling case by

$$\begin{aligned}
\alpha_\nu = & 3 \left(\frac{3}{2} \right)^{\frac{1}{3}} \frac{n_e q_e^3 B \Gamma}{8\pi m_e^2 c^2 \gamma_c \nu^2} \frac{1}{2} \left(1 - \frac{p-1}{p} \left(\frac{\nu_m}{\nu_c} \right)^{-\frac{1}{2}} \right)^{-1} \\
& \cdot \left\{ 4 \left(\frac{\nu}{\nu_c} \right)^{-1} \left[\Gamma_f \left(\frac{4}{3}, \frac{\nu}{\nu_m} \right) - \Gamma_f \left(\frac{4}{3}, \frac{\nu}{\nu_c} \right) \right] \right. \\
& \left. + (p+3) \left(\frac{\nu_m}{\nu_c} \right)^{-1} \left(\frac{\nu}{\nu_m} \right)^{-\frac{p+1}{2}} \left[\Gamma_f \left(\frac{p}{2} + \frac{5}{6} \right) - \Gamma_f \left(\frac{p}{2} + \frac{5}{6}, \frac{\nu}{\nu_m} \right) \right] \right\}. \tag{4.10}
\end{aligned}$$

The transition from optically thin to optically thick happens as the self-absorption frequency, ν_a . The flux across the whole range of τ_ν can be written as

$$F_\nu = \frac{R^3 P_\nu}{3D_L^2} \left(\frac{\alpha_\nu}{\alpha_{\nu_a}} \right)^{-1} \left[1 - \exp\left(- \frac{\alpha_\nu}{\alpha_{\nu_a}} \right) \right], \quad (4.11)$$

where R is the radial extent of the blast wave, D_L is the luminosity distance to the source (both in cm) and α_{ν_a} is the absorption coefficient α_ν at the self-absorption frequency ν_a . This implies that $F_\nu \propto \nu^2$ in both slow and fast cooling regimes for $\nu < \nu_a < \nu_m$, and is proportional to $\nu^{5/2}$ when $\nu_m < \nu < \nu_a$.

4.1.2 Spectral break evolution

The evolution of the light curves at various frequencies is a product of the movement of the spectral breaks, which themselves are subject to the hydrodynamical evolution of the fireball. The exact reasons and derivation of this evolution's dependence on the underlying physical parameters of the system is complicated, and beyond the scope of this thesis. For more information, see Blandford & McKee (1976); Sari et al. (1998); Wijers & Galama (1999); van der Horst (2007); Gao et al. (2013b); van Eerten (2014).

The work in this chapter examines a relativistic shock moving adiabatically into a homogeneous medium (cf. van der Horst, 2007). The maximum flux density of the spectrum is

$$F_{\nu,\max} = 21.3 \epsilon_{B,-1}^{\frac{1}{2}} n_0^{\frac{1}{2}} E_{52} d_{L,28}^{-2} \left(\frac{1+z}{2} \right) \text{ mJy}, \quad (4.12)$$

where $\epsilon_{B,-1}$ is the fraction of the energy contained in the magnetic field, in units of 10^{-1} , n_0 is the number density of the CBM (cm^{-3}), E_{52} is the energy in the blast wave in units of 10^{52} erg, and $d_{L,28}$ is the luminosity distance in units of 10^{28} cm.

The position of the cooling break is given by

$$\nu_c = 5.98 \times 10^{13} \epsilon_{B,-1}^{-\frac{3}{2}} n_0^{-1} E_{52}^{-\frac{1}{2}} t_d^{-\frac{1}{2}} \left(\frac{1+z}{2} \right)^{-\frac{1}{2}} \text{ Hz}, \quad (4.13)$$

where t_d is the time after GRB trigger in days. For the peak frequency,

$$\nu_m = 3.21 \times 10^{13} (p-2)^2 (p-1)^{-2} \epsilon_{e,-1}^2 \epsilon_{B,-1}^{\frac{1}{2}} E_{52}^{\frac{1}{2}} t_d^{-\frac{3}{2}} \left(\frac{1+z}{2} \right)^{\frac{1}{2}} \text{ Hz}, \quad (4.14)$$

where $\epsilon_{e,-1}$ is the fraction of energy contained in the emitting electrons (rather than the population of electrons as a whole) in units of 10^{-1} .

The self-absorption frequency depends on both ν_c and ν_m , and evolves differently depending on which is greatest, as well as whether it lies above or below the peak frequency. It evolves as

$$\nu_a = 9.21 \times 10^9 (p-2)^{-1} (p-1)^{\frac{8}{5}} \left(p + \frac{2}{3} \right)^{-\frac{3}{5}} (p+2)^{\frac{3}{5}} \epsilon_{e,-1} \epsilon_{B,-1}^{\frac{1}{5}} n_0^{\frac{3}{5}} E^{\frac{1}{5}} \left(\frac{1+z}{2} \right)^{-1} \text{ Hz} \quad (4.15)$$

for ($\nu_a < \nu_m < \nu_c$) and

$$\begin{aligned} \nu_a = & 2^{\frac{9p-22}{6(p+4)}} 3^{\frac{8}{3(p+4)}} \alpha_{\text{ad}}^{-\frac{p+2}{2(p+4)}} \beta_{\text{ad}}^{-\frac{3p+2}{2(p+4)}} \pi^{-\frac{p+2}{p+4}} \left(\frac{1+X}{2} \right)^{-\frac{2(p+2)}{p+4}} \left[\Gamma_f \left(\frac{p}{2} + \frac{1}{3} \right) \right]^{\frac{2}{p+4}} \\ & \cdot (p-2)^{\frac{2(p-1)}{p+4}} (p-1)^{-\frac{2(p-2)}{p+4}} (p+2)^{\frac{2}{p+4}} q_e^{\frac{p+6}{p+4}} m_e^{-\frac{3p+2}{p+4}} m_p^{\frac{2(p-1)}{p+4}} c^{-\frac{5p+10}{2(p+4)}} \epsilon_e^{\frac{2(p-1)}{p+4}} \\ & \cdot \epsilon_B^{\frac{p+2}{2(p+4)}} n_0^{\frac{2}{p+4}} E^{\frac{p+2}{2(p+4)}} t^{-\frac{3p+2}{2(p+4)}} (1+z)^{\frac{p-6}{2(p+4)}} \text{ Hz} \end{aligned} \quad (4.16)$$

for ($\nu_m < \nu_a < \nu_c$), both in the slow cooling regime. Note the change in units (in part due to the complication in simplifying terms with a variable exponent, p), so that ϵ_e and ϵ_B are whole units, and t is in seconds. α_{ad} and β_{ad} are adiabatic constants, the former relating the Lorentz factor (Γ) to the radius (R), and the latter accounting for the angular dependence between R and t . Their values are $\frac{16}{17}$ and 4, respectively (van der Horst, 2007). X is the mass fraction of hydrogen in the shock, and is set to 0.7. m_p is the proton mass (g).

	Relativistic	Jet break	Non-relativistic
$F_{\nu, \max}$	0	-1	3/5
ν_c	-1/2	0	-1/5
ν_m	-3/2	-2	-3
ν_a ($\nu_a < \nu_m < \nu_c$)	0	-1/5	6/5
ν_a ($\nu_m < \nu_a < \nu_c$)	$-\frac{3p+2}{2(p+4)}$	$-\frac{2(p+1)}{p+4}$	$-\frac{3p-2}{p+4}$
ν_a ($\nu_a < \nu_c < \nu_m$)	-1/2	-6/5	-1/5

Table 4.1: Time dependences of $F_{\nu, \max}$, ν_c , ν_m , and ν_a in the three phases of the blast wave's hydrodynamical evolution for adiabatic expansion into a homogeneous external medium.

For the fast cooling regime, ($\nu_a < \nu_c < \nu_m$),

$$\nu_a = 1.25 \times 10^9 \epsilon_{B,-1}^{\frac{6}{5}} n_0^{\frac{11}{10}} E_{52}^{\frac{7}{10}} t_d^{-\frac{1}{2}} \left(\frac{1+z}{2} \right)^{-\frac{1}{2}} \text{ Hz.} \quad (4.17)$$

The time dependence of the breaks and peak flux also changes with the different hydrodynamical states of the blast wave, which can be relativistic, post-jet break, and non-relativistic (see Section 4.3.1). The dependences for a shock expanding adiabatically into a homogenous medium are shown in Table 4.1.

4.2 Data Sample

The collected sample consists of four SGRBs with good X-ray observations exhibiting a clear plateau, and for which there were contemporaneous optical observations in at least one filter, as well as an identified redshift. Radio observations were not essential, but were a welcome bonus. The sample represents those SGRBs with the best data availability to test the analysis and introduce the model, but is not an exhaustive list of all SGRBs that satisfy the selection criteria. The classification of GRB 060614 is uncertain (Gehrels et al., 2006), but was included as an EE GRB here due to the lack of an associated supernova to deep limits (Della Valle et al., 2006; Gal-Yam et al., 2006) as would be expected for an LGRB. Analysis by Zhang et al. (2007) also

suggests that this burst is linked to the short class. The X-ray data used here were taken by the *Swift* X-Ray Telescope (XRT; Burrows et al. 2005) and were downloaded from the UK *Swift* Science Data Centre (UKSSDC) archives (Evans et al., 2007, 2009). The 0.3 – 10 keV flux light curves were used, corrected for absorption using a ratio of (counts-to-flux un-absorbed)/(counts-to-flux observed). Details of the data reduction process can be found in Evans et al. (2007, 2009). The 0.3 – 10 keV flux light curves were then compressed into flux density light curves at 1.73 keV (the bandpass logarithmic mid-point) using the equations in Appendix 4.8.

References for the ultraviolet (UV), optical, infrared (IR), and radio data that were used are shown in Table 4.2. Galactic extinction correction was done using the values in Schlafly & Finkbeiner (2011), even in cases where the original data were corrected using the Schlegel et al. (1998) values. In most cases, the effect of intrinsic absorption was neglected due to a lack of high-quality near-IR to optical data with which to constrain it. The single exception is GRB 130603B, which was corrected with $A_v = 0.86 \pm 0.15$ mag and a Small Magellanic Cloud (SMC) extinction law (de Ugarte Postigo et al., 2014). Conflicting values were also derived for the intrinsic absorption in GRB 060614, with Della Valle et al. (2006) finding $A_v = 0.08$ mag and Covino et al. (2013) finding $A_v = 0.74^{+0.20}_{-0.17}$ mag or $A_v = 0.62 \pm 0.06$ mag, depending on whether an X-ray prior was used. Both studies find an SMC extinction law. The discrepancy comes from the use of a spectral break between the optical and X-ray frequencies, and highlights how the applied model can influence the derived intrinsic absorption. Intrinsic absorption was neglected in this case in an attempt to make the results as general as possible. Fong (2014) derived $A_v = 0.5$ for GRB 070714B, but it was not included here because it was derived by comparison of the optical and X-ray bands, and is therefore dependent on the presence of a spectral break between them.

GRB	Γ	z	$E(B - V)$	Reference
051221A	$1.95^{+0.18}_{-0.17}$	0.5465^a	0.069	[1]
060614	$1.78^{+0.08}_{-0.08}$	0.1254^b	0.019	[2,3,4]
070714B	$1.76^{+0.28}_{-0.24}$	0.9224^c	0.141	[5] (A,B,C,D)
130603B	$1.98^{+0.15}_{-0.14}$	0.356^d	0.02	[6,7,8] (E)

Table 4.2: UV, optical, IR and radio data used. Photon indices, Γ are for the X-ray data, and come from the UKSSDC spectrum repository (Evans et al., 2007, 2009) which gives 90 per cent confidence interval errors. $E(B - V)$ values are from Schlafly & Finkbeiner (2011).

References (redshift): ^aSoderberg et al. (2006); ^bGal-Yam et al. (2006); ^cGraham et al. (2009); ^dThone et al. (2013).

References (refereed): [1] - Soderberg et al. (2006); [2] - Della Valle et al. (2006); [3] - Gal-Yam et al. (2006); [4] - Mangano et al. (2007); [5] - Graham et al. (2009); [6] - Tanvir et al. (2013); [7] - de Ugarte Postigo et al. (2014); [8] - Fong et al. (2014).

References (GCN circulars): (A) - Chandra & Frail (2007); (B) - Landsman et al. (2007); (C) - Perley et al. (2007); (D) - Weaver et al. (2007); (E) - de Pasquale & Melandri (2013).

4.3 Model

The central engine in the model is a magnetar, formed as a product of the merger of two NS. The merger drives a relativistic outflow, which expands with time. Internal processes such as shocks between expanding shells of ejecta (Goodman, 1986; Paczynski, 1986) or magnetic turbulence (Zhang & Yan, 2011) convert some of the kinetic energy of the blast wave into electromagnetic radiation, which is observed as the SGRB prompt emission. The blast wave sweeps up ambient particles as it expands into the circum-burst medium (CBM), and eventually starts to slow down once it has accumulated sufficient mass. This deceleration radius, R_{dec} , marks the outer boundary for emission processes to be considered ‘internal’. The interaction between the blast wave and the CBM forms a strong shock at the head of the ejecta, and a synchrotron emission spectrum is set up by the action of electrons traversing the shock front. This is the emission site of the afterglow. For simplicity, an adiabatic expansion is assumed, along with a homogeneous ambient medium, as is expected in the vicinity of an NS binary. However, for LGRBs or binaries with pulsar winds the local density profile can be different (see e.g. Starling et al., 2008; Curran et al., 2009).

4.3.1 Synchrotron emission

The relativistic blast wave accelerates electrons, which subsequently radiate synchrotron emission in accordance with their respective Lorentz factors, which are assumed to have a power-law distribution. There are two distinct emission regimes, dubbed ‘fast cooling’, in which the cooling time-scale of the electrons is less than the lifetime of the source, and ‘slow cooling’, in which the majority of electrons cool on longer timescales than the source lifetime. (Sari et al., 1998; Wijers & Galama, 1999).

The synchrotron spectrum has three characteristic break frequencies: the peak frequency, ν_m ; the cooling frequency, ν_c ; and the self-absorption frequency, ν_a , at which the medium changes from being optically thin to being optically thick. These breaks are not static in time, but change and evolve with the hydrodynamical expansion of the blast wave. Their position and evolution determines the phenomenology of the corresponding light curve at a given observational band (Sari et al., 1998; Wijers & Galama, 1999). The breaks and peak flux ($F_{\nu, \max}$) are governed by the energy contained in the blast wave and three other physical parameters: ϵ_e , the fraction of energy contained in the emitting electrons, ϵ_B , the fraction of energy contained in the magnetic field, and n_0 , the number density (in cm^{-3}) of particles in the ambient medium.

In addition, the breaks’ behaviour is affected by the dynamical state of the blast wave, which can be in the relativistic, jet-spreading, or non-relativistic phase. The jet spreading phase occurs when $\theta_0 \approx \gamma^{-1}$, where θ_0 is the opening angle of the collimated jet, and γ is the bulk Lorentz factor of the blast wave. The observer begins to ‘notice’ the edge of the jet as it expands, and as γ drops the jet spreads sideways (van Eerten & MacFadyen, 2012). As the shock becomes almost spherical, it becomes non-relativistic at a time t_{NR} which can be approximated by (van Eerten & MacFadyen, 2012)

$$t_{\text{NR}} = 1100 \left(\frac{E_{\text{iso}}}{10^{53} n_0} \right)^{1/3} \text{ d}. \quad (4.18)$$

These three dynamical phases each have their own hydrodynamical evolution, and hence the time

dependences of the synchrotron break frequencies also vary. Values used for the synchrotron spectrum and its evolution in this chapter come from chapter 2 of van der Horst (2007). In this analysis, only the forward shock emission is dealt with.

4.3.2 Energy injection

The magnetar formed by the merger is initially rapidly spinning, with a spin period of the order of 1 ms. After birth, it loses angular momentum in the form of magnetic dipole spin-down (Zhang & Mészáros, 2001), resulting in energy being injected into the outflow and the forward shock for a sustained period, typically of the order of 1000 s. This was investigated for LGRBs by Dall’Osso et al. (2011). The total energy injected into the shock at a time t after merger is given by (cf. Zhang & Mészáros 2001)

$$E_d(t) = \frac{\eta L_0 t}{(1 + t/T_{\text{em}})^2}. \quad (4.19)$$

The parameter η accounts for the ignorance in the efficiency of the transfer of energy from the dipole to the forward shock, both in terms of radiative losses and beaming factor. L_0 is the luminosity of the dipole plateau in erg s^{-1} and T_{em} is the point at which the plateau turns over, known as the characteristic spin-down time-scale. L_0 and T_{em} are both derived from the underlying physical parameters of the magnetar:

$$L_{0,49} = B_{\text{p},15}^2 P_{0,-3}^{-4} R_6^6 \quad (4.20)$$

$$T_{\text{em},3} = 2.05 I_{45} B_{\text{p},15}^{-2} P_{0,-3}^2 R_6^{-6}, \quad (4.21)$$

where $L_{0,49}$ is L_0 in units of $10^{49} \text{ erg s}^{-1}$ and $T_{\text{em},3}$ is T_{em} in units of 10^3 s . I_{45} is the moment of inertia in units of 10^{45} g cm^2 , and is ~ 1 (2) for a 1.4 (2.1) M_{\odot} NS. R_6 is the NS radius in 10^6 cm , $P_{0,-3}$ is the spin period in ms and $B_{\text{p},15}$ is the dipole field strength in units of 10^{15} G . The NS radius is set at $R_6 = 1$, since this is consistent with most equations of state (Lattimer & Prakash,

2004). These relations place limits on the values of L_0 for a given T_{em} , principally through the break-up spin period for an NS (e.g. $P \geq 0.66$ ms for a $2.1M_{\odot}$ NS; Lattimer & Prakash 2004). The upper limit placed on L_0 by P is given by

$$L_{0,49} \leq 2.05 I_{45} T_{\text{em},3}^{-1} P_{\text{lim},-3}^{-2} \quad (4.22)$$

because T_{em} is a fixed quantity for a given GRB.

The two EE bursts in the sample, GRB 060614 and GRB 070714B, are likely to also inject energy into the shock during the EE phase, although without a clear model for what EE is, it is difficult to say how much. To represent EE, the energy profile from Gompertz et al. (2014) was used, where a magnetic propeller is invoked to describe the emission feature. These magnetic propellers accelerate in-falling material to super-Keplerian velocities, ejecting it from the system at relativistic speeds, where it subsequently shocks to produce electromagnetic radiation. The exact physics behind these models is largely irrelevant for this analysis, but the accurate luminosity profile provides a convenient way to introduce EE energy injection to the system. The total energy in the forward shock at a time t is then given by

$$E_{\text{FS}}(t) = E_k + E_{\text{EE}}(t) + E_{\text{d}}(t). \quad (4.23)$$

Here, E_k represents the impulsive energy of the blast wave, and is tied to the prompt emission isotropic equivalent energy $E_{\gamma,\text{iso}}$ through a pre-factor accounting for beaming and efficiency. E_{EE} is the energy injected during EE, representing the luminosity profile from Gompertz et al. (2014) multiplied by another pre-factor κ , again to account for beaming and efficiency. E_{d} is the energy injected by dipole spin-down, given by Equation 4.19. These energies were varied to obtain fits to the data, and the physical implications that the obtained values have for the central engine are discussed in Section 4.5.

4.3.3 X-ray and optical fitting

To perform least-squares fitting for broadband GRB afterglows, one normally requires well-sampled light curves in the X-ray and optical bands, as well as at least two radio bands. Without radio observations, it is very difficult to locate ν_a , since this break is normally found at radio frequencies, and ν_m and $F_{\nu, \max}$ can only be constrained as a combination, rather than individually. Additionally, if ν_c lies above the X-ray frequency then it too becomes poorly constrained. Because of this, large degeneracies can occur where the observed X-ray and optical light curves give combinations of ν_m and $F_{\nu, \max}$ that can be recreated by many different physical parameter values, each having very different implications for the positions of ν_c and ν_a . Thus, any fitting can result in parameter uncertainties spanning several orders of magnitude. For this sample, the available data consist of a well-sampled X-ray light curve, as well as a sparsely sampled optical light curve (sometimes in multiple bands) and just one or two radio observations or limits at best per burst. This is insufficient for fitting in the traditional way, so an order of magnitude search of the parameter space was conducted within reasonable parameter limits.

Synthetic light curves were created through a combination of nine free parameters. Three are well constrained by the data: the characteristic spin-down time-scale T_{em} , the jet break time t_{jb} , and the power-law index of the electron Lorentz factor distribution p . p is the most constrained; this parameter sets the spectral slope, so the simultaneous goodness-of-fit to both the X-ray and R-band data is very sensitive to its value (with a small mitigation for the position of the cooling break: $\beta = \frac{p-1}{2}$ for $\nu_m < \nu < \nu_c$; $\beta = \frac{p}{2}$ for $\nu_c < \nu$). p also sets the temporal decay of the light curves, adding further constraint to its value. Because of these strong constraints, a single value of p was used, obtained by simultaneous model fitting to both the X-ray and optical light curves, as well as the late-time temporal decay in the post-plateau region.

Once this value is obtained, the next most constrained parameter is T_{em} , which determines the time at which the flat plateau region transitions into the late-time temporal decay. There is some

GRB	p	T_{em} (s)	t_{jb} (d)
051221A	2.4	8.0×10^3	≥ 4.0
060614	2.6	2.5×10^4	1.10
070714B	2.9	2.0×10^3	≥ 0.7
130603B	2.5	8.0×10^2	0.35

Table 4.3: The single-value free parameters for each burst, selected by data constraints.

degeneracy between the temporal slope of the decay (controlled by p) and the time at which transition occurs (controlled by T_{em}), particularly in cases where data in this region is sparse, but the extra constraint on p from the spectral slope requirements ensures that a single value can be used for both parameters; values of p outside of a fairly small range are unable to provide simultaneous fits to the X-ray and optical light curves. In cases where the late temporal decay is too steep at both X-ray and optical frequencies for any reasonable combination of p and T_{em} to reproduce, a jet break was used, implemented as a smooth achromatic break at a time t_{jb} . Where no jet break was required at all, models assuming no jet break and ones assuming the earliest jet break allowed by the data were tested to produce the full range of possible fluxes. The single-value model parameters are listed in Table 4.3.

The remaining six parameters are less constrained. They are ϵ_e , ϵ_B , n_0 , L (where $L = \eta L_0$), κ and E_k . Constraints were applied to the range of allowed values for these parameters. ϵ_B has been found to be as low as 10^{-8} (Barniol Duran, 2014; Santana et al., 2014) and as a fraction can be as high as 1. In practice, ϵ_e tends towards higher values than ϵ_B . An upper limit of 1 was set, noting that ϵ_e actually refers to the electron population that is emitting synchrotron radiation, rather than the electron population as a whole, and the lower limit was set as 10^{-3} (Kumar, 2000). n_0 was limited between 10^{-5} and 100 cm^{-3} , in line with what has been found in these sources (Cenko et al., 2011). The upper limit of L was set by the argument in Equation 4.22, and values of this parameter below $\sim 10^{47} \text{ erg s}^{-1}$ are never energetic enough to match the data, so the lower limit was set as $10^{47} \text{ erg s}^{-1}$. Within these limits for L , EE ceases to have any influence on the light curve if $\kappa \lesssim 10^{-2}$. If EE is isotropic, and the observed luminosity is only 1 per cent of the true

Parameter	Minimum	Maximum
ϵ_e	10^{-3}	1
ϵ_B	10^{-8}	1
n_0 (cm $^{-3}$)	10^{-5}	100
L (erg s $^{-1}$)	10^{47}	10^{49a}
κ	10^{-2}	10
E_k (erg)	10^{48}	10^{52}

Table 4.4: Limits on parameters used in the order of magnitude parameter space search. ^a 10^{49} erg s $^{-1}$ is typical, but the real value depends on Equation 4.22

energy (i.e. the conversion efficiency of kinetic to potential energy in the internal shocks is 1 per cent), then the energy delivered to the synchrotron shock front could be up to 100 times higher than observed in the light curve. In practice, however, the emission is (a) unlikely to be fully isotropic, (b) likely to shock more efficiently than 1 per cent, and (c) certain to be less than 100 per cent efficient at delivering its energy to the synchrotron shock front. For these reasons, the upper limit of κ was set at a still fairly generous factor of 10. Finally, the energy in the shock from prompt emission was limited to 10^{48} erg $< E_k < 10^{52}$ erg. The arguments for these limits are identical to those used for κ , except that the prompt emission is known to be beamed (Sari et al., 1999; Frail et al., 2001) so the upper limit is lower, and because the injected energy at early times is negligible, E_k dominates the early light curve so the lower limit can be much less energetic before its influence vanishes. These limits are summarised in Table 4.4.

Each combination of parameters creates a synthetic light curve, and the match to the data was assessed by calculating the χ^2 value for the X-ray observations, as well as observations in the R-band since this is always the best sampled optical light curve. The χ^2 values for the two light curves were assessed separately to avoid a situation where an excellent fit to the X-rays but a poor fit to the optical is indistinguishable from a good fit to both, since the statistics will be dominated by the much better sampled X-ray light curve. Upper limits were not included in the χ^2 calculations, but were subsequently inspected for violations (see Section 4.4). Since there are often fewer R-band data points than free parameters, the reduced χ^2 for the individual bands could

GRB	Reduced χ^2 limit	ϵ_e	ϵ_B	n_0 (cm^{-3})	L (erg s^{-1})	E_k erg	κ
051221A	2.8	0.1–1	10^{-4} – 10^{-1}	10^{-4} – 10^1	10^{47} – 10^{48}	10^{48} – 10^{51}	–
060614	15	0.1–1	10^{-7} – 10^{-3}	10^{-5} – 10^2	10^{48}	10^{48} – 10^{50}	10^{-2} – 10^{-1}
070714B	10	0.1–1	10^{-6} – 10^{-2}	10^{-4} – 10^2	10^{47} – 10^{49}	10^{48} – 10^{52}	10^{-2} – 10^0
130603B	8	0.1–1	10^{-5} – 10^0	10^{-4} – 10^1	10^{47} – 10^{49}	10^{48} – 10^{51}	–

Table 4.5: The range of physical parameters and energy factors found in the models that successfully matched the data (including radio observations). No value for κ is shown for GRB 051221A and GRB 130603B because these bursts do not contain EE. The reduced χ^2 thresholds are also shown.

not be calculated, but the overall reduced χ^2 was calculated by summing the χ^2 contributions and dividing by the combined degrees of freedom. The X-ray band χ^2 was obtained for data points in the X-ray plateau and later, excluding the preceding steep decay. This region is believed to be due the curvature effect (Kumar & Panaitescu, 2000).

4.4 Modelling results

The order of magnitude parameter search returned a variety of viable combinations across the four GRBs. Each was inspected by eye to ensure that no upper limits were violated and that the model was consistent with (i.e. fainter than) the early X-ray emission, since neither of these things were factored into the χ^2 value. The fit each model gave to other optical and UV observations was also inspected for consistency, and those that violated upper limits or provided a poor match to the data were rejected. 16 models were found for GRB 051221A, 6 models were found for GRB 060614, 21 models were found for GRB 070714B, and 17 models were found for GRB 130603B. Example fits for each GRB are shown in Fig. 4.1. The X-ray re-brightening at around 10^{-2} d in GRB 070714B was interpreted as an X-ray flare (e.g. Gompertz et al., 2013) due to its short time-scale and apparent discrepancy with the R-band light curve. This is supported by a spectral hardening shown by the photon index fit on the UKSSDC burst analyser¹ (Evans et al., 2007,

¹www.swift.ac.uk/burst_analyser

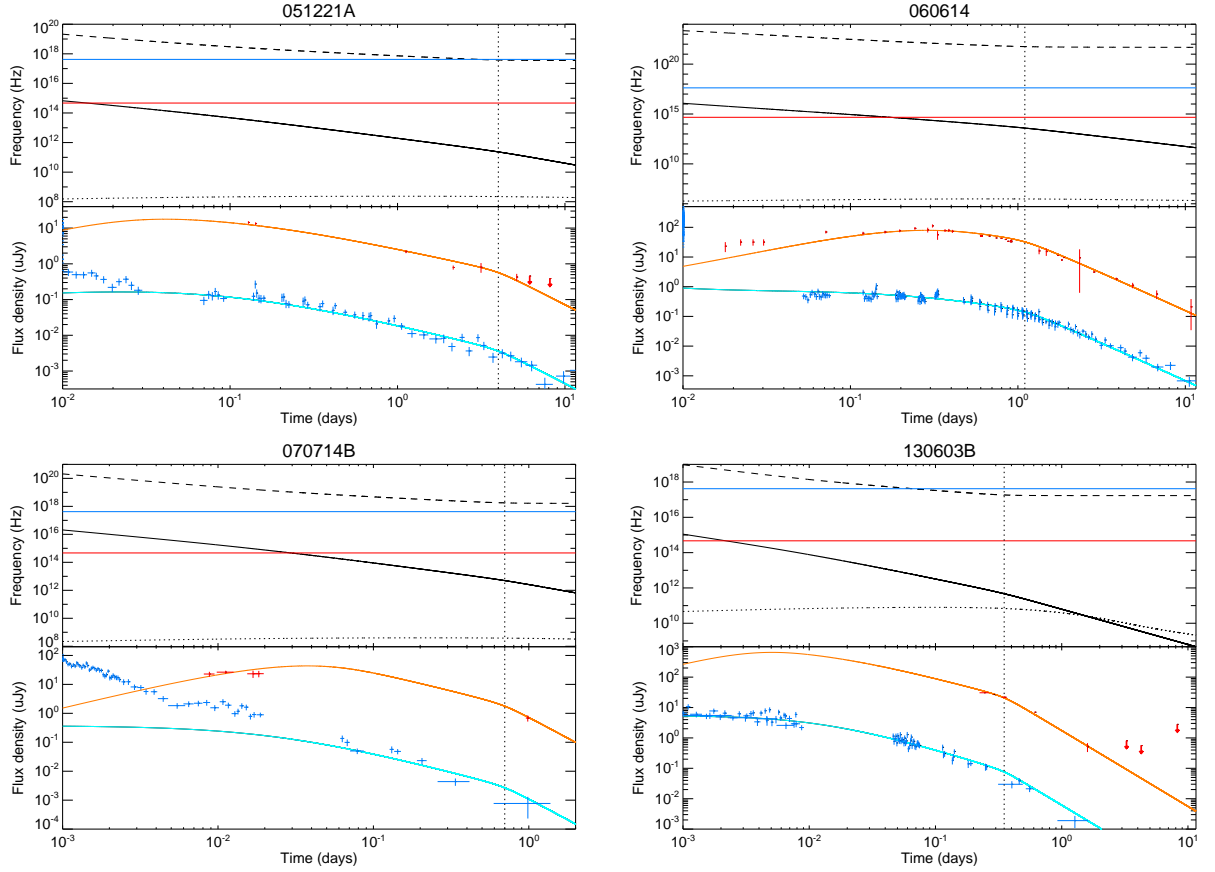


Figure 4.1: Example fits to the X-ray and R-band light curves of the four GRBs in the sample. Top panels: temporal evolution of the three spectral breaks. The black dashed, solid, and dotted lines are the cooling, peak, and self-absorption breaks, respectively. The horizontal blue (red) line marks the X-ray (R-band) frequency for reference. The vertical black dotted line denotes a jet break. Bottom panels: light curves showing the model fit line to the X-ray (blue) and R-band (red) data points. The goodness-of-fit in the X-ray band is only assessed for the plateau data and later, i.e. all data in 060614 and 130603B, and data at times later than 5×10^{-2} d in 051221A and 070714B. The re-brightening at around 10^{-2} d in GRB 070714B is interpreted as an X-ray flare.

2009)

For each parameter combination, the χ^2 values were calculated separately for the X-ray and R-band light curves. These are plotted against each other, and χ^2 cuts were made at both frequencies that return a sample of the best fits for each GRB. This method prevents the much better sampled X-ray light curve from dominating the selection threshold, as would be the case for a combined reduced χ^2 cutoff. The reduced χ^2 limits that result from the combination of χ^2 cutoffs for each burst are shown in Table 4.5. The large variations in these limits are a reflection on how constraining the available X-ray and R-band data are to the models; since the fitting procedure is a simple order of magnitude search rather than a least-squares fit, light curves with larger numbers of data points will be much less forgiving on the models applied. A finer parameter search would reduce χ^2 . The reduced χ^2 limits for all four bursts could also be made more uniform with least-squares fitting; however, this approach leads to very large parameter uncertainties, as previously discussed.

Three of the four GRBs (051221A, 070714B and 130603B) also feature radio detections and upper limits. The presence of radio observations helps to narrow the parameter space, with varying degrees of severity depending on how constraining the observation is. They are shown in Fig. 4.2, plotted alongside the region described by the various light curves from the surviving models, shown in grey. GRB 051221A is the most constrained by radio observations; eight more models were ruled out due to the consecutive upper limits at 8.46 GHz, including all models not featuring a jet break. The dark grey line shows the model that best matches the radio detection for this burst, but it is at odds with the upper limits. In GRB 130603B, the most luminous models appear to violate some of the upper limits; however, these can be retained due to the possible influence of radio scintillation (Frail et al., 1997; Goodman, 1997) which can explain discrepancies in isolated cases. Forward shock emission appears to have some difficulty in matching the radio detections in this burst and GRB 051221A, and possible reasons for this are discussed in Section 4.5. In GRB 070714B, the upper limit is not at all constraining to the physical parameter space.

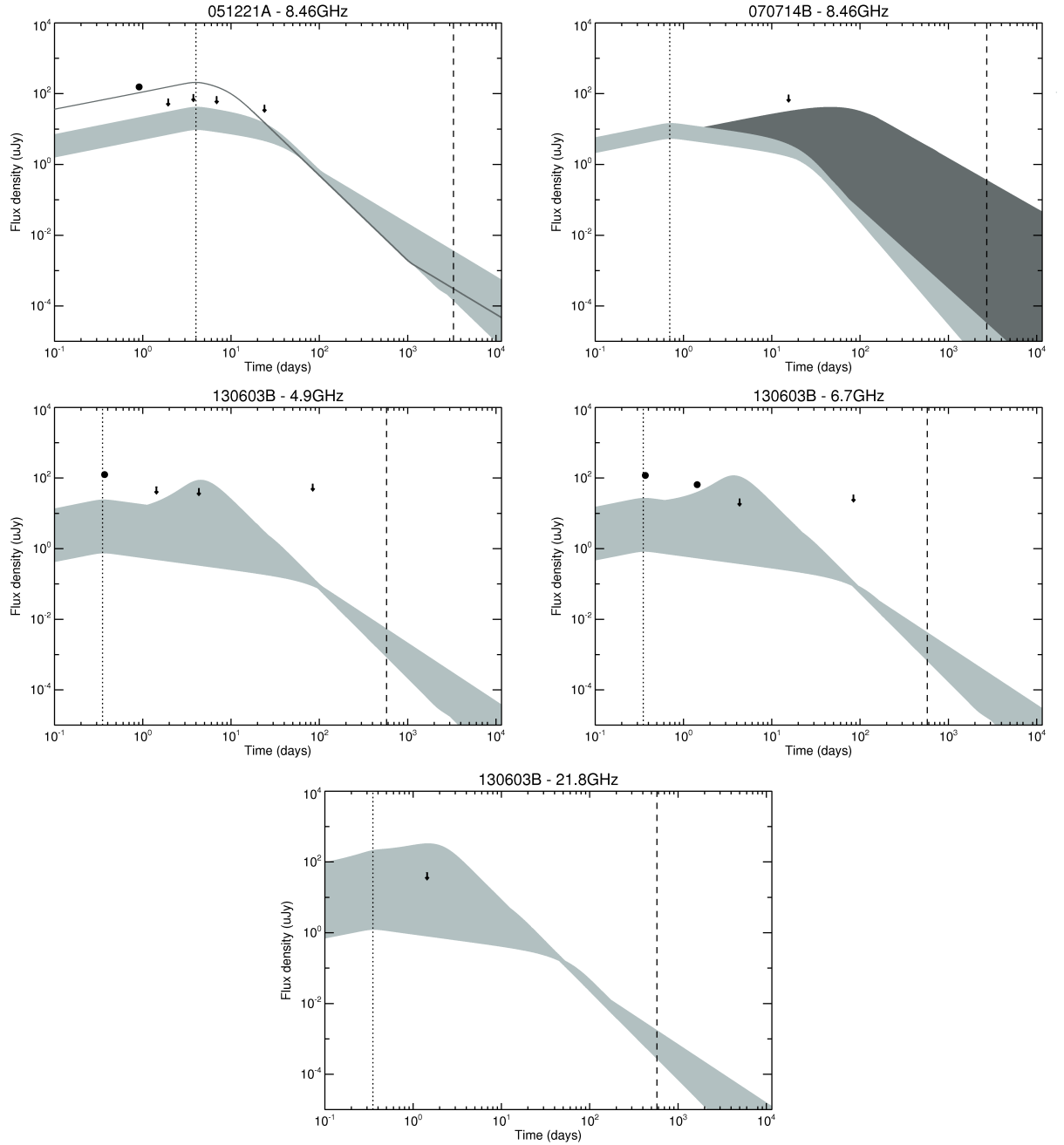


Figure 4.2: The radio detections and upper limits available for the sample of four GRBs. The light grey region shows the range of fluxes described by the light curves of the model fits that are consistent with the broadband data. See Section 4.5 for a discussion in the apparent upper limit violations in GRB 130603B. The dark grey line in GRB 051221A shows the model that comes closest to matching the observations at 8.46 GHz, and its inconsistency with the upper limits illustrates the probable need for reverse shock emission at early times. The dark grey region in GRB 070714B shows the additional range of predictions resulting from the models with no jet break that are consistent with observations. The vertical black dotted line shows the position of the required jet break for GRB 051221A and GRB 130603B, and the position of the earliest jet break allowed by the data for GRB 070714B. The vertical black dashed line marks the 1st of January 2015 for reference.

For each GRB, a fairly wide range of parameters was found. It is immediately obvious from Table 4.5 that a high value of ϵ_e is required in all cases, otherwise the model emission is too faint to match what is observed in both X-rays and optical bands. It should be noted that while broad ranges for the physical parameter values are given, these values only work to reproduce the data in specific combinations. Two of the four GRBs (060614 and 070714B) have values for p that are consistent within the 90 per cent confidence interval with the late-time photon index Γ from the UKSSDC spectrum repository (Table 4.2). The other two lie between the values gained when using the $\nu < \nu_c$ and $\nu_c < \nu$ closure relations, indicating some evidence for a cooling break. Although there may be models with and without cooling breaks for each burst when using different parameter combinations, the example best fits in Fig. 4.1 support this statement, since GRB 051221A and GRB 130603B exhibit late X-ray cooling breaks, while the other two GRBs do not. In two bursts (060614 and 070714B), the data appear to show the peak frequency passing through the R-band, with the cooling break sitting well above the X-ray band. This is a feature of all GRB 060614 models, and is very constraining to the physical parameters because it breaks the $\nu_m - F_{\nu, \max}$ degeneracy.

4.5 Modelling discussion

In some cases, most notably GRB 130603B, models that appear to violate radio upper limits have been retained. This is based on radio scintillation arguments (Frail et al., 1997; Goodman, 1997), where isolated detections and upper limits could be located at scintillation maxima/minima, and therefore have larger errors than quoted. For this reason, the handful of models that do not obey the upper limit in GRB 130603B have been left in the predictions. In cases like the 8.46 GHz light curve for GRB 051221A, however, consecutive limits are unlikely to have all occurred at scintillation minima, and so the models that passed above more than one of them (including all the no jet break models) were rejected.

This causes a problem when trying to explain the earlier radio detection with forward shock emission alone; the only model that comes close in GRB 051221A, shown by the dark grey line in Fig. 4.2, is inconsistent with three of the four radio upper limits. While it could be argued that the single detection in GRB 051221A is itself due to scintillation, the situation is even worse in GRB 130603B, where consecutive detections at 6.7 GHz and a further observation at 4.9 GHz cannot be matched by models without rising above multiple upper limits. The natural explanation for this is the presence of a reverse shock propagating backwards through the ejected material. A reverse shock could produce a radio flare, providing a match to the data while still being masked beneath the forward shock emission at higher frequencies (Kulkarni et al., 1999; Sari & Piran, 1999; Nakar & Piran, 2005; van Eerten, 2014). Reverse shocks are believed to have been observed in both LGRBs (e.g. Akerlof et al., 1999; Chandra et al., 2010; Anderson et al., 2014) and SGRBs (e.g. Soderberg et al. 2006 for GRB 051221A).

The model includes only the most basic features of the magnetar central engine; reverse shock emission or other sources of radiation (e.g. kilonova emission, Piran et al., 2013; Tanvir et al., 2013) have not been incorporated. The aim was to show that a physically motivated, self-consistent central engine, in which a newly formed magnetar injects energy into an expanding forward shock as it loses angular momentum, can be reconciled with the longer wavelength (optical, IR, radio) observations of SGRBs, as well as just the X-ray light curves as is usually done. For this reason, and given the roughness of our fitting routine, the fact that the light curves at all frequencies are well recreated by this bare-bones model is encouraging.

Soderberg et al. (2006) modelled the afterglow of GRB 051221A. The results here are in agreement with theirs, except that a much wider range in ϵ_B was found (10^{-4} – 10^{-1} in this work, compared to 0.12–1/3 in Soderberg et al. 2006) and n_0 (10^{-4} – 10^1 cm $^{-3}$ in this work, compared to $(0.5$ – $2.4) \times 10^{-3}$ cm $^{-3}$ in Soderberg et al. 2006). This narrow range is likely due to the inclusion of a reverse shock in their modelling, and indeed their forward shock only parameter ranges are much broader, although still narrower than what is found here. GRB 051221A was

also modelled by Burrows et al. (2006), who obtain a low- and high-density fit, giving a range of $10^{-4} \text{ cm}^{-3} \leq n_0 \leq 0.1 \text{ cm}^{-3}$ which is in agreement with the findings of this chapter, and similar to the forward shock only results of Soderberg et al. (2006). Both studies find narrow jets, consistent with the range found in Section 4.5.1, and jet break times of 4–5 d. Fan & Xu (2006) also fitted the magnetar model to the broadband observations of GRB 051221A, finding a family of physical parameters within the range of these results.

No broadband modelling has been done on GRB 070714B, but Xu et al. (2009) fitted a model featuring power-law energy injection to GRB 060614, and found a fit with $\epsilon_e \sim 0.12$, $\epsilon_B \sim 2 \times 10^{-4}$, and $n_0 = 0.04 \text{ cm}^{-3}$, in agreement with this range of parameters. By fitting power-law models to the R-band light curves (Della Valle et al., 2006) and a combination of X-ray and optical bands (Mangano et al., 2007), two previous studies have found a jet break at ~ 1.3 d in GRB 060614, consistent with what is found here at 1.1 d.

The broadband afterglow of GRB 130603B was modelled by Fong et al. (2014). As in 051221A, the derived range of density values in this chapter is wider, extending two orders of magnitude lower than Fong et al. (2014). The ϵ_B range also extends down an order of magnitude further. These ranges highlight the large degeneracies in the parameters; ϵ_e is confined to a relatively small range (\sim one order of magnitude) because ν_m and $F_{\nu, \text{max}}$ are well constrained by the data, whereas ν_c and ν_a are often unconstrained, leading to a variety of acceptable parameter combinations. Fong et al. (2014) find a jet break at ≈ 0.47 d, and a jet opening angle in the range $4^\circ - 14^\circ$, both of which are consistent with these findings. Finally, the magnetar spin period and dipole field values calculated by Fong et al. (2014) for the dipole spin-down injection case intersect with the line for GRB 130603B shown in Fig. 4.3. Fan et al. (2013) also showed that the magnetar model was capable of reproducing the broadband emission observed in GRB 130603B for one combination of physical parameters that lies within the derived range.

4.5.1 Energetics

The radiative efficiency of a GRB is defined as (cf. Zhang, 2007)

$$\zeta = \frac{E_{\gamma,\text{iso}}}{E_{\gamma,\text{iso}} + E_{k,\text{iso}}} \quad (4.24)$$

and gives a direct measure of how efficiently the total energy is converted into EM radiation. Here, we calculate E_k for each burst, which is the energy delivered to the afterglow emission site by the prompt impulse, and makes no assumption on geometry. The lower limit of E_k is not at all constraining; the fit to the plateau emission depends much more on the luminosity of the dipole spin-down injection, L . Values for E_k of 10^{48} erg and below are indistinguishable from one another, and for a given $E_{\gamma,\text{iso}}$ will just represent an asymptotic approach to a radiative efficiency of 1, which is unphysical. The upper limits of E_k are far more important, since they are constrained by observation in that too much energy contribution will drive the model fluxes up above what is observed, and will mask the plateau feature in cases where E_d is negligible in comparison to E_k . The approximate maximum value of $E_{k,\text{iso}}$ is given by assuming that the upper limit of E_k came from a strongly beamed geometry with a beaming factor of ~ 1000 , i.e. the upper limit of $E_{k,\text{iso}}$ is as much as a thousand times greater than the upper limit of E_k . The radiative efficiency can then be used to calculate the implied opening angle (cf. Racusin et al., 2009a):

$$\theta_j = 0.057 t_{\text{jb}}^{3/8} \left(\frac{3.5}{1+z} \right)^{3/8} \left(\frac{\zeta}{0.1} \right)^{1/8} \left(\frac{n_0}{E_{\gamma,\text{iso},53}} \right)^{1/8}. \quad (4.25)$$

The range of calculated efficiencies and opening angles are shown in Table 4.6. The derived efficiencies are consistent with Zhang (2007), who found typical values of < 10 per cent in their sample. Note that for the two EE GRBs, these calculations may be affected by the energy contribution of EE. We find that GRB 060614 tends to demand higher values of ϵ_e and ζ than the other bursts, which is symptomatic of its more luminous and longer lasting afterglow plateau putting extra demands on the available energy. The derived opening angles are consistent with the results of

GRB	$E_{\gamma,\text{iso}}$ (erg)	ζ	θ_j (deg)
051221A	$1.5 \times 10^{51,a}$	$\geq 1.5 \times 10^{-3}$	$\geq 2.37 (\leq 22.7)^*$
060614	$2.5 \times 10^{51,b}$	$\geq 2.0 \times 10^{-2}$	1.62–19.7
070714B	$1.6 \times 10^{51,c}$	$\geq 1.6 \times 10^{-4}$	$\geq 0.87 (\leq 14.4)^*$
130603B	$1.0 \times 10^{51,d}$	$\geq 1.0 \times 10^{-3}$	1.01–10.0

Table 4.6: Calculated minimum radiative efficiencies and ranges of opening angles. ^aSoderberg et al. (2006); ^bMangano et al. (2007); ^cGraham et al. (2009); ^dFong et al. (2014). *Upper limit derived from the earliest permissible jet-break in cases where the data are consistent with isotropic emission.

Ryan et al. (2015). Their results (in degrees) are $26.0_{-2.20}^{+1.80}$ for GRB 051221A, $17.0_{-4.93}^{+7.08}$ for GRB 060614 and $19.1_{-6.38}^{+6.38}$ for GRB 070714B, where the errors are 1σ . These values were obtained by fitting to the X-ray light curves only.

4.5.2 Magnetar properties

The well constrained value of T_{em} and the results for L mean that the magnetar properties can be approximated. These approximations assume 100 per cent efficiency and isotropic emission, which is unlikely to be the case; however, in energetic terms a reduction in one compensates for a reduction in the other, and the large starting uncertainty associated with a simple order of magnitude search for L means that this assumption is sufficiently accurate in the context of other sources of error. The range of magnetar spin periods and field strengths is illustrated in Fig. 4.3. These properties are not well constrained in three out of four bursts due to the degeneracy created by the wide range of physical parameters, as well as uncertainties in measuring the dipole plateau due to contamination from the prompt and EE components. The normalisation of the B – P relation is set by the value of T_{em} for each burst, and the suitable combinations run from the minimum spin break-up period up to the point at which the plateau becomes too faint for a good fit, at around $L = 10^{47} \text{ erg s}^{-1}$.

The implications for EE in GRB 060614 and GRB 070714B are not well defined. While a range

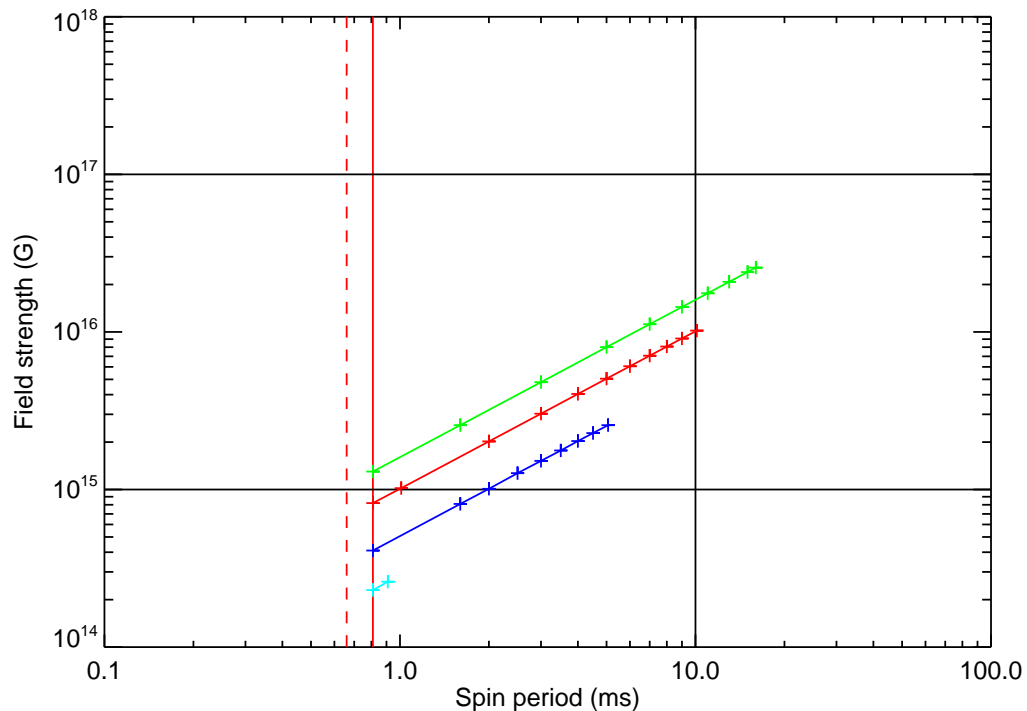


Figure 4.3: Magnetar spin period and dipole field strength combinations that satisfy the luminosity limits and T_{em} values of the four GRBs. Blue – GRB 051221A; light blue – GRB 060614; red – GRB 070714B; green – GRB 130603B. The solid (dashed) vertical red line marks the spin break-up period for a 1.4 (2.1) M_{\odot} NS (Lattimer & Prakash, 2004). The vertical black line represents the maximum allowed spin period at birth, based on the conservation of angular momentum of a white dwarf binary merger (Usov, 1992). The lower horizontal limit marks the minimum magnetic field required to produce a GRB observable in the gamma band (Thompson, 2007) and the upper limit is the nominal threshold for fast field decay.

of energies that work in the context of the light curves can be found, the physical interpretation is not constrained in terms of beaming or efficiency, save that the results lie in the region found here. One central engine capable of providing such a result is a magnetic propeller (Gompertz et al., 2014). The EE profile used here borrowed the luminosity curve for a 40 per cent efficient isotropic propeller (without the pre-factor κ), so the EE contribution is energetically consistent with the propeller model, however in this context it was used as a simple indicator of luminosity, and the restrictions it imposes on P and B of the underlying magnetar were not applied.

Telescope	Sensitivity (μJy)	Reference
<i>60 MHz:</i>		
LWA1	38000	Ellingson et al. (2013)
LOFAR	5000	van Haarlem et al. (2013)
<i>150 MHz:</i>		
MWA	1200	Tingay et al. (2013)
LOFAR	300	van Haarlem et al. (2013)
<i>1.4 GHz:</i>		
GMRT	150	Ghirlanda et al. (2014)
WSRT/Apertif	50	Ghirlanda et al. (2014)
ASKAP	50	Ghirlanda et al. (2014)
MeerKAT phase 1	9	Ghirlanda et al. (2014)
MeerKAT phase 2	6	Ghirlanda et al. (2014)
SKA phase 1	1	Ghirlanda et al. (2014)
SKA phase 2	0.15	Ghirlanda et al. (2014)
<i>15 GHz:</i>		
AMI	70	Zwart et al. (2008)
VLA	5	Ghirlanda et al. (2014)
<i>100 GHz:</i>		
CARMA	900	Bock (2006)
ALMA	6	[A]

Table 4.7: Detection sensitivities for different instruments at the frequencies for which we calculate flux density prediction light curves. Limits are 5σ and assume a 12 h integration time. [A] – almascience.eso.org/proposing/sensitivity-calculator

4.6 Implications for radio emission

The models that successfully match the available broadband observations in Section 4.4 are used to create synthetic light curves in a variety of radio frequencies: 60 and 150 MHz, and 1.4, 15, and 100 GHz. The light curves combine to give a region of predicted flux densities, showing the bounds of what the radio afterglow should have looked like for each GRB at each frequency, given the imposed restrictions of the specific physical model. This is plotted in Fig. 4.4. Table 4.7 shows the sensitivity thresholds for modern-day and future radio telescopes that observe at the frequencies plotted, and a selection of these are superimposed on the light curves. The detectabil-

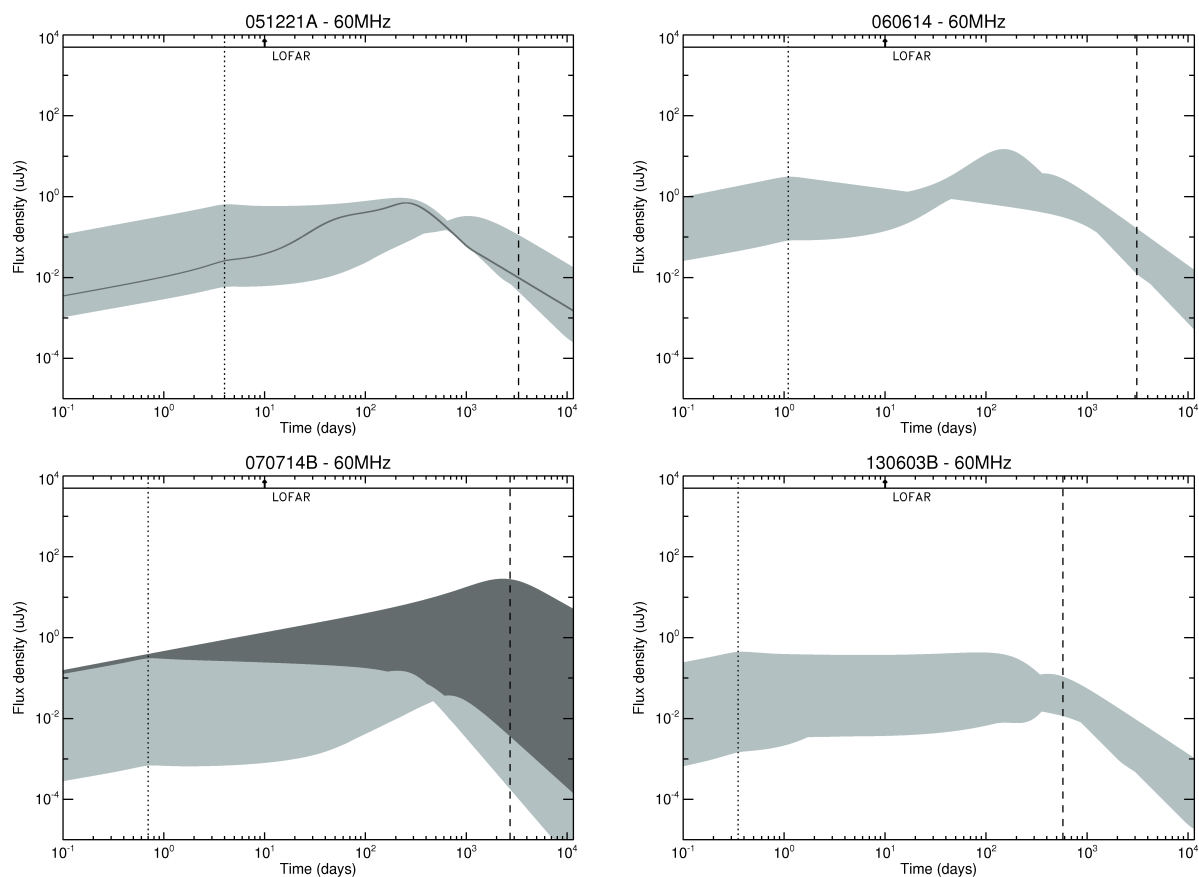


Figure 4.4a: Predicted flux density light curves at 60 MHz for the four GRBs in our sample. The dark grey line in GRB 051221A shows the model that comes closest to matching the observations at 8.46 GHz in Figure 4.2. The dark grey region in GRB 070714B shows the additional range of predictions resulting from the models with no jet break that are consistent with observations. The vertical black dotted line shows the position of the required jet break for GRB 051221A, GRB 060614 and GRB 130603B, and the position of the earliest jet break allowed by the data for GRB 070714B. The vertical black dashed line marks the 1st of January, 2015, for reference. Selected limits from Table 4.7 are over-plotted.

ity of each GRB radio afterglow is assessed. The flux densities are in general modest, typically peaking in the μJy range; however, the results for the anomalously bright GRB 060614 do extend up to mJy. The signal from each GRB is suppressed by the jet break, which curtails the initial brightening of the emission early on in the light curve in most cases. The region either side of this break usually represents the best opportunity to observe the radio afterglow.

At the lower frequencies (60 and 150 MHz), only the Low Frequency Array (LOFAR) at 150 MHz gets close to being within an order of magnitude of the predictions. The picture is slightly better

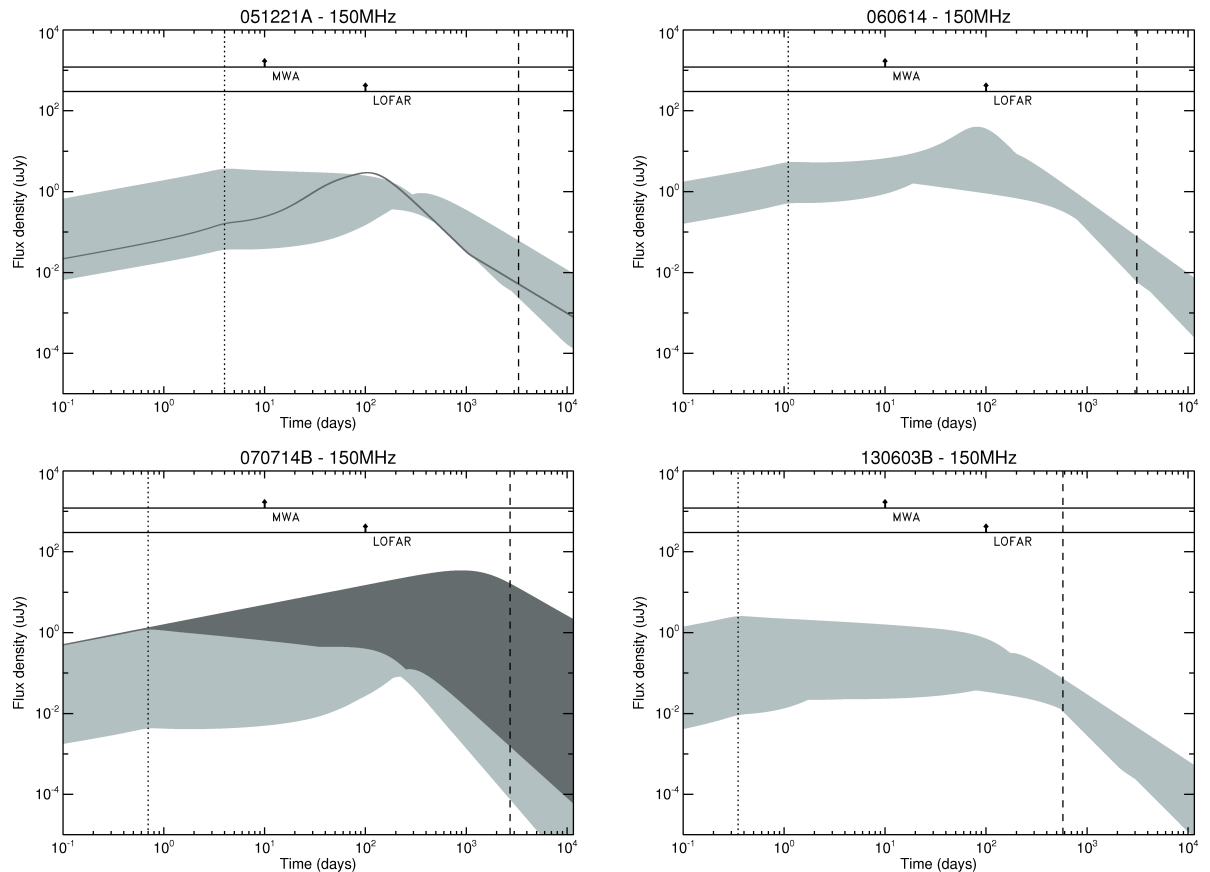


Figure 4.4b: 150 MHz.

moving to higher frequencies; in the near future at 1.4 GHz, the Westerbork Synthesis Radio Telescope (WSRT)/Apertif and the Australian Square Kilometre Array Pathfinder (ASKAP) will be sensitive enough to be capable of observing the brighter models in GRB 060614, and graze the upper limits of the GRB 070714B predictions. MeerKAT would have been capable of detecting at least the upper portion of all four bursts, and could have resolved the entire predicted region of GRB 060614 if observations had been made around the time of the jet break.

At 15 GHz, the Arcminute Microkelvin Imager (AMI) is capable of observing the upper reaches of the predictions for all but the highest z burst (GRB 070714B) for around a week, possibly even a month for the brighter portion of GRB 060614. The Very Large Array (VLA), in its expanded capacity (Perley et al., 2011), would have been able to go deeper than our lower limits in each

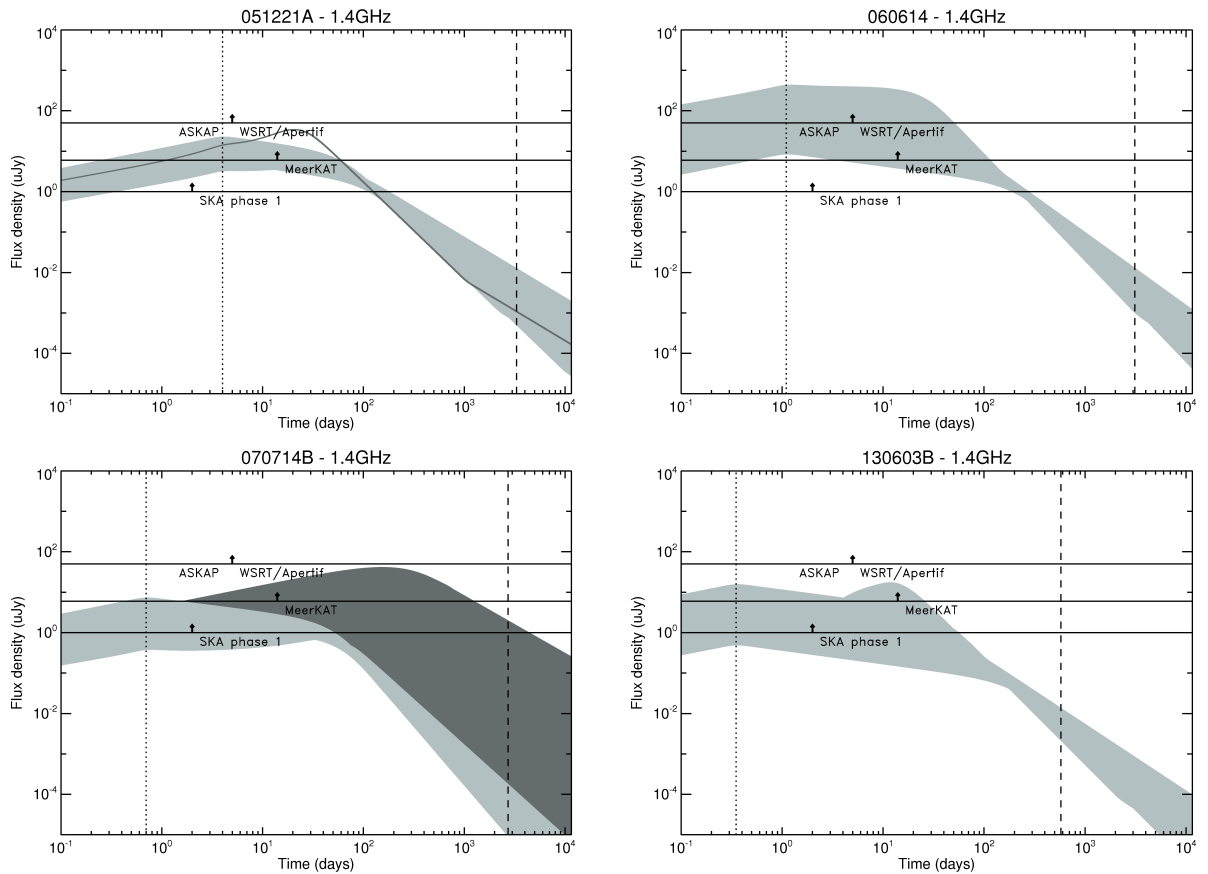


Figure 4.4c: 1.4 GHz.

burst except GRB 130603B in the first week, and provide meaningful limits on the evolution of the radio afterglow for up to a year after trigger. Finally, at 100 GHz the Combined Array for Research in Millimetre-wave Astronomy (CARMA) may have been able to detect the brightest models in GRB 060614 and GRB 130603B, and the Atacama Large Millimetre Array (ALMA) would have been able to provide limits similar to those mentioned for the VLA, with a window of weeks in GRB 051221A and GRB 070714B, and months in GRB 060614, where the entire predicted region lay above its sensitivity threshold.

The model fluxes show that previous radio observations, while able to limit some of the physical parameter space, were not deep enough to place serious constraints on the magnetar model. However, the recently upgraded VLA (Perley et al., 2011) and ALMA are now at μJy sensitivity, deep

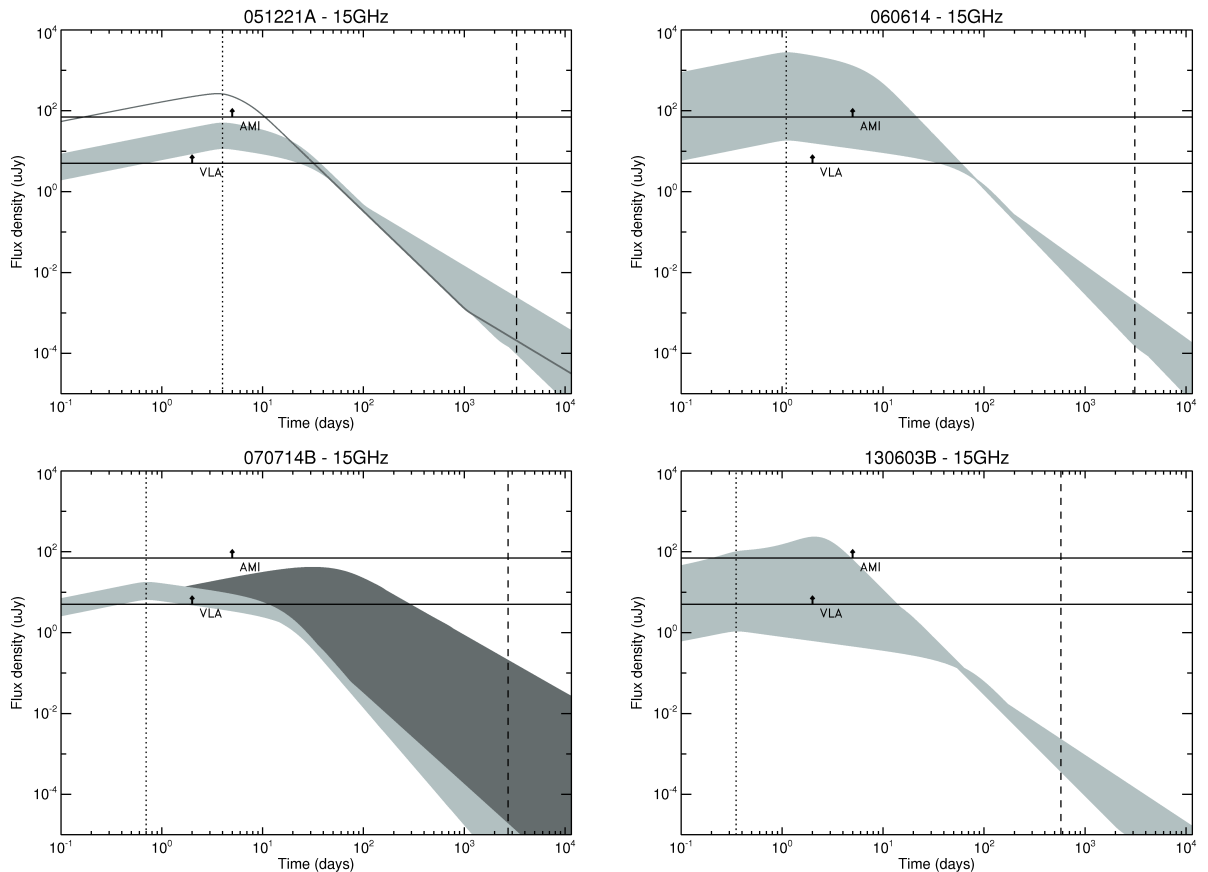


Figure 4.4d: 15 GHz.

enough to probe even the faintest predicted models. Either telescope can now provide meaningful and highly constraining restrictions on a central engine invoking dipole spin-down injection into a forward shock by making observations within the first week or two after trigger, assuming the four GRBs discussed here are representative of the sample as a whole. Since the sample contains the highest recorded spectroscopic SGRB redshift ($z = 0.9224$; GRB 070714B) and the results in Table 4.5 show CBM densities at or near the observed lower limit $n_0 \sim 10^{-5} \text{ cm}^{-3}$, it seems that the sample does represent SGRB and EE GRB radio fluxes as a whole, rather than the most luminous cases.

The Square Kilometre Array (SKA) paints a rather brighter picture for the future; the results suggest that even at phase 1, we should expect to see magnetar-injection driven 1.4 GHz afterglows

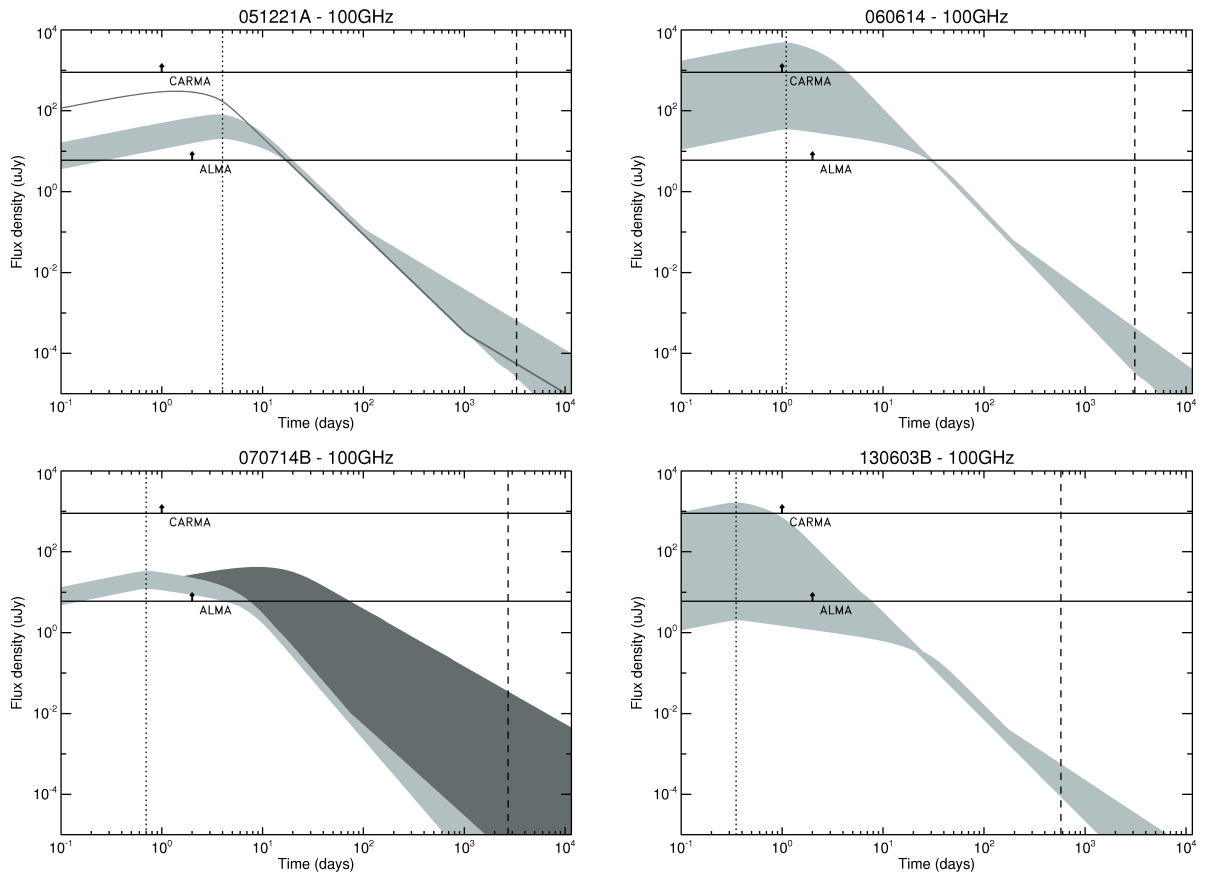


Figure 4.4e: 100 GHz.

for months after trigger if the model is to be believed. All four GRBs shown here would be observable for months, in some cases up to a year after trigger, with only the very faintest models in GRB 070714B and GRB 130603B lying below the sensitivity threshold. By phase 2, all four of the radio afterglows in the sample would have been visible for a year or more, and the entire predicted flux density region could be explored for each with the correct observing strategy. These findings are in agreement with Feng et al. (2014), who simulated radio afterglow light curves for compact object mergers at the advanced Laser Interferometer Gravitational-wave Observatory (aLIGO) horizon. The simplest case of merger followed by injection is considered here; however, the radio signal from these mergers may be further enhanced by other processes such as macronovae (Piran et al., 2013).

4.7 Conclusions

Order of magnitude fitting to the broadband afterglows of a sample of four GRBs was performed. A physically motivated central engine was applied, invoking energy injection into a forward shock from a magnetar as it rapidly loses angular momentum along open magnetic field lines. By imposing the limitations of a self-consistent central engine for the energy profile of each GRB, the available parameter space for the physics underlying the evolution of the blast wave as it expands into the ambient medium is narrowed. Combinations of these parameters are tested against the data, resulting in a family of models that accurately recreate observations. These models are then used to predict the radio signature from the central engine, and are assessed for detectability.

The results show that current broadband observations are consistent with the magnetar injection model, as physical parameters that lie within the allowed ranges are found for all bursts. Some discrepancies exist at radio frequencies, suggesting that previous early detections captured emission from a reverse shock propagating backwards through the ejecta, rather than a forward shock moving outwards into the CBM. It is found that while recent observational detection thresholds are not constraining to the magnetar model, state-of-the-art facilities such as the upgraded VLA and ALMA are now capable of observing to depths greater than the predicted flux density range if observations are made in the first few weeks, and to maximum sensitivity. It is also shown that SKA will be capable of observing to depths in excess of the model predictions, and hence is expected to observe these signatures, or impose strict limits on the physical parameters.

4.8 Appendix A: Flux density equations

Using the equations below, the flux (F ; $\text{erg cm}^{-2} \text{s}^{-1}$) observed in a bandpass bounded by a lower limit ν_l and upper limit ν_h (both Hz) can be converted to a flux density (F_{ν_p} ; Jy) at the bandpass logarithmic mid-point (ν_p ; Hz), assuming a power-law spectrum with an index β ($F_\nu = \nu^{-\beta}$).

$$\begin{aligned}
 F_{\nu_p} &= \frac{(\beta - 1)F}{\nu_l} \left(\frac{\nu_l}{\nu_h}\right)^{\beta/2} \left[1 - \left(\frac{\nu_h}{\nu_l}\right)^{1-\beta}\right]^{-1} && \text{for } \beta > 1 \\
 F_{\nu_p} &= \frac{F}{\nu_p} \left[\ln\left(\frac{\nu_h}{\nu_l}\right)\right]^{-1} && \text{for } \beta = 1 \\
 F_{\nu_p} &= \frac{(1 - \beta)F}{\nu_h} \left(\frac{\nu_h}{\nu_l}\right)^{\beta/2} \left[1 - \left(\frac{\nu_l}{\nu_h}\right)^{1-\beta}\right]^{-1} && \text{for } \beta < 1
 \end{aligned} \tag{4.26}$$

5

Conclusions and future prospects

During this thesis, the magnetar model has been rigorously tested for consistency with the broad-band observations of EE GRBs. This chapter presents the main findings and conclusions of the undertaken work, as well as a summary of the current understanding of the classification of EE GRBs and the role magnetars may play in driving them. Future prospects for investigation are also discussed, both with modern technology, and in the context of upcoming observational facilities.

5.1 Key conclusions

The investigations outlined in the science chapters of this thesis have yielded a number of key conclusions on the potential of magnetars as the central engines of EE GRBs.

Firstly, as shown in Chapter 2, the energy release calculated from the k-corrected light curves is consistent with the magnetar model; the observed luminosity is within the energy constraints imposed by the rotational energy reservoir of a millisecond spin period NS. Furthermore, accounting for this energy release has the effect of shifting the derived birth spin periods from a region outside of the expected range into the region predicted by theory. Making this one simple assumption about the nature of EE GRBs brings them into line with the properties of SGRBs, strongly suggesting that the two classes are related. When modelled as magnetars, the EE and SGRB samples are indistinguishable from one another in terms of the derived spin periods and dipole fields of the central NS, and so the difference between the two classes must be attributed to either the environment or the formation mechanism.

Having shown that the EE feature is likely to be drawn from the rotational energy reservoir, the main conclusion from Chapter 3 is that a magnetic propeller provides a natural divide between EE GRBs and SGRBs because it implies that the existence of EE is predicated not on the properties of the magnetar, but on the existence of a fallback accretion disc. One way to provide this difference is with an unequal mass binary merger, where the less compact of the two components can be tidally stripped during in-spiral, providing the fallback disc required to initiate the propeller. The results for Chapter 3 show that the required luminosity can be produced by fallback discs with masses of a few $10^{-2} M_{\odot}$ to a few $10^{-3} M_{\odot}$, but the conversion efficiency of kinetic energy to electromagnetic radiation in shocks between expanding shells of ejecta must be fairly high, ≥ 10 per cent. As discussed in Section 3.5.1, the low Lorentz factors used when investigating the propeller emission mean that the propeller-driven shells will most likely never catch up to the forward shock, and therefore cannot contribute to the broadband afterglow via energy injection.

The key result from Chapter 4 is that the broadband observations of a sample of short and EE GRBs are well matched by a model in which a magnetar injects dipole radiation into a forward shock. This presents a more rigorous test of the magnetar central engine, whereas previous chapters made assumptions on the efficiency at which injected energy was reprocessed in the shock and re-radiated at X-ray frequencies. This chapter provides spectra and templates that reproduce the observed emission, and crucially show that the lack of radio detections is not yet overly damning to the magnetar model, as might be expected for a central engine with a great deal of implied energy injection.

5.2 The current status of the magnetar model

The results of this thesis provide strong evidence that EE GRBs are likely to be a subclass of SGRBs, and that both are consistent with the magnetar model. The consistency is suggestive, but the evidence is currently far from conclusive. It is generally accepted that SGRBs are produced during the merger of two compact objects, but this itself has not yet been conclusively confirmed, and probably won't be until (or unless) the GW signal is observed by aLIGO and/or advanced Virgo, or until multiple high-confidence kilonova detections are made. In terms of the BH vs magnetar central engine debate, both candidates have strengths and weaknesses. The main strengths of the magnetar model have been extolled throughout this thesis; it has proven itself in numerous studies to be highly adept at reproducing the broadband signature of SGRB afterglows in a way that the BH central engine is not always able, and is consistent with the energetic constraints inherent to a rotating NS. It has also been shown that the criticisms regarding the lack of observed radio signatures are premature (e.g. Metzger & Bower, 2014). However, several valid criticisms remain.

5.2.1 The weaknesses of the magnetar model

There are many hurdles the magnetar central engine must overcome before it is more widely accepted by the GRB community. Firstly, there is a degree of doubt over the feasibility of a long-lived massive NS remnant in the aftermath of a binary NS merger. Broadly, this is a question of the NS equation of state, and concerns will be alleviated by the continued discovery of more massive NSs in nature (e.g. Demorest et al., 2010; Antoniadis et al., 2013). Suggestions that the binary components are white dwarfs instead of NSs are problematic because white dwarfs are not expected to receive significant natal kicks (e.g. Berger, 2014), so the large offsets that some SGRBs possess from their host galaxies then become difficult to reconcile with theory.

The main criticism of the model is its apparent inability to launch jets with the requisite Lorentz factors (e.g. Dessart et al., 2009; Murguia-Berthier et al., 2014). The prompt emission is not investigated in this thesis, but it of course goes without saying that if the magnetar is unable to supply the prompt emission, then its ability to convincingly produce the afterglow is irrelevant. The main problem is that a high baryon density ‘chokes’ the jet, meaning that it cannot be launched at a velocity sufficient to power an SGRB. This problem can be alleviated somewhat with the contribution from magnetic fields, but remains the biggest single issue with the magnetar central engine.

5.3 Consistency tests

One of the main checks for consistency that arises from this thesis is the development of templates that are capable of finding a match to the broadband signature of magnetar energy injection. This allows the constraint of the spectrum, predicts the physical parameters of the CBM, and enables the production of light curves at any frequency. The predictions of this work, outlined in Chapter 4, are testable with modern-day radio telescopes, primarily the VLA and ALMA, and provide a

method by which magnetar-driven SGRBs may be ruled out via the flux density observed in the radio band, which is predicted to be higher than that of a BH central engine due to the large amount of energy injection implicit to the model. These templates can be applied to new SGRBs as they are detected, requiring only a well-sampled X-ray light curve (usually provided by *Swift*) and a modest number of observations at other frequencies.

Another test of the predictions is to combine *Swift* data with *Fermi* observations; the bandpass of GBM is 8 keV – 40 MeV (Meegan et al., 2009), and many of the predicted cooling breaks lie within this range. Constraining the cooling break has important implications for constraining the physical parameters of the shock, and this in turn will narrow the parameter space in which the self-absorption break resides. Tightening the available flux density region will provide a sterner test for the magnetar model. However, very few (if any) GRBs with sufficient data to perform the analysis have both *Swift* and *Fermi* observations.

5.4 Future work

The magnetic propeller model that was developed in Chapter 3 was also applied to the giant flares seen in a small sample of LGRBs by some undergraduate project students that were supervised during this thesis, and was found to give a reasonable match the phenomenological shape. If these two features are really produced in the same way, then a spectral analysis of both ought to yield comparable results. This is somewhat complicated by the features appearing in different classes of GRB, but the long sample is believed to contain examples of magnetar-driven afterglows in the aftermath of core-collapse (e.g. Lü & Zhang, 2014), so the presence of a magnetic propeller is feasible in both cases.

One of the most obvious opportunities that arises from the work in this thesis is the extension of the SGRB prediction templates to the BH central engine. The BH suffers from an inability

to provide long-term energy injection in order to produce the late-time plateaux seen in half the sample, but several models exist to try to rectify this situation: an extended coasting phase (Duffell & MacFadyen, 2014), a fallback accretion model (Rosswog, 2007), and an excavated pulsar cavity scenario (Holcomb et al., 2014). Any or all of these can be developed into a radio predictions code in the same way as was done for dipole injection in Chapter 4, and this library of templates can then be compared to each new burst, with the aim of ruling some of them out against observations. They each imply different levels of energy injection after the initial prompt emission episode, and therefore could well predict observationally distinct radio emission evolution.

5.4.1 The square kilometre array and the survey science era

Although EE and SGRB X-ray emission can be reproduced reasonably well by both of the competing central engines, the radio signature ought to be very different. The SKA¹ is the perfect tool to exploit this observational diagnostic because, as shown in Chapter 4, it will be sensitive enough to observe the radio signature of magnetar energy injection for almost all combinations of physical parameters. In addition to its potential to distinguish between progenitor models for on-axis bursts, the SKA is also expected to detect off-axis GRB afterglows (Granot et al., 2002), i.e. those GRBs for which the prompt emission jet is not pointed towards the Earth, and so no trigger is detected, thanks to its large FOV and excellent sensitivity. The rate of these off-axis detections will be extremely useful in determining the true rate of GRBs in the Universe, as well as the beaming angle. These capabilities mean that the SKA will be an invaluable tool in progressing the field. SKA pathfinders such as MeerKAT and ASKAP are already in operation, and the construction of phase 1 is scheduled to take place from 2018 to 2023.

A related instrument that will augment and enhance the efforts of the SKA is the Large Synoptic Survey Telescope (LSST²; Ivezić et al., 2008). LSST will observe each patch of sky for thirty

¹www.skatelescope.org

²www.lsst.org/lsst/

seconds every three to four days in the optical band, and is expected to detect 10 – 100 SGRB orphan afterglows per year, as well as approximately 1000 LGRB orphans (LSST Science Collaboration et al., 2009). This switch from survey follow-up to survey direct science at both optical and radio frequencies is sure to yield exciting new discoveries and advancements in GRB science. Construction of the LSST began in 2014, with engineering first light anticipated in 2019, and the commencement of the 10 year survey expected to begin two years later, in 2021.

5.4.2 The advent of gravitational wave astronomy

The compact object merger progenitor hypothesis for SGRBs will be put to the test with the inauguration of the advanced-phase gravitational wave detectors. In their previous incarnations, LIGO and Virgo were able to detect the GW signal of an in-spiralling binary system composed of two $1.4 M_{\odot}$ NSs out to a maximum of 49.3 Mpc ($z \sim 0.01^3$; The LIGO Scientific Collaboration & The Virgo Collaboration, 2012), where the detection horizon is defined as the distance at which an optimally oriented and optimally located equal-mass compact binary in-spiral would give an average SNR of 8 in the interferometer. There has never been a recorded SGRB within this horizon, and only one LGRB in the archive has occurred closer: GRB 980425A, at $z = 0.0085 \pm 0.0002$ (Tinney et al., 1998). LGRBs are not believed to be binary NS mergers, and type Ib/c supernovae are not expected to be particularly strong GW candidates. Regardless, neither LIGO nor Virgo were yet constructed at this time. The nearest recorded GRB during a science run was LGRB 060218, at $z = 0.03345 \pm 0.00006$ (Mirabal et al., 2006), which was not detected.

In the advanced era, aLIGO is predicted to achieve a binary NS detection *range*⁴ of 215 Mpc when optimised for these phenomena (LIGO Scientific Collaboration et al., 2013), which translates into a horizon (as defined in the previous paragraph) of 485.9 Mpc ($z \sim 0.1$). The latter measure

³converted using Wright (2006)

⁴The volume- and orientation-averaged distance at which a compact binary coalescence consisting of two $1.4 M_{\odot}$ NSs gives a matched filter SNR of 8 in a single detector (Finn & Chernoff, 1993).

Year	Estimated Duration	aLIGO range (Mpc)	AdV range (Mpc)	Predicted BNS detection rate	% localised to	
					5 deg ²	20 deg ²
2015	3 months	40 – 80	-	0.0004 – 3	-	-
2016/17	6 months	80 – 120	20 – 60	0.006 – 20	2	5 – 12
2017/18	9 months	120 – 170	60 – 85	0.04 – 100	1 – 2	10 – 12
2019+	(per year)	200	65 – 130	0.2 – 200	3 – 8	8 – 28
2022+	(per year)	200 ^a	130	0.4 – 400	17	48

Table 5.1: Planned science runs for the aLIGO and advanced Virgo (AdV) gravitational wave detectors, with the expected binary NS merger detection rates (LIGO Scientific Collaboration et al., 2013). ^aIncluding LIGO India.

is a factor of 2.26 larger than the former (LIGO Scientific Collaboration et al., 2013). This is getting close to the lowest recorded redshift for an SGRB, at $z = 0.1218 \pm 0.0003$ (Rowlinson et al., 2010b), and the predicted rate of GW counterparts to SGRB X-ray detections is discussed in Rowlinson et al. (2013). Table 5.1 shows the expected science runs and ranges of aLIGO and advanced Virgo. In addition to these interferometers (including LIGO India), the Japanese Kamioka Gravitational Wave Detector (KAGRA) is currently under construction, and is due to begin operations in 2017 (Aso et al., 2013).

References

- Akerlof C. et al., 1999, *Nature*, 398, 400
- Akiyama S., Wheeler J. C., Meier D. L., Lichtenstadt I., 2003, *ApJ*, 584, 954
- Amati L., 2006, *MNRAS*, 372, 233
- Amati L. et al., 2002, *A&A*, 390, 81
- Anderson G. E. et al., 2014, *MNRAS*, 440, 2059
- Antoniadis J. et al., 2013, *Science*, 340, 448
- Aptekar R. L. et al., 1995, *Space Science Rev.*, 71, 265
- Arnaud K. A., 1996, in *Astronomical Society of the Pacific Conference Series*, Vol. 101, *Astronomical Data Analysis Software and Systems V*, Jacoby G. H., Barnes J., eds., p. 17
- Aso Y., Michimura Y., Somiya K., Ando M., Miyakawa O., Sekiguchi T., Tatsumi D., Yamamoto H., 2013, *Phys. Rev. D*, 88, 043007
- Atwood W. B. et al., 2009, *ApJ*, 697, 1071
- Band D. et al., 1993, *ApJ*, 413, 281
- Barbier L. et al., 2005, *GRB Coordinates Network*, 4397, 1
- Barkov M. V., Pozanenko A. S., 2011, *MNRAS*, 417, 2161
- Barniol Duran R., 2014, *MNRAS*, 442, 3147
- Barthelmy S. D. et al., 2005a, *Space Science Rev.*, 120, 143
- Barthelmy S. D. et al., 2005b, *Nature*, 438, 994
- Barthelmy S. D. et al., 1994, in *American Institute of Physics Conference Series*, Vol. 307, *Gamma-Ray Bursts*, Fishman G. J., ed., p. 643
- Baumgarte T. W., Shapiro S. L., Shibata M., 2000, *ApJL*, 528, L29

References

- Belczynski K., Perna R., Bulik T., Kalogera V., Ivanova N., Lamb D. Q., 2006, *ApJ*, 648, 1110
- Berger E., 2007, *ApJ*, 670, 1254
- Berger E., 2010, *ApJ*, 722, 1946
- Berger E., 2014, *ARA&A*, 52, 43
- Berger E., Boss A., 2005, *GRB Coordinates Network*, 3966, 1
- Berger E. et al., 2005, *Nature*, 438, 988
- Bernardini M. G. et al., 2013, *ApJ*, 775, 67
- Bernardini M. G., Margutti R., Zaninoni E., Chincarini G., 2012, *Memorie della Societa Astronomica Italiana Supplementi*, 21, 226
- Blandford R. D., McKee C. F., 1976, *Physics of Fluids*, 19, 1130
- Bloom J. S., Djorgovski S. G., Kulkarni S. R., Frail D. A., 1998, *ApJL*, 507, L25
- Bloom J. S., Frail D. A., Sari R., 2001, *AJ*, 121, 2879
- Bloom J. S., Kulkarni S. R., Djorgovski S. G., 2002, *AJ*, 123, 1111
- Bloom J. S. et al., 1999a, *Nature*, 401, 453
- Bloom J. S. et al., 2006, *ApJ*, 638, 354
- Bloom J. S., Sigurdsson S., Pols O. R., 1999b, *MNRAS*, 305, 763
- Bock D. C.-J., 2006, in *Astronomical Society of the Pacific Conference Series*, Vol. 356, *Revealing the Molecular Universe: One Antenna is Never Enough*, Backer D. C., Moran J. M., Turner J. L., eds., p. 17
- Boella G., Butler R. C., Perola G. C., Piro L., Scarsi L., Bleeker J. A. M., 1997, *A&AS*, 122, 299
- Bromberg O., Nakar E., Piran T., Sari R., 2013, *ApJ*, 764, 179
- Bucciantini N., Metzger B. D., Thompson T. A., Quataert E., 2012, *MNRAS*, 419, 1537
- Bucciantini N., Quataert E., Arons J., Metzger B. D., Thompson T. A., 2008, *MNRAS*, 383, L25
- Bucciantini N., Quataert E., Metzger B. D., Thompson T. A., Arons J., Del Zanna L., 2009, *MNRAS*, 396, 2038

References

- Bucciantini N., Thompson T. A., Arons J., Quataert E., Del Zanna L., 2006, *MNRAS*, 368, 1717
- Burrows D. N. et al., 2006, *ApJ*, 653, 468
- Burrows D. N. et al., 2005, *Science*, 309, 1833
- Cannizzo J. K., Troja E., Gehrels N., 2011, *ApJ*, 734, 35
- Cannizzo K. C. et al., 2006, *GRB Coordinates Network*, 5904, 1
- Cavallo G., Rees M. J., 1978, *MNRAS*, 183, 359
- Cenko S. B. et al., 2011, *ApJ*, 732, 29
- Cenko S. B., Kasliwal M., Cameron P. B., Kulkarni S. R., Fox D. B., 2006, *GRB Coordinates Network*, 5946, 1
- Chandra P., Frail D. A., 2006, *GRB Coordinates Network*, 5910, 1
- Chandra P., Frail D. A., 2007, *GRB Coordinates Network*, 6685, 1
- Chandra P., Frail D. A., 2012, *ApJ*, 746, 156
- Chandra P. et al., 2010, *ApJL*, 712, L31
- Chapman R., Levan A. J., Priddey R. S., Tanvir N. R., Wynn G. A., King A. R., Davies M. B., 2007, in *Astronomical Society of the Pacific Conference Series*, Vol. 372, 15th European Workshop on White Dwarfs, Napiwotzki R., Burleigh M. R., eds., p. 415
- Chincarini G. et al., 2010, *MNRAS*, 406, 2113
- Connaughton V., 2002, *ApJ*, 567, 1028
- Cook G. B., Shapiro S. L., Teukolsky S. A., 1992, *ApJ*, 398, 203
- Cook G. B., Shapiro S. L., Teukolsky S. A., 1994, *ApJ*, 422, 227
- Covino S. et al., 2005, *GRB Coordinates Network*, 3665, 1
- Covino S. et al., 2013, *MNRAS*, 432, 1231
- Cucchiara A. et al., 2011, *ApJ*, 736, 7
- Cummings J. R. et al., 2009, *GRB Coordinates Network*, 9461, 1

References

- Curran P. A., Starling R. L. C., O'Brien P. T., Godet O., van der Horst A. J., Wijers R. A. M. J., 2008, *A&A*, 487, 533
- Curran P. A., Starling R. L. C., van der Horst A. J., Wijers R. A. M. J., 2009, *MNRAS*, 395, 580
- Dall'Osso S., Stratta G., Guetta D., Covino S., De Cesare G., Stella L., 2011, *A&A*, 526, A121
- D'Avanzo P., Fiore F., Piranomonte S., Covino S., Tagliaferri G., Chincarini G., Stella L., 2007, *GRB Coordinates Network*, 7152, 1
- D'Avanzo P. et al., 2009, *A&A*, 498, 711
- de Pasquale M., Melandri A., 2013, *GRB Coordinates Network*, 14759, 1
- de Ugarte Postigo A. et al., 2014, *A&A*, 563, A62
- D'Elia V. et al., 2011, *GRB Coordinates Network*, 12578, 1
- Della Valle M. et al., 2006, *Nature*, 444, 1050
- Demorest P. B., Pennucci T., Ransom S. M., Roberts M. S. E., Hessels J. W. T., 2010, *Nature*, 467, 1081
- Dermer C. D., 2004, *ApJ*, 614, 284
- Dessart L., Burrows A., Livne E., Ott C. D., 2007, *ApJ*, 669, 585
- Dessart L., Burrows A., Livne E., Ott C. D., 2008, *ApJL*, 673, L43
- Dessart L., Ott C. D., Burrows A., Rosswog S., Livne E., 2009, *ApJ*, 690, 1681
- Djorgovski S. G., Kulkarni S. R., Bloom J. S., Goodrich R., Frail D. A., Piro L., Palazzi E., 1998, *ApJL*, 508, L17
- Drenkhahn G., Spruit H. C., 2002, *A&A*, 391, 1141
- Duffell P. C., MacFadyen A. I., 2014, *ArXiv e-prints*, 1407.8250
- Duncan R. C., Thompson C., 1992, *ApJL*, 392, L9
- Ellingson S. W. et al., 2013, *IEEE Transactions on Antennas and Propagation*, 61, 2540
- Esposito P. et al., 2010, *MNRAS*, 405, 1787
- Evans P. A. et al., 2009, *MNRAS*, 397, 1177

References

- Evans P. A. et al., 2007, *A&A*, 469, 379
- Falcone A. D. et al., 2006, *ApJ*, 641, 1010
- Fan Y.-Z., Xu D., 2006, *MNRAS*, 372, L19
- Fan Y.-Z., Yu Y.-W., Xu D., Jin Z.-P., Wu X.-F., Wei D.-M., Zhang B., 2013, *ApJL*, 779, L25
- Feng L., Vaulin R., Hewitt J. N., 2014, *ArXiv e-prints*, 1405.6219
- Fenimore E. E., Palmer D., Galassi M., Tavenner T., Barthelmy S., Gehrels N., Parsons A., Tueller J., 2003, in *American Institute of Physics Conference Series*, Vol. 662, *Gamma-Ray Burst and Afterglow Astronomy 2001: A Workshop Celebrating the First Year of the HETE Mission*, Ricker G. R., Vanderspek R. K., eds., pp. 491–493
- Fernández R., Metzger B. D., 2013, *MNRAS*, 435, 502
- Finn L. S., Chernoff D. F., 1993, *Phys. Rev. D*, 47, 2198
- Fishman G. J., Meegan C. A., Parnell T. A., Wilson R. B., Pacias W., Mateson J. L., Cline T. L., Teegarden B. J., 1985, *International Cosmic Ray Conference*, 3, 343
- Fong W. et al., 2014, *ApJ*, 780, 118
- Fong W.-f., 2014, PhD thesis, Harvard-Smithsonian Center for Astrophysics
- Fox D. B. et al., 2005, *Nature*, 437, 845
- Frail D. A., 2005a, *GRB Coordinates Network*, 4417, 1
- Frail D. A., 2005b, in *IAU Colloq. 192: Cosmic Explosions, On the 10th Anniversary of SN1993J*, Marcaide J.-M., Weiler K. W., eds., p. 451
- Frail D. A., Kulkarni S. R., Nicastro L., Feroci M., Taylor G. B., 1997, *Nature*, 389, 261
- Frail D. A. et al., 2001, *ApJL*, 562, L55
- Frank J., King A., Raine D. J., 2002, *Accretion Power in Astrophysics: Third Edition*
- Fruchter A. S. et al., 2006, *Nature*, 441, 463
- Fruchter A. S. et al., 1999, *ApJL*, 519, L13
- Fryer C. L., Woosley S. E., Herant M., Davies M. B., 1999, *ApJ*, 520, 650
- Fynbo J. P. U. et al., 2006, *Nature*, 444, 1047

References

- Gal-Yam A. et al., 2006, *Nature*, 444, 1053
- Galama T. J. et al., 2000, *ApJ*, 536, 185
- Galama T. J. et al., 1998, *Nature*, 395, 670
- Gao H., Ding X., Wu X.-F., Zhang B., Dai Z.-G., 2013a, *ApJ*, 771, 86
- Gao H., Lei W.-H., Zou Y.-C., Wu X.-F., Zhang B., 2013b, *NewA Rev.*, 57, 141
- Gehrels N. et al., 2004, *ApJ*, 611, 1005
- Gehrels N. et al., 2006, *Nature*, 444, 1044
- Gehrels N., Ramirez-Ruiz E., Fox D. B., 2009, *ARA&A*, 47, 567
- Gehrels N., Razzaque S., 2013, *Frontiers of Physics*, 8, 661
- Gehrels N. et al., 2005, *Nature*, 437, 851
- Ghirlanda G. et al., 2014, *PASA*, 31, 22
- Ghirlanda G., Ghisellini G., Celotti A., 2004, *A&A*, 422, L55
- Ghirlanda G., Nava L., Ghisellini G., Celotti A., Burlon D., Covino S., Melandri A., 2012, *MNRAS*, 420, 483
- Giacomazzo B., Perna R., 2013, *ApJL*, 771, L26
- Goad M. R. et al., 2007, *A&A*, 476, 1401
- Goldreich P., Reisenegger A., 1992, *ApJ*, 395, 250
- Gomboc A., 2012, *Contemporary Physics*, 53, 339
- Gompertz B. P., O'Brien P. T., Wynn G. A., 2014, *MNRAS*, 438, 240
- Gompertz B. P., O'Brien P. T., Wynn G. A., Rowlinson A., 2013, *MNRAS*, 431, 1745
- Gompertz B. P., van der Horst A. J., O'Brien P. T., Wynn G. A., Wiersema K., 2015, *MNRAS*, 448, 629
- Goodman J., 1986, *ApJL*, 308, L47
- Goodman J., 1997, *New Science*, 2, 449

References

- Graham J. F. et al., 2009, *ApJ*, 698, 1620
- Granot J., Panaitescu A., Kumar P., Woosley S. E., 2002, *ApJL*, 570, L61
- Greiner J. et al., 2011, *A&A*, 526, A30
- Grindlay J., Portegies Zwart S., McMillan S., 2006, *Nature Physics*, 2, 116
- Hancock P. J., Gaensler B. M., Murphy T., 2013, *ApJ*, 776, 106
- Harrison F. A. et al., 1999, *ApJL*, 523, L121
- Hjorth J. et al., 2003, *Nature*, 423, 847
- Hjorth J. et al., 2005, *Nature*, 437, 859
- Holcomb C., Ramirez-Ruiz E., De Colle F., Montes G., 2014, *ApJL*, 790, L3
- Hotokezaka K., Kiuchi K., Kyutoku K., Okawa H., Sekiguchi Y.-i., Shibata M., Taniguchi K., 2013, *Phys. Rev. D*, 87, 024001
- Hurley K. et al., 2005, *Nature*, 434, 1098
- Ivezic Z. et al., 2008, *ArXiv e-prints*, 0805.2366
- Kann D. A. et al., 2011, *ApJ*, 734, 96
- Kaplan S. A., Tsytovich V. N., 1973, *Plasma astrophysics*
- Katz J. I., 1997, *ApJ*, 490, 633
- King A. R., Ritter H., 1998, *MNRAS*, 293, L42
- Klebesadel R. W., Strong I. B., Olson R. A., 1973, *ApJL*, 182, L85
- Kouveliotou C. et al., 1998, *Nature*, 393, 235
- Kouveliotou C., Meegan C. A., Fishman G. J., Bhat N. P., Briggs M. S., Kosshut T. M., Paciasas W. S., Pendleton G. N., 1993, *ApJL*, 413, L101
- Kouveliotou C. et al., 1999, *ApJL*, 510, L115
- Kulkarni S. R. et al., 1999, *ApJL*, 522, L97
- Kumar P., 2000, *ApJL*, 538, L125

References

- Kumar P., Panaitescu A., 2000, *ApJL*, 541, L51
- Landsman W., Marshall F. E., Racusin J., 2007, *GRB Coordinates Network*, 6689, 1
- Lattimer J. M., 2011, *Ap&SS*, 336, 67
- Lattimer J. M., 2012, *Annual Review of Nuclear and Particle Science*, 62, 485
- Lattimer J. M., Prakash M., 2001, *ApJ*, 550, 426
- Lattimer J. M., Prakash M., 2004, *Science*, 304, 536
- Lazzati D., Ramirez-Ruiz E., Ghisellini G., 2001, *A&A*, 379, L39
- Lee W. H., Ramirez-Ruiz E., López-Cámara D., 2009, *ApJL*, 699, L93
- Lei W.-H., Zhang B., Liang E.-W., 2013, *ApJ*, 765, 125
- Levan A. J. et al., 2014, *ApJ*, 781, 13
- Levesque E. M., Kewley L. J., Graham J. F., Fruchter A. S., 2010a, *ApJL*, 712, L26
- Levesque E. M., Soderberg A. M., Kewley L. J., Berger E., 2010b, *ApJ*, 725, 1337
- Li L. et al., 2012, *ApJ*, 758, 27
- Li L.-X., Paczyński B., 1998, *ApJL*, 507, L59
- LIGO Scientific Collaboration et al., 2013, *ArXiv e-prints*, 1304.0670
- Lithwick Y., Sari R., 2001, *ApJ*, 555, 540
- LSST Science Collaboration et al., 2009, *ArXiv e-prints*, 0912.0201
- Lü H.-J., Zhang B., 2014, *ApJ*, 785, 74
- Lü H.-J., Zhang B., Liang E.-W., Zhang B.-B., Sakamoto T., 2014, *MNRAS*, 442, 1922
- Lü J., Zou Y.-C., Lei W.-H., Zhang B., Wu Q., Wang D.-X., Liang E.-W., Lü H.-J., 2012, *ApJ*, 751, 49
- Lyne A. G. et al., 2004, *Science*, 303, 1153
- Lyons N., O'Brien P. T., Zhang B., Willingale R., Troja E., Starling R. L. C., 2010, *MNRAS*, 402, 705

References

- MacFadyen A. I., Woosley S. E., 1999, *ApJ*, 524, 262
- Mangano V. et al., 2007, *A&A*, 470, 105
- Mao J. et al., 2008, *GRB Coordinates Network*, 7665, 1
- Margutti R. et al., 2011, *MNRAS*, 417, 2144
- Markwardt C. B., 2009, in *Astronomical Society of the Pacific Conference Series*, Vol. 411, *Astronomical Data Analysis Software and Systems XVIII*, Bohlender D. A., Durand D., Dowler P., eds., p. 251
- Mazets E. P., Golenetskii S. V., 1981, *Ap&SS*, 75, 47
- Mazets E. P., Golentskii S. V., Ilinskii V. N., Aptekar R. L., Guryan I. A., 1979, *Nature*, 282, 587
- McKinney J. C., 2006, *MNRAS*, 368, 1561
- Meegan C. et al., 2009, *ApJ*, 702, 791
- Meegan C. A., Fishman G. J., Wilson R. B., Horack J. M., Brock M. N., Paciesas W. S., Pendleton G. N., Kouveliotou C., 1992, *Nature*, 355, 143
- Melandri A. et al., 2008, *ApJ*, 686, 1209
- Mészáros P., 2002, *ARA&A*, 40, 137
- Mészáros P., 2006, *Reports on Progress in Physics*, 69, 2259
- Meszáros P., Rees M. J., 1993, *ApJL*, 418, L59
- Mészáros P., Rees M. J., 1997, *ApJ*, 476, 232
- Mészáros P., Rees M. J., 1999, *MNRAS*, 306, L39
- Meszáros P., Rees M. J., 2014, *ArXiv e-prints*, 1401.3012
- Metzger B. D., Arcones A., Quataert E., Martínez-Pinedo G., 2010, *MNRAS*, 402, 2771
- Metzger B. D., Bower G. C., 2014, *MNRAS*, 437, 1821
- Metzger B. D., Giannios D., Thompson T. A., Bucciantini N., Quataert E., 2011, *MNRAS*, 413, 2031
- Metzger B. D., Quataert E., Thompson T. A., 2008, *MNRAS*, 385, 1455

References

- Metzger M. R., Djorgovski S. G., Kulkarni S. R., Steidel C. C., Adelberger K. L., Frail D. A., Costa E., Frontera F., 1997, *Nature*, 387, 878
- Miller M. C., Miller J. M., 2015, *Phys. Rep.*, 548, 1
- Mirabal N., Halpern J. P., An D., Thorstensen J. R., Terndrup D. M., 2006, *ApJL*, 643, L99
- Mitsuda K. et al., 2007, *PASJ*, 59, 1
- Murguia-Berthier A., Montes G., Ramirez-Ruiz E., De Colle F., Lee W. H., 2014, *ApJL*, 788, L8
- Nakar E., Piran T., 2005, *ApJL*, 619, L147
- Nakar E., Piran T., 2011, *Nature*, 478, 82
- Narayan R., Paczynski B., Piran T., 1992, *ApJL*, 395, L83
- Narayan R., Piran T., Kumar P., 2001, *ApJ*, 557, 949
- Narayan R., Piran T., Shemi A., 1991, *ApJL*, 379, L17
- Norris J. P., Bonnell J. T., 2006, *ApJ*, 643, 266
- Norris J. P., Gehrels N., Scargle J. D., 2010, *ApJ*, 717, 411
- Norris J. P., Hertz P., Wood K. S., Kouveliotou C., 1991, *ApJ*, 366, 240
- Norris J. P., Nemiroff R. J., Bonnell J. T., Scargle J. D., Kouveliotou C., Paciasas W. S., Meegan C. A., Fishman G. J., 1996, *ApJ*, 459, 393
- Norris J. P., Share G. H., Messina D. C., Dennis B. R., Desai U. D., Cline T. L., Matz S. M., Chupp E. L., 1986, *ApJ*, 301, 213
- Nousek J. A. et al., 2006, *ApJ*, 642, 389
- Nysewander M., Fruchter A. S., Pe'er A., 2009, *ApJ*, 701, 824
- O'Brien P. T., Willingale R., Osborne J. P., Goad M. R., 2006, *New Journal of Physics*, 8, 121
- Ohno M. et al., 2012, in *American Institute of Physics Conference Series*, Vol. 1427, American Institute of Physics Conference Series, Petre R., Mitsuda K., Angelini L., eds., pp. 115–122
- Paczynski B., 1986, *ApJL*, 308, L43
- Paczynski B., 1990, *ApJ*, 363, 218

References

- Paczynski B., 1991, *Acta Astronomica*, 41, 257
- Page K., Chester M., Cummings J., Gehrels N., Kennea J., Markwardt C., Palmer D., Sakamoto T., 2005, *GRB Coordinates Network*, 3961, 1
- Palmer D. M. et al., 2005, *Nature*, 434, 1107
- Panaiteacu A., 2006, *MNRAS*, 367, L42
- Panaiteacu A., Kumar P., 2001, *ApJ*, 554, 667
- Panaiteacu A., Mészáros P., Gehrels N., Burrows D., Nousek J., 2006, *MNRAS*, 366, 1357
- Parsons A. M. et al., 2006, *GRB Coordinates Network*, 5252, 1
- Perley D. A., Bloom J. S., Thoene C., Butler N. R., 2007, *GRB Coordinates Network*, 6652, 1
- Perley D. A. et al., 2009, *ApJ*, 696, 1871
- Perley R. A., Chandler C. J., Butler B. J., Wrobel J. M., 2011, *ApJL*, 739, L1
- Phinney E. S., 1991, *ApJL*, 380, L17
- Piran T., 1999, *Phys. Rep.*, 314, 575
- Piran T., Nakar E., Rosswog S., 2013, *MNRAS*, 430, 2121
- Piro A. L., Ott C. D., 2011, *ApJ*, 736, 108
- Popham R., Woosley S. E., Fryer C., 1999, *ApJ*, 518, 356
- Poza H. B., 1979, *IEEE Transactions on Aerospace Electronic Systems*, 15, 414
- Price D. J., Rosswog S., 2006, *Science*, 312, 719
- Price P. A., Berger E., Fox D. B., 2006, *GRB Coordinates Network*, 5275, 1
- Prochaska J. X., Bloom J. S., Chen H.-W., Hansen B., Kalirai J., Rich M., Richer H., 2005, *GRB Coordinates Network*, 3700, 1
- Qin Y. et al., 2013, *ApJ*, 763, 15
- Racusin J. L., Barthelmy S. D., Burrows D. N., Chester M. M., Gehrels N., Krimm H. A., Palmer D. M., Sakamoto T., 2007, *GRB Coordinates Network*, 6620, 1
- Racusin J. L. et al., 2009a, *GRB Coordinates Network*, 9666, 1

References

- Racusin J. L. et al., 2009b, *ApJ*, 698, 43
- Ramirez-Ruiz E., Fenimore E. E., 2000, *ApJ*, 539, 712
- Rees M. J., Meszaros P., 1992, *MNRAS*, 258, 41P
- Rees M. J., Meszaros P., 1994, *ApJL*, 430, L93
- Rees M. J., Mészáros P., 1998, *ApJL*, 496, L1
- Ritz S. M., Gehrels N., McEnery J. E., Meegan C., Michelson P. F., Thompson D. J., Fermi Mission Team, 2009, in *Bulletin of the American Astronomical Society*, Vol. 41, American Astronomical Society Meeting Abstracts #213, p. #468.01
- Roming P. W. A. et al., 2005, *Space Science Rev.*, 120, 95
- Roming P. W. A. et al., 2009, *ApJ*, 690, 163
- Rosswog S., 2007, *MNRAS*, 376, L48
- Rosswog S., Ramirez-Ruiz E., Davies M. B., 2003, *MNRAS*, 345, 1077
- Rowlinson A., O'Brien P. T., Metzger B. D., Tanvir N. R., Levan A. J., 2013, *MNRAS*, 430, 1061
- Rowlinson A. et al., 2010a, *MNRAS*, 409, 531
- Rowlinson A. et al., 2010b, *MNRAS*, 408, 383
- Ruderman M., 1975, in *Annals of the New York Academy of Sciences*, Vol. 262, Seventh Texas Symposium on Relativistic Astrophysics, Bergman P. G., Fenyves E. J., Motz L., eds., pp. 164–180
- Ryan G., van Eerten H., MacFadyen A., Zhang B.-B., 2015, *ApJ*, 799, 3
- Rybicki G. B., Lightman A. P., 1986, *Radiative Processes in Astrophysics*
- Sakamoto T. et al., 2006, in *American Institute of Physics Conference Series*, Vol. 836, Gamma-Ray Bursts in the Swift Era, Holt S. S., Gehrels N., Nousek J. A., eds., pp. 43–47
- Sakamoto T. et al., 2007, *GRB Coordinates Network*, 7147, 1
- Santana R., Barniol Duran R., Kumar P., 2014, *ApJ*, 785, 29
- Sari R., Piran T., 1999, *ApJ*, 520, 641
- Sari R., Piran T., Halpern J. P., 1999, *ApJL*, 519, L17

References

- Sari R., Piran T., Narayan R., 1998, *ApJL*, 497, L17
- Schady P. et al., 2006, *GRB Coordinates Network*, 5699, 1
- Schlafly E. F., Finkbeiner D. P., 2011, *ApJ*, 737, 103
- Schlegel D. J., Finkbeiner D. P., Davis M., 1998, *ApJ*, 500, 525
- Schmidt W. K. H., 1978, *Nature*, 271, 525
- Shapiro I. I., 1964, *Physical Review Letters*, 13, 789
- Shapiro S. L., Teukolsky S. A., 1986, *Black Holes, White Dwarfs and Neutron Stars: The Physics of Compact Objects*
- Soderberg A. M. et al., 2006, *ApJ*, 650, 261
- Sonbas E., MacLachlan G. A., Shenoy A., Dhuga K. S., Parke W. C., 2013, *ApJL*, 767, L28
- Stanek K. Z. et al., 2003, *ApJL*, 591, L17
- Starling R. L. C., van der Horst A. J., Rol E., Wijers R. A. M. J., Kouveliotou C., Wiersema K., Curran P. A., Weltevrede P., 2008, *ApJ*, 672, 433
- Svensson K. M., Levan A. J., Tanvir N. R., Fruchter A. S., Strolger L.-G., 2010, *MNRAS*, 405, 57
- Swenson C. A., Roming P. W. A., 2014, *ApJ*, 788, 30
- Takahashi T. et al., 2007, *PASJ*, 59, 35
- Tanvir N. R. et al., 2009, *Nature*, 461, 1254
- Tanvir N. R., Levan A. J., Fruchter A. S., Hjorth J., Hounsell R. A., Wiersema K., Tunnicliffe R. L., 2013, *Nature*, 500, 547
- The LIGO Scientific Collaboration, The Virgo Collaboration, 2012, *ArXiv e-prints*, 1203.2674
- Thompson C., Duncan R. C., 1993, *ApJ*, 408, 194
- Thompson C., Duncan R. C., 1995, *MNRAS*, 275, 255
- Thompson T. A., 2007, in *Revista Mexicana de Astronomia y Astrofisica Conference Series*, Vol. 27, *Revista Mexicana de Astronomia y Astrofisica*, vol. 27, pp. 80–90
- Thompson T. A., Chang P., Quataert E., 2004, *ApJ*, 611, 380

References

- Thompson T. A., Quataert E., Burrows A., 2005, *ApJ*, 620, 861
- Thone C. C., de Ugarte Postigo A., Gorosabel J., Tanvir N., Fynbo J. P. U., 2013, *GRB Coordinates Network*, 14744, 1
- Tingay S. J. et al., 2013, *PASA*, 30, 7
- Tinney C. et al., 1998, *IAU Circ.*, 6896, 3
- Troja E. et al., 2009, *GRB Coordinates Network*, 9913, 1
- Troja E. et al., 2007, *ApJ*, 665, 599
- Tunnicliffe R. L. et al., 2014, *MNRAS*, 437, 1495
- Ukwatta T. N. et al., 2008, *GRB Coordinates Network*, 7203, 1
- Ukwatta T. N. et al., 2010, *ApJ*, 711, 1073
- Usov V. V., 1992, *Nature*, 357, 472
- Valentim R., Rangel E., Horvath J. E., 2011, *MNRAS*, 414, 1427
- van der Horst A. J., 2007, PhD thesis, University of Amsterdam
- van Eerten H., 2014, *MNRAS*, 442, 3495
- van Eerten H. J., MacFadyen A. I., 2012, *ApJ*, 751, 155
- van Haarlem M. P. et al., 2013, *A&A*, 556, A2
- van Paradijs J. et al., 1997, *Nature*, 386, 686
- Wainwright C., Berger E., Penprase B. E., 2007, *ApJ*, 657, 367
- Weaver C. et al., 2007, *GRB Coordinates Network*, 6657, 1
- Wijers R. A. M. J., Galama T. J., 1999, *ApJ*, 523, 177
- Willingale R., Genet F., Granot J., O'Brien P. T., 2010, *MNRAS*, 403, 1296
- Winkler C., Pace O., Volonté S., 1993, *ESA Journal*, 17, 207
- Woods P. M. et al., 1999, *ApJL*, 519, L139
- Woosley S. E., 1993, *ApJ*, 405, 273

References

Wright E. L., 2006, *PASP*, 118, 1711

Xu D. et al., 2009, *ApJ*, 696, 971

Yi T., Liang E., Qin Y., Lu R., 2006, *MNRAS*, 367, 1751

Zhang B., 2007, *Chinese J. Astron. Astrophys.*, 7, 1

Zhang B., Fan Y. Z., Dyks J., Kobayashi S., Mészáros P., Burrows D. N., Nousek J. A., Gehrels N., 2006, *ApJ*, 642, 354

Zhang B., Mészáros P., 2001, *ApJL*, 552, L35

Zhang B., Mészáros P., 2004, *International Journal of Modern Physics A*, 19, 2385

Zhang B., Yan H., 2011, *ApJ*, 726, 90

Zhang B., Zhang B.-B., Liang E.-W., Gehrels N., Burrows D. N., Mészáros P., 2007, *ApJL*, 655, L25

Zou Y.-C., Fan Y.-Z., Piran T., 2011, *ApJL*, 726, L2

Zou Y.-C., Piran T., 2010, *MNRAS*, 402, 1854

Zwart J. T. L. et al., 2008, *MNRAS*, 391, 1545